Univerità degli Studi di Trieste
Dipartimento di Ingegneria e Architettura

University of Sfax
National Engineering School of Sfax

XXXIII Doctoral Cycle

Insights into Methods for Electric Machine Winding Design

A thesis submitted for the dual degree of
Doctor of Philosophy
in
Electrical Engineering
and
Ingegneria Industriale e dell'Informazione

PhD Candidate	Nada Elloumi
PhD Program Coordinator	Fulvio Babich
Thesis Supervisor	Alberto Tessarolo
Thesis Co-supervisor	Ahmed Masmoudi

Academic year: 2019/2020

Acknowledgements

The research works presented in this thesis were developed during the PhD course conducted within the co-tutelle agreement between the *University of Sfax, the National Engineering School of Sfax (ENIS), Sfax, Tunisia,* and *the University of Trieste (UNITS), the Department of Engineering and Architecture, Trieste, Italy.* I am genuinely thankful to all the members from both the Italian and Tunisian sides that allowed this agreement to be successful.

I would like to express my deep gratitude to my academic supervisors from the Italian side Professor *Alberto Tessarolo* for giving me the opportunity to do research and providing invaluable guidance and suggestions beyond his intensive activities. It was a great privilege and honor to work and study under his guidance. I have learned from him the methodology to carry on research and the best way to present the research works as clearly as possible. A special thanks goes to my colleagues *Cesare Ciriani* and *Mario Mezzarobba* of the *Electrical Machine Analysis and Design Laboratory* for their invaluable support and availability whenever I needed help.
I also would like to thank my supervisor from the Tunisian side Professor *Ahmed Masmoudi* for his invaluable support from both academic and personal sides. Without his help and guidance, this study would not have been successful.

I am extremely grateful to my parents *Habib Elloumi* and *Salma Meslameni* for their love, prayers, care and sacrifices for educating me and preparing me for the future. They always have been my source of inspiration and my refuge from which I take strength and courage. I am very much thankful to my beloved sisters *Dorra, Rim, Maleke and Kaouthar* for their constant support and encouragements that helped me survive all the hurdles and not letting me give up.

Nada Elloumi

Preface

THE design of the stator winding has direct influence on the electric machine performance. As technology has advanced, researchers and motor manufacturers have worked on possible ways to improve the stator winding layout to achieve several targets depending on the application which namely consist of minimization of harmonic losses for improved efficiency, torque pulsation reduction, acoustic noise and vibration reduction,... For this purpose, an extensive range of literature have presented several design strategies for both synchronous and induction motors acting on winding connection types, configurations, conductors type and shape..., to achieve the required electrical performance. It has been shown that - depending on the application - some winding configurations can be more problematic than others as they produce additional undesirable parasitic effects. However, in some cases, the choice of the winding layout is limited by the required application which leads to look for solutions to cope with the winding configuration drawbacks.

The works presented in this thesis will deal with two different aspects of electrical machine windings that need to be further explored which consist of: fractional slot concentrated winding optimization in three-permanent magnet machines and study and improvement of the winding in terms of skin effect is large-medium voltage synchronous machines. Regarding the first topic, potentials and limits of the FSCW optimization through multi-layer arrangement will be presented to mitigate three problems: unbalanced magnetic pull (UMP), torque ripple and permanent-magnet eddy-current losses. As for the second topic, an extensive study of the eddy-currents losses in the stator equipped with form wound coils made of flat conductors embedded in open slots will be covered. Such study is important as it helps to identify the main causes of problems to avoid it through a suitable design.

Contents

List of Figures

List of Tables

Part 1

Design Optimization of Multilayer Fractional-Slot Concentrated Winding for Surface Permanent Magnet Machines

1.1 Introduction to the fractional slot concentrated winding surface permanent magnet machines optimization

PERMANENT magnet synchronous machines (PMSM) are widely found in numerous applications from automotive to aerospace since they offer several key features such as high power density, high efficiency and good dynamic performance. Among PM machines, surface-mounted permanent-magnet (SPM) motors combined with fractional slot concentrated non-overlapping winding (FSCW) can be profitably chosen for several advantages they offer. Indeed, the use of FSCW in the design of PMSMs is revealed to be extremely beneficial [1] thanks to various advantages such as good faults tolerance capability [2], improved manufacturability and modularity [3], reduced end-coils and overall axial length [4] and increased flux weakening performance [5].

However, a well-known drawback of FSCWs is the presence of a large magneto-motive force (MMF) space harmonic content causing additional parasite effect. Among the several issues generated by the presence of the rich harmonic content, the most harmful effects consists of:

- eddy current losses creation in the rotor magnets causing possible consequent overheating and demagnetization issues [6, 7],
- unbalanced Magnetic Pull (UMP) due to the interaction of the induced space harmonics for some particular slot pole combinations causing mechanical noise and vibration [8, 9],
- an excessive torque ripple which occurs as a result of the interaction between the rotor field distribution and the armature MMF distribution [10].

To address the issue, the literature presents several works about FSCW MMF harmonics reduction from the design point of view dealing with stator winding type of connection and layout. For example, a space shifted star-delta winding is proposed to minimize the interactive space harmonics [10]. The use of multiphase configuration was proven to be useful for the reduction of induced eddy losses [11]. However, The most common and promising technique for MMF space harmonic reduction is the adoption of multilayer arrangement in which more then two coils belonging to different phases are wound around the same tooth [12, 13]. It has been shown that with increasing the winding layer number, some of the space harmonics in the MMF could be significantly reduced or even cancelled which has an important impact on the performance and the characteristics of the machine.

However, it has been observed that in multi-layer FSCW even better results can be achieved if unequal coils having different number of turns are employed [14–16]. As a study case and for the sake of torque ripple minimization, a four layer FSCW with unequal coils has been proposed in [16] for a 12-slot/10-pole IPM machine to reduce armature reaction induce space harmonics. Whereas the aforementioned method adopted multi-layer technique from the stator side, the optimization focused on IPM machines topology which has different behaviour compared to SPM machines. The major part of the literature dealing with multi-layer winding technique is based on a case-by-case reasoning using the star of slot method [17] to elaborate winding layouts leading to the cancellation of given MMF harmonics or subharmonics. However, the question is left unanswered whether the proposed multilayer winding solution can be considered as "optimal" and if can be actually further improved through some different arrangement of tooth coil and different selection of their number of turns. For this purpose, a more general method for different slot-pole combinations FSCW SPM machines directly targeting the most problematic configuration for which an optimal solution could be generated has to be proposed.

Recently, some attempts to built a more generalized multilayer stator winding optimization methods aiming at introducing automated procedures for obtaining winding layout solutions have been performed. In [18], a multi-objective differential evolution optimization algorithm is proposed aiming to reduce the air-gap MMF total harmonic distortion (THD) and winding resistance to get a general solution of multilayer configuration suitable for any kind of winding whether it is integer or fractional slots. Another work proposed in [19] which similarly acts on the MMF THD to reduce the MMF harmonic content uses linear algebraic technique to define multilayer winding layouts applied on FSCW. However, while the aforementioned works features automated methods of optimization, they seem to be very general in terms of MMF space harmonic reduction regardless of the application and may lead to a further complication of the winding layout, i.e. by unnecessarily increasing the number of layers per slot. In fact, even if the high harmonic content of the FSCW MMF spectrum lies under the generation of the majority of parasitic effects in the machine, not all harmonics act the same toward giving rise to unwanted phenomena. For this reason comes the need for considering the harmonic spectrum analysis as a base from which the objective of the optimization is determined depending on the application.

This Part suggests a new general, systematic and automated method aimed at the optimization of three phase multilayer FSCW SPM machines based on [20]. This method basically focuses on the study of the harmonic spectrum of the different FSCW topologies to determine the most harmful harmonic orders leading to the generation of parasitic aspects. The winding optimization is then applied by means of a single objective quadratic programming which can be solved using existing computationally efficient algorithms [21] in terms of minimizing the undesirable parasitic aspect. Indeed, constraints are imposed to guarantee that the winding is feasible using non-overlapping tooth coils [2] and is electrically symmetric. The developed optimization method will be applied to different study cases by adapting the objective function to the desired optimizing feature in terms of UMP, rotor eddy current losses and torque pulsation minimization. The proposed optimization outputs the best design automatically identifying the optimal number of layers, the optimal number of turns for each coil and the optimal assignment of the coils to the phases, without requiring any reasoning or intervention by the designer and guaranteeing winding symmetry and feasibility.

This Part is organized as follows. Section 1.2 gives a brief presentation of classical use of the star of slots method in conventional double layer FSCW. In Section 1.3 the multilayer FSCW concept is introduced and the analytical model of the air-gap MMF harmonic computation is described. The formulation of the quadratic programming problem is presented in Section 1.4. Section 1.5 presents different applications of the quadratic programming algorithm aiming at minimizing the UMP, the torque ripple and eddy-current magnet losses respectively. Potentials of employing FSCW configuration in squirrel-cage induction machines will be covered as well in order to investigate on the possibility of optimizing the winding layout to enhance the machine performance.

1.2 Use of Star of Slots in the Design of Conventional Double Layer FSCW

The star of slots method was initially proposed for designing large synchronous generators fractional slot windings with a high number of poles to maximise the main harmonics of the electromotive force (EMF) induced in the windings. Lately, the star of slot technique has been considered for the arrangement of FSCW equipping PM synchronous machines[17, 22]. It is designed to build a balanced symmetrical m-phase winding which contains the information of the winding distribution. Thus it can be adopted for the analysis of the harmonic content of the airgap MMF distribution. In the following, a three-phase double layer winding motor is considered. The considerations that are presented are valid for any odd number of phases m.

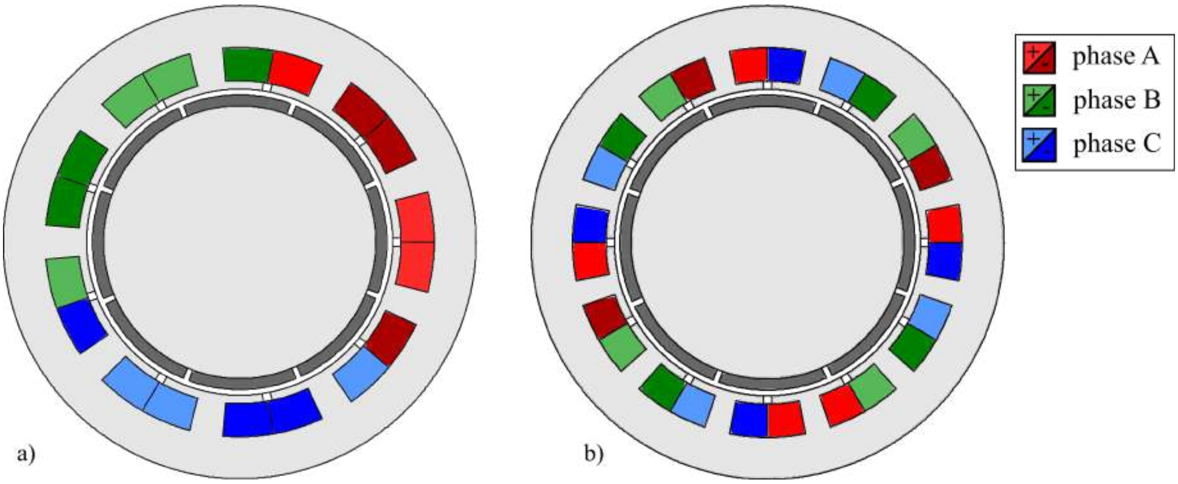

Figure 1.1: Examples of fractional-slot double-layer motors with non-overlapped coils **a)** 9 slots/8 poles configuration, **b)** 12 slots/8 poles configuration.

1.2.1 Classical drawing of star of slots

The star of slots is the phasor representation of the main EMF harmonic induced in the coil side of each slot. The machine periodicity is given by the greatest common divisor of the number of slots Z and the number of pole pairs p which corresponds to the number of identical parts the machine could be split in.

$$t = \gcd(Z, p) \tag{1.1}$$

The star of slots phasor diagram is characterized by Z/t spokes where each spoke is containing t phasors. Giving the fact that the Z slots are equidistant, the electric angular displacement between two phasors induced in the coils of two adjacent slots is equal to the electrical angle α_s expressed as follows:

$$\alpha_s = p\frac{2\pi}{Z} \tag{1.2}$$

The angle between two adjacent spokes results in

$$\alpha_{ph} = \alpha_s t \tag{1.3}$$

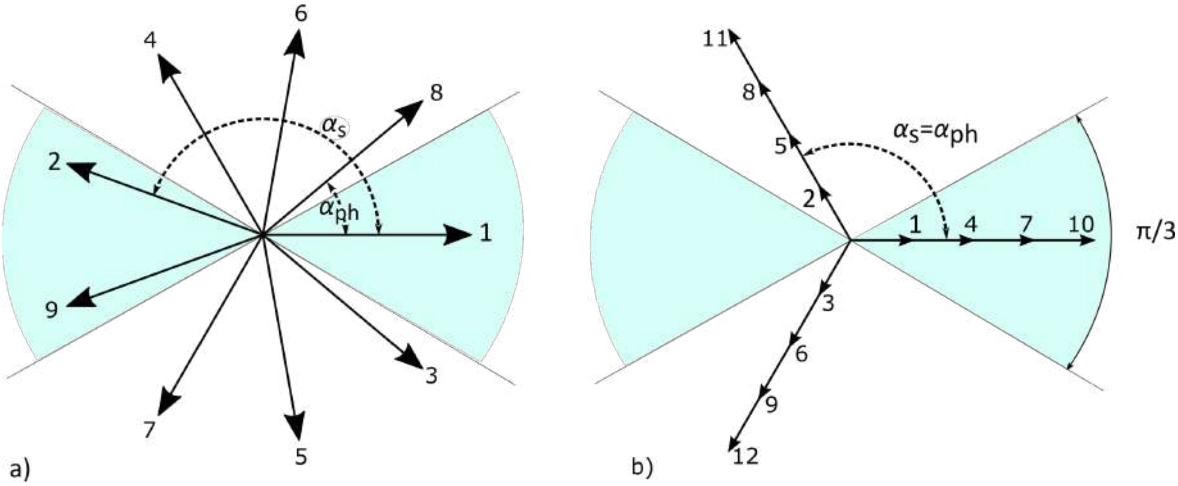

Figure 1.2: Star of slots of double layer FSCW SPM machines presented in Fig. 1.1 **a)** 9 slots/8 poles configuration with t=1, number of spokes equal to 9 with one phasor each, **b)** 12 slots/8 poles configuration with t=4, number of spokes equal to 3 with four phasors each.

As shown in Figure 1.2, the number given to each phasor corresponds to the number given consecutively to each stator slot. The phasors belonging to the same phase are located inside two opposite sectors which has an angular opening equal to $\frac{\pi}{m}$. The coils located within a sector are fed with a positive polarity, while those of the opposite sector are fed with a negative polarity.
For the sake of more compactness, the star of slots graphical method can be translated into a matricial form to facilitate its implementation into the optimization algorithm. For that, the winding topology for a conventional double layer FSCW can represented by a $Z \times 3$-sized "winding matrix" $\mathbf{W}$ characterized by $k = 0..Z-1$ rows representing the stator slots index and $l = "a", "b" and "c"$ referring to the stator phases:

$$[\mathbf{W}]_{k,l} = W_{k,l} \tag{1.4}$$

Each element $W_{k,l}$ of the winding matrix $\mathbf{W}$ represents the number of turns wound around the k^{th} tooth belonging to the phase $"l"$ where $W_{k,l}$ takes the sign of the polarity of the phase as shown in Table 1.1 (a). To avoid the use of negative winding matrix elements $W_{k,l}$, the number of columns can be extended to $2m = 6$ so that each column refers to one polarity of phase and all number of turns $W_{k,l}$ wound around each tooth belonging to that phase are positive values (Table 1.1 (b)).

1.2.2 Winding Feasibility Condition

It is commonly assumed in the literature that, for a three-phase dual layer FSCW with Z slots and p pole pairs to be symmetrical, the number of slots Z must be an integer multiple of $(3\,gcd(Z,p))$=

Table 1.1: Example of a winding matrix for the 9 slots/8 poles configuration were the number of turns per tooth is set to 100, **a)** using the physical phases a, b and c; **b)** using equivalent sub-phases.

(a)

l k	a	b	c
0	100	0	0
1	−100	0	0
2	0	0	−100
3	0	0	100
4	0	0	−100
5	0	−100	0
6	0	100	0
7	0	−100	0
8	−100	0	0

(b)

l	0	1	2	3	4	5
k	$+a$	$-c$	$+b$	$-a$	$+c$	$-b$
0	100	0	0	0	0	0
1	0	0	0	100	0	0
2	0	100	0	0	0	0
3	0	0	0	0	100	0
4	0	100	0	0	0	0
5	0	0	0	0	0	100
6	0	0	100	0	0	0
7	0	0	0	0	0	100
8	0	0	0	100	0	0

$3t$. In other words, the feasibility constraint consists of having an equal number of spokes per phase according to Z and p. Than the following relation has to be met:

$$\frac{Z}{mt} \in \mathbb{N} \tag{1.5}$$

The machines slots/poles combinations meeting the aforementioned constraint are referred to as conventional.

Besides the usefulness of the star of slots method in the design of double and single layer winding, multilayer winding are also feasible but mostly based on case by case reasoning. To make the procedure more automatic, a suitable mathematical tool can be developed to generate solutions for multilayer winding design which requires a more compact mathematical expressions that facilitate the implementation into optimization algorithms. In what follows, a matricial notation of the winding distribution in the stator slots will be considered which will be implemented in the developed analytical approach.

1.3 Multilayer FSCW Model and MMF Analysis

1.3.1 Multilayer FSCW modeling

In what follows, a modeling of multilayer winding in order to fit the quadratic programming requirements is proposed. In general, for a multilayer FSCW machine each of the Z stator teeth is assumed to have three coils wound around it, one coil for each of the three phases a, b and c.The polarity sign of the number of turns $N_{k,a}$, $N_{k,b}$ and $N_{k,c}$ of the three coils of each slot must be taken positive or negative depending on the direction of the relevant current i_a, i_b and i_c (according to the conventional positive direction chosen for the current e.g., positive if entering the page, negative otherwise). The sum of the number of turns of each phase wound around one tooth do not have to exceed the total number of turns N_0 which can be round around a tooth. From that the following constraint must hold:

$$|N_{k,a}| + |N_{k,b}| + |N_{k,b}| \leq N_0 \tag{1.6}$$

The total amperturns flowing around the k^{th} tooth are equal to

$$N_{k,a}i_a + N_{k,b}i_b + N_{k,b}i_c \tag{1.7}$$

The developed optimization approach based on quadratic programming aims at finding the FSCW optimal design under suitable constraints. It can be applied if the objective function is linear or quadratic function of the design variables. The constraints have to be formulated in a linear equalities or inequalities.

Regardless of the objective function, the FSCW optimal design implies determining the number of turns $N_{k,a}$, $N_{k,b}$ and $N_{k,c}$ for any $k = 0, 1, ..., Z - 1$ considered as design variables under

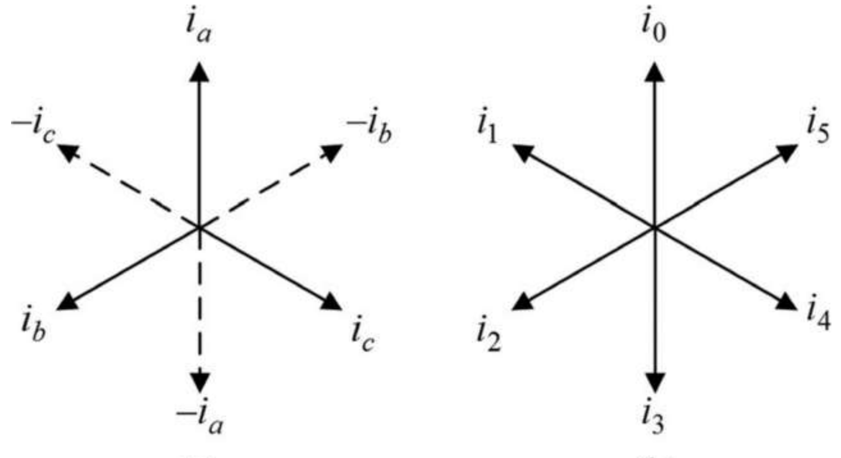

Figure 1.3: **(a)** Phase current phasors, **(b)** equivalent sub-phase phasors.

suitable constraints (including (1.7)). However, the non-linearity of (1.7) with respect to the design variables $N_{k,a}$, $N_{k,b}$ and $N_{k,c}$ makes it unsuitable as a constraint to be considered in the optimization algorithm. To linearize the problem, it is convenient to introduce a system of fictitious "sub-current" i_0, i_1, i_2, i_3, i_4 and i_5 which phasors are illustrated in Figure 1.3 together with the phasors of the physical currents i_a, i_b and i_c. From that, it can be easily seen that the proposed "sub-currents" are related to the standard physical currents such as

$$i_a = i_0 = -i_3, \;\; i_b = i_2 = -i_5, \;\; i_c = i_4 = -i_1 \tag{1.8}$$

This implies that each phase coil wound around the k^{th} tooth can be split into a couple of "sub-coils", one with positive polarity and the other with negative polarity, having the same overall number of turns. As shown in Figure 1.4, six sub-coils are wound around the tooth, composed of $N_{k,j} \geq 0$ turns each where $j = 0, 1, .., 5$ such that

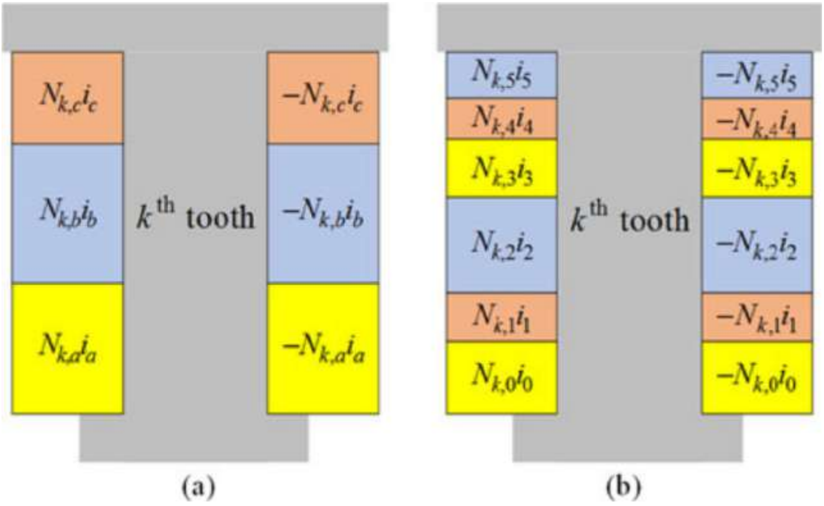

Figure 1.4: Illustrative multilayer structure: phase sub-coils wound around the k^{th} tooth with corresponding amperturns. **(a)** three phase sub-coils; **(b)** equivalent configuration with six sub-coils.

$$N_{k,0} + N_{k,1} + N_{k,2} + N_{k,3} + N_{k,4} + N_{k,5} \leq N_0 \tag{1.9}$$

Then the total amperturns around the k^{th} tooth are now equal to

$$N_{k,0}i_0 + N_{k,1}i_1 + N_{k,2}i_2 + N_{k,3}i_3 + N_{k,4}i_4 + N_{k,5}i_5 \tag{1.10}$$

In order that the proposed multilayer model (Figure 1.4 (b)) will be equivalent to the standard configuration (Figure 1.4 (a)) in terms of air-gap MMF, the equality between (1.7) and (1.9) has to be imposed. Based on (1.8) this happen if

$$N_{k,a} = N_{k,0} - N_{k,3}, \;\; N_{k,b} = N_{k,2} - N_{k,5}, \;\; N_{k,c} = N_{k,4} - N_{k,1} \tag{1.11}$$

The linear aspect of the obtained constraint (1.9) allows its implementation in the optimization algorithm.Therefore, the model assumed in the rest of the section is that shown in Figure 1.4 (b) under the assumption (1.11). Accordingly, the design variables will be $N_{k,j}$ which are positive or null quantities subject to the linear constraint (1.9). The current flowing in the six sub-coils of each tooth is expressed as:

$$i_j(t) = I_0 \cos\left(\omega t - \frac{\pi}{3} j\right) \tag{1.12}$$

where I_0 and f are the phase current amplitude and frequency, $\omega = 2\pi f$ and $j = 0, 1, .., 5$.

1.3.2 Air-gap MMF Harmonic Computation

An explicit expression for the air-gap MMF as function of the design variables, i.e., the number of turns $N_{k,j}$ is necessary in order to be implemented in the FSCW design optimization algorithm.

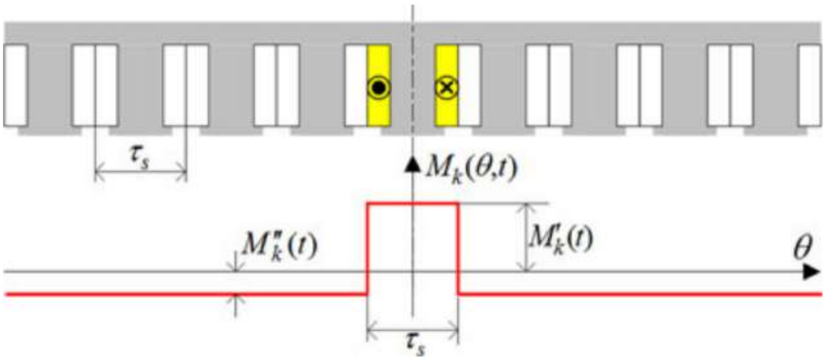

Figure 1.5: Air-gap MMF produced by the k^{th} wound tooth energized with a total current $i_k(t)$.

For the sake of simplification, the stator and rotor cores are considered as linear. Thus, the superposition principle can be applied so that the air-gap MMF due to the entire winding can be computed by summing the contribution of each tooth. The waveform of the air-gap MMF generated by the amperturns(1.10) of the k^{th} tooth is presented in Figure 1.5 where

$$M_k(\theta, t) = \begin{cases} M'_k(t) = \dfrac{Z-1}{Z} \sum\limits_{j=0..5} N_{k,j} i_j(t), & \text{if } |\theta| \leq \tau_s \\ M''_k(t) = \dfrac{-1}{Z} \sum\limits_{j=0..5} N_{k,j} i_j(t), & \text{if } \dfrac{\tau_s}{2} \leq |\theta| \leq \pi \end{cases} \tag{1.13}$$

and $\tau_s = 2\pi/Z$.

In order to consider all the harmonic orders, the expression for $M_k(\theta, t)$ can be written using Fourier series as [23]:

$$M_k(\theta, t) = \left(\sum_{j=0..5} N_{k,j} i_j(t)\right) \left(\sum_{n=1..\infty} a_n cos(n\theta)\right) \tag{1.14}$$

where the Fourier coefficient a_n is given by

$$a_n = \frac{2}{\pi}\frac{1}{n}(-1)^n \sin\left(\frac{\pi n(Z-1)}{Z}\right) \tag{1.15}$$

Then, the total airgap MMF can be easily computed by summing the contribution of the coils of all the stator teeth displaced by $2\pi/Z$ apart leading to the overall MMF following expression

$$\begin{aligned} M_s(\theta,t) &= \sum_{k=0..Z-1} M_k\left(\theta - k\frac{2\pi}{Z}, t\right) \\ &= \sum_{k=0..Z-1}\sum_{j=0..5}\sum_{n=1..\infty} a_n N_{k,j} I_0 \cos\left(\omega t - j\frac{\pi}{3}\right)\cos\left(n\theta - nk\frac{2\pi}{Z}\right) \end{aligned} \tag{1.16}$$

To obtain more compact expression of the total air-gap MMF, it is possible to manipulate (1.16) using the complex trigonometric functions such as

$$\cos\left(\omega t - j\frac{\pi}{3}\right)\cos\left(n\theta - nk\frac{2\pi}{Z}\right) = Re\left\{e^{i(\omega t - j\frac{\pi}{3})}\frac{1}{2}\left[e^{i(n\theta - nk\frac{2\pi}{Z})} + e^{-i(n\theta - nk\frac{2\pi}{Z})}\right]\right\} \tag{1.17}$$

After few mathematical simplifications and passages, equation (1.16) can be put in the following form:

$$\begin{aligned} M_s(\theta,t) &= Re\left\{\sum_{n=1..\infty}\left[m_n^- e^{i(\omega t - n\theta)} + m_n^+ e^{i(\omega t + n\theta)}\right]\right\} \\ &= Re\left\{\sum_{n=1..\infty}\left[|m_n^-| e^{i(\omega t - n\theta + arg(m_n^-))} + |m_n^+| e^{i(\omega t + n\theta + arg(m_n^+))}\right]\right\} \\ &= \sum_{n=1..\infty}\left[|m_n^-|\cos\left(\omega t - n\theta + arg(m_n^-)\right) + |m_n^+|\cos\left(\omega t + n\theta + arg(m_n^+)\right)\right] \end{aligned} \tag{1.18}$$

where

$$m_n^- = \frac{a_n I_0}{2}\sum_{k=1..Z-1}\sum_{j=0..5} N_{j,k} e^{i(-\frac{\pi}{3}j + kn\frac{2\pi}{Z})} \tag{1.19}$$

$$m_n^+ = \frac{a_n I_0}{2}\sum_{k=1..Z-1}\sum_{j=0..5} N_{j,k} e^{i(-\frac{\pi}{3}j - kn\frac{2\pi}{Z})} \tag{1.20}$$

are the complex coefficients for the n^{th} order space harmonics. The sign "-" refers to the harmonics revolving in the same direction with respect to the rotor (co-rotating) while the sign "+" refers to the ones rotating in the opposite direction (counter-rotating). Thanks to the developed expression

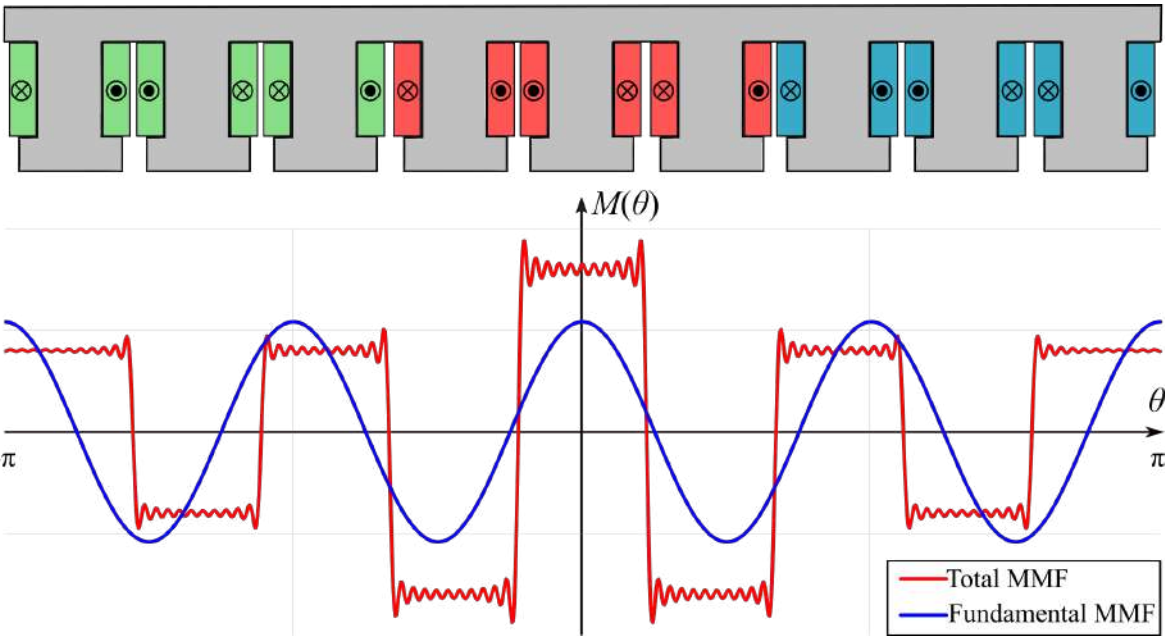

Figure 1.6: Air-gap MMF distribution for conventional 9 slots/8 poles FSCW machine configuration along the angular coordinate θ for an instant $t = 0$s.

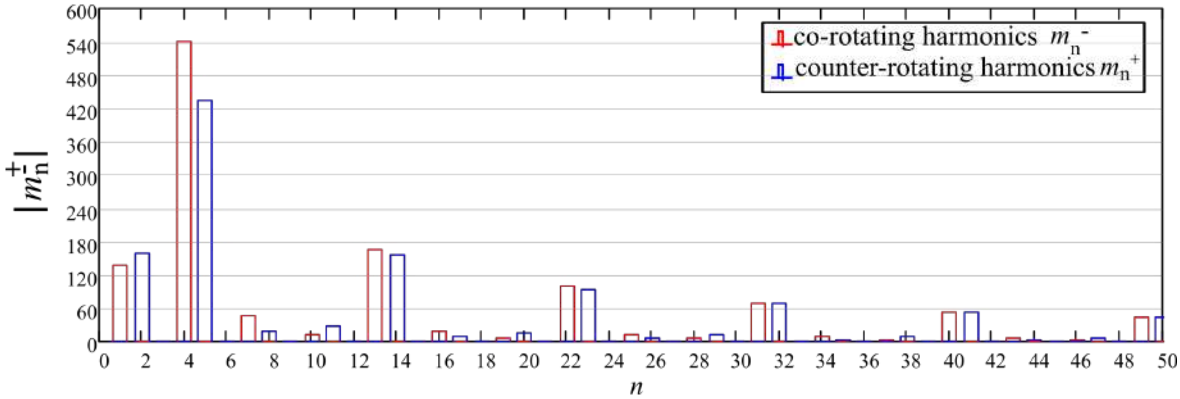

Figure 1.7: Air-gap MMF harmonic amplitudes for conventional 9 slots/8 poles FSCW machine configuration with taking $I_0 = 8$ A and $f = 50$ Hz.

(1.18) of the total air-gap MMF, the amplitude of each MMF harmonic order can be easily determined by means of m_n^- and m_n^+ (Figures 1.6 and 1.7) which is very useful for the MMF harmonic spectral analysis and enables the manipulation of each harmonic independently.

1.3.3 Stator MMF formulation for quadratic programming

A more compact expression for (1.19) and (1.20) function of the design variables is needed to facilitate their implementation in the quadratic optimization algorithm. For that, all the variables $N_{k,j}$ are grouped into a single $6Z$-sized vector $\mathbf{x}$ defined as follows:

$$\mathbf{x} = (N_{0,0}...N_{0,5}, N_{1,0}...N_{1,5}, ...N_{Z-1,0}...N_{Z-1,5})^T \tag{1.21}$$

such that

$$[\mathbf{x}]_{6k+j} = N_{k,j} \quad \forall \ j = 0..5 \ \ and \ \ k = 0..Z-1 \tag{1.22}$$

This allows for (1.19) and (1.20) to be written in a compact form as:

$$\begin{aligned} m_n^{\pm} &= \frac{a_n I_0}{2} \sum_{h=1..6Z-1} [\mathbf{x}]_h \, e^{i\left(-\frac{\pi}{3} mod(h,6) \mp n \frac{2\pi}{Z} floor(\frac{h}{6})\right)} \\ &= v_n^{\pm T} \mathbf{x} \end{aligned} \tag{1.23}$$

where $mod(x, y)$ and $floor(x, y)$ are functions returning the remainder and the integer part of the division of $\mathbf{x}$ by y. The complex vectors v_n^+ and v_n^- are defined as follows:

$$[v_n^{\pm}]_h = \frac{a_n I_0}{2} \, e^{i\left(-\frac{\pi}{3} mod(h,6) \mp n \frac{2\pi}{Z} floor(\frac{h}{6})\right))} \ \forall \ h = 0..6Z-1 \tag{1.24}$$

Thanks to the complex nature of equation (1.23), it is possible to express the air-gap space harmonic amplitudes m_n^- and m_n^+ as follows:

$$\begin{aligned} |m_n^{\pm}| = \sqrt{\overline{m}_n^{\pm} m_n^{\pm}} &= \sqrt{(\overline{v_n^{\pm T} \mathbf{x}})(v_n^{\pm T} \mathbf{x})} \\ &= \sqrt{\overline{(v_n^{\pm T} \mathbf{x})}^T (v_n^{\pm T} \mathbf{x})} \\ &= \sqrt{\mathbf{x}^T \overline{v}_n^{\pm} v_n^{\pm T} \mathbf{x}} \\ &= \sqrt{\mathbf{x}^T \mathbf{H}_n^{\pm} \mathbf{x}} \end{aligned} \tag{1.25}$$

Where $\mathbf{H}_n^{\pm}$ indicates the symmetric $6Z \times 6Z$ matrices defined as follows:

$$\mathbf{H}_n^{\pm} = \overline{v}_n^{\pm} v_n^{\pm T} \tag{1.26}$$

Since the obtained $\mathbf{H}_n^{\pm}$ is a complex matrix and the $\boldsymbol{x}$ vector (1.21) being real, equation (1.25) can be rewritten as:

$$|m_n^{\pm}|^2 = Re\{|m_n^{\pm}|^2\} = \mathbf{x}^T Re\{\mathbf{H}_n^{\pm}\}\mathbf{x} = \mathbf{x}^T \mathbf{Q}_n^{\pm}\mathbf{x} \tag{1.27}$$

where $\mathbf{Q}_n^{\pm} = \Re\{\mathbf{H}_n^{\pm}\}$ are real-valued matrices which will be employed in the optimization algorithm and can be computed based on (1.26) as:

$$\mathbf{Q}_n^{\pm} = Re\{\overline{v}_n^{\pm} v_n^{\pm T}\} = Re\{v_n^{\pm}\}Re\{v_n^{\pm T}\} + Im\{v_n^{\pm}\}Im\{v_n^{\pm T}\} \tag{1.28}$$

1.3.4 Symmetry constraint of the three phase system

One important constraint to be imposed to guarantee the feasibility of the FSCW resultant from the optimization algorithm is the symmetry of the three phase system. To fulfill this constraint, the three phase sinusoidal waves must be equal in magnitude and phase. For that it is needed to determine the contribution of the three phases to the MMF fundamental which is possible through using equation (1.18). Actually, it is sufficient to substitute the harmonic order n by the number of pole pairs p considering only the "co-rotating" revolving with the same direction as the rotor such that:

$$M_{s,fund}(\theta, t) = Re\{m_p^{-} e^{i(\omega t - p\theta)}\} \tag{1.29}$$

By substituting (1.23) into (1.29), it is possible to express the fundamental MMF expression using the "turn vector" $\mathbf{x}$ as:

$$M_{s,fund}(\theta, t) = Re\{v_p^{-T}\mathbf{x}e^{i(\omega t - p\theta)}\} \tag{1.30}$$

In order to determine the MMF fundamentals due to each phase individually, the following 6×6 matrices are introduced:

$$\begin{gathered}
\mathbf{K}_{6a} = \begin{pmatrix} 1 & 0 & 0 & 0 & 0 & 0 \\ 0 & 0 & 0 & 0 & 0 & 0 \\ 0 & 0 & 0 & 0 & 0 & 0 \\ 0 & 0 & 0 & 1 & 0 & 0 \\ 0 & 0 & 0 & 0 & 0 & 0 \\ 0 & 0 & 0 & 0 & 0 & 0 \end{pmatrix}
\mathbf{K}_{6b} = \begin{pmatrix} 0 & 0 & 0 & 0 & 0 & 0 \\ 0 & 1 & 0 & 0 & 0 & 0 \\ 0 & 0 & 0 & 0 & 0 & 0 \\ 0 & 0 & 0 & 0 & 0 & 0 \\ 0 & 0 & 0 & 0 & 1 & 0 \\ 0 & 0 & 0 & 0 & 0 & 0 \end{pmatrix} \\
\mathbf{K}_{6c} = \begin{pmatrix} 0 & 0 & 0 & 0 & 0 & 0 \\ 0 & 0 & 0 & 0 & 0 & 0 \\ 0 & 0 & 1 & 0 & 0 & 0 \\ 0 & 0 & 0 & 0 & 0 & 0 \\ 0 & 0 & 0 & 0 & 0 & 0 \\ 0 & 0 & 0 & 0 & 0 & 1 \end{pmatrix}
\mathbf{0}_6 = \begin{pmatrix} 0 & 0 & 0 & 0 & 0 & 0 \\ 0 & 0 & 0 & 0 & 0 & 0 \\ 0 & 0 & 0 & 0 & 0 & 0 \\ 0 & 0 & 0 & 0 & 0 & 0 \\ 0 & 0 & 0 & 0 & 0 & 0 \\ 0 & 0 & 0 & 0 & 0 & 0 \end{pmatrix}
\end{gathered} \tag{1.31}$$

and used to build the following $6Z \times 6Z$ matrices:

$$\mathbf{K}_a = \begin{pmatrix} \mathbf{K}_{6a} & \mathbf{0}_6 & \dots & \mathbf{0}_6 \\ \mathbf{0}_6 & \mathbf{K}_{6a} & \dots & \mathbf{0}_6 \\ \vdots & \vdots & \ddots & \vdots \\ \mathbf{0}_6 & \mathbf{0}_6 & \dots & \mathbf{K}_{6a} \end{pmatrix} \mathbf{K}_b = \begin{pmatrix} \mathbf{K}_{6b} & \mathbf{0}_6 & \dots & \mathbf{0}_6 \\ \mathbf{0}_6 & \mathbf{K}_{6b} & \dots & \mathbf{0}_6 \\ \vdots & \vdots & \ddots & \vdots \\ \mathbf{0}_6 & \mathbf{0}_6 & \dots & \mathbf{K}_{6b} \end{pmatrix}$$
$$\mathbf{K}_c = \begin{pmatrix} \mathbf{K}_{6c} & \mathbf{0}_6 & \dots & \mathbf{0}_6 \\ \mathbf{0}_6 & \mathbf{K}_{6c} & \dots & \mathbf{0}_6 \\ \vdots & \vdots & \ddots & \vdots \\ \mathbf{0}_6 & \mathbf{0}_6 & \dots & \mathbf{K}_{6c} \end{pmatrix} \tag{1.32}$$

It can be easily seen that

$$\mathbf{K}_a + \mathbf{K}_b + \mathbf{K}_c = \mathbf{I}_{6Z} \tag{1.33}$$

where $\mathbf{I}_{6Z}$ is a $6Z \times 6Z$ identity matrix.
Thus, the "turn vector" $\mathbf{x}$ can be also written as follows:

$$\mathbf{x} = \mathbf{I}_{6Z}\mathbf{x} = (\mathbf{K}_a + \mathbf{K}_b + \mathbf{K}_c)\mathbf{x} = \mathbf{x}_a + \mathbf{x}_b + \mathbf{x}_c \tag{1.34}$$

where

$$\mathbf{x}_a = \mathbf{K}_a\mathbf{x}, \;\; \mathbf{x}_b = \mathbf{K}_b\mathbf{x}, \;\; \mathbf{x}_c = \mathbf{K}_c\mathbf{x} \tag{1.35}$$

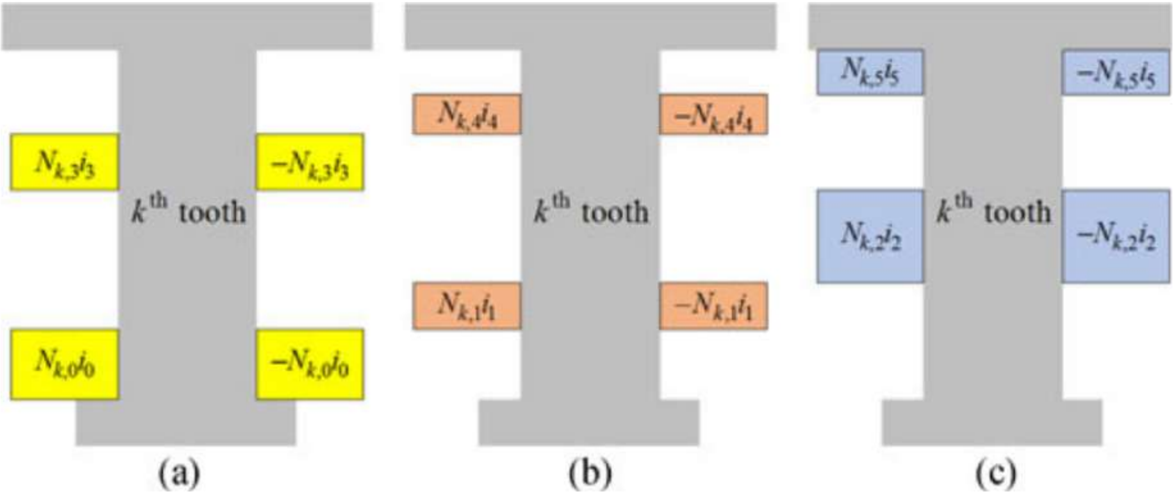

Figure 1.8: k^{th} wound tooth configuration for each phase when the turn vector is equal to **(a)** $\mathbf{x}_a = \mathbf{K}_a\mathbf{x}$; **(b)** $\mathbf{x}_b = \mathbf{K}_b\mathbf{x}$; **(c)** $\mathbf{x}_c = \mathbf{K}_c\mathbf{x}$.

Figure 1.8 illustrates the windings configurations identified by the turn vectors $\mathbf{x}_a$, $\mathbf{x}_b$ and $\mathbf{x}_c$ for the k^{th} tooth where only the turns of phases a, b and c are considered, respectively. As an example, the turn vector $\mathbf{x}_a$ represents the number of turns for sub-phases "0" and "3" which correspond to "a" and"-a" as shown in Figure 1.4. These elements are the same as $\mathbf{x}$ while all the other sub-phases are set to zero turns. By obtaining the dissociated phases turn vectors, the MMF fundamental expression (1.30) can be written as:

$$\begin{aligned} M_{s,fund}(\theta,t) &= Re\{v_p^{-T}(\mathbf{x}_a+\mathbf{x}_b+\mathbf{x}_c)e^{i(\omega t-p\theta)}\} \\ &= M_{fund,a}(\theta,t)+M_{fund,b}(\theta,t)+M_{fund,c}(\theta,t) \end{aligned} \tag{1.36}$$

where $M_{fund,a}(\theta,t)$, $M_{fund,b}(\theta,t)$ and $M_{fund,c}(\theta,t)$ represent the MMF fundamentals produced by the three phases a, b and c individually written as follows:

$$\begin{aligned} M_{fund,a}(\theta,t) &= Re\{v_p^{-T}\mathbf{x}_a e^{i(\omega t-p\theta)}\} \\ &= |v_p^{-T}\mathbf{x}_a|\cos\Big(\omega t-p\theta+arg(v_p^{-T}\mathbf{x}_a)\Big) \end{aligned} \tag{1.37}$$

$$\begin{aligned} M_{fund,b}(\theta,t) &= Re\{v_p^{-T}\mathbf{x}_b e^{i(\omega t-p\theta)}\} \\ &= |v_p^{-T}\mathbf{x}_b|\cos\Big(\omega t-p\theta+arg(v_p^{-T}\mathbf{x}_b)\Big) \end{aligned} \tag{1.38}$$

$$\begin{aligned} M_{fund,c}(\theta,t) &= Re\{v_p^{-T}\mathbf{x}_c e^{i(\omega t-p\theta)}\} \\ &= |v_p^{-T}\mathbf{x}_c|\cos\Big(\omega t-p\theta+arg(v_p^{-T}\mathbf{x}_c)\Big) \end{aligned} \tag{1.39}$$

The winding symmetry constraint is fulfilled when the three sinusoidal waves expressed in (1.37)-(1.39)) are equal in magnitude and phase. That implies the equality of the three complex numbers $v_p^{-T}\mathbf{x}_a$, $v_p^{-T}\mathbf{x}_b$ and $v_p^{-T}\mathbf{x}_c$ such as:

$$\begin{aligned} Re\{v_p^{-T}(\mathbf{x}_b-\mathbf{x}_a)\} &= Im\{v_p^{-T}(\mathbf{x}_b-\mathbf{x}_a)\} = 0 \\ Re\{v_p^{-T}(\mathbf{x}_c-\mathbf{x}_b)\} &= Im\{v_p^{-T}(\mathbf{x}_c-\mathbf{x}_b)\} = 0 \end{aligned} \tag{1.40}$$

In order to include the turn vector $\mathbf{x}$, the winding symmetry constraint could be reformulated considering (1.35) as follows:

$$\begin{aligned} Re\{v_p^{-T}(K_b-K_a)\}\mathbf{x} &= Im\{v_p^{-T}(K_b-K_a)\}\mathbf{x} = 0 \\ Re\{v_p^{-T}(K_c-K_b)\}\mathbf{x} &= Im\{v_p^{-T}(K_c-K_b)\}\mathbf{x} = 0 \end{aligned} \tag{1.41}$$

1.3.5 SPM rotor contribution to the air-gap MMF

At this point, with the air-gap stator MMF being determined, the modelling of the rotor contribution to the machine air-gap MMF is necessary to be incorporated to the optimization procedure.

Several parasitic phenomena are generated by the presence of harmonics in the rotor field which require a rigorous analysis of its harmonic spectrum to reckon the cause of perturbation to be subject of optimization. Given the simplicity of the SPM machine rotor geometry, the rotor field can be presented by means of some analytical expressions mainly based on Fourier series theory as explained in the following.

Firstly, a simplified machine model is considered ; with a smooth rotor where the slot openings are neglected; represented in a cylindrical coordinate system (ρ, θ, z) as shown in Figure 1.9. The first pole axis is taken as a reference for the rotor angular position θ. This simplified model is used only for the purpose of determining the rotor field in order to obtain the waveform purely generated by the rotor magnets without any distortion from the stator slots.

As illustrated in Figure 1.9, τ_m denotes permanent magnet span, τ_p is the pole pitch, h_m is the magnet thickness and δ is the mechanical air-gap width. A parameter c can be introduced as:

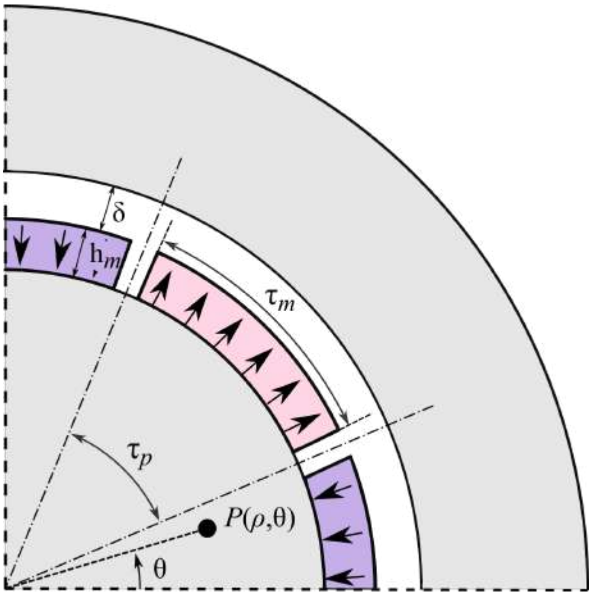

Figure 1.9: Simplified slotless model of SPM machine.

$$c = \frac{\tau_m}{\tau_p} \tag{1.42}$$

where c refers to the magnet to pole span ratio. The permanent magnets are assumed to be uniformly magnetized characterized by radial magnetization pattern. the stator and rotor cores are considered to have infinite permeability.

Based on the previously set assumptions , the MMF produced by the permanent magnets M_r mainly consists of its radial component $M_{\rho,r}$ having a quasi-rectangular waveform alternatively equal to M_{pm} and $-M_{pm}$ as we move along the rotor periphery [24]. The radial component $M_{r,\rho}$ shown in Figure 1.10-(b) at a position of the rotor $\theta = 0$ degrees can be expressed using Fourier series expansion given by:

$$M_{r,\rho}(\theta) = \sum_{n=1,3,5..} \frac{4M_{pm}}{n\pi} \sin\left(\frac{np\tau_m}{2}\right) \cos\left(np\theta\right) \tag{1.43}$$

where M_{pm} is the rotor MMF magnitude generated by the magnets field expressed using the magnets' coercivity H_c as follows:

$$M_{pm} = H_c h_m \tag{1.44}$$

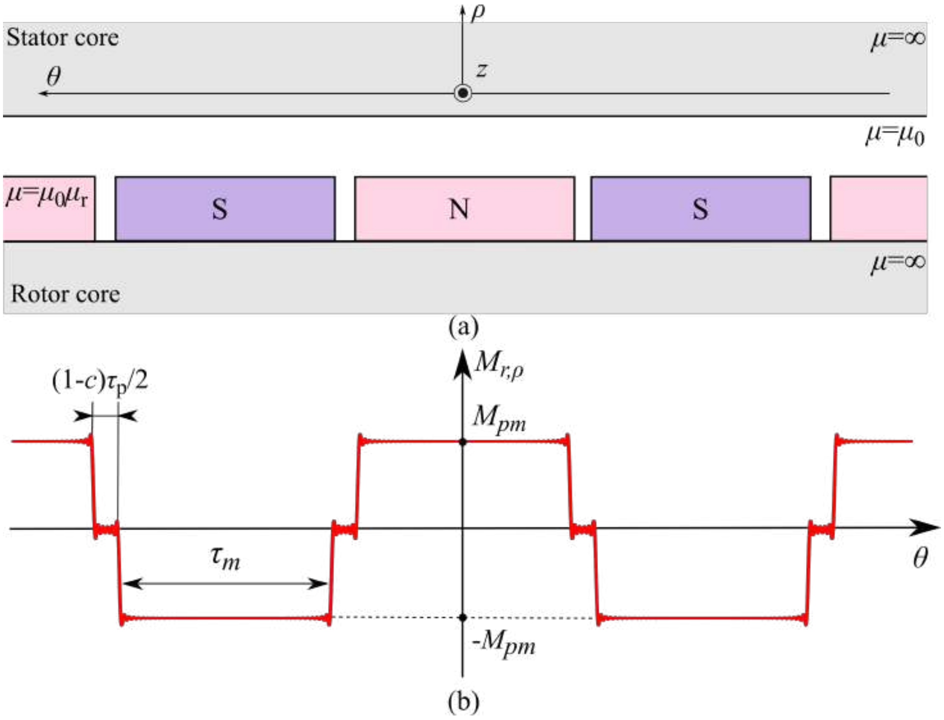

Figure 1.10: (a) Simplified slotless model of SPM machine where the air-gap circumference is unrolled along a straight line; **(a)** Rotor MMF waveform along the angular coordinate θ.

In synchronous steady-state conditions, the rotor revolves at a speed of (ω/p) rad/s, where ω is the stator electrical pulsation. At an instant t, the same waveform of M_ρ as presented in Figure 1.10-(b) is produced but shifted by $(\omega/p)t$. Equation (1.43) can be then rewritten as a function of both time and space as follows:

$$\begin{aligned} M_r(t,\theta) &= \sum_{n=1,3,5..} \frac{4M_{pm}}{n\pi} \sin\left(\frac{np\tau_m}{2}\right) \cos\left[np(\theta - \frac{\omega}{p}t)\right] \\ &= \sum_{n=1,3,5..} m_{r,n} \cos\left[np(\theta - \frac{\omega}{p}t)\right] \\ &= Re\left\{ \sum_{n=1,3,5..} m_{r,n} e^{jnp(\theta - \frac{\omega}{p}t)} \right\} \end{aligned} \tag{1.45}$$

with

$$m_{r,n} = \frac{4M_{pm}}{n\pi} \sin\left(\frac{np\tau_m}{2}\right) \tag{1.46}$$

represents the rotor MMF magnitude for each harmonic order n.

As shown in Figure 1.11, the rotor MMF distribution waveform predicted analytically from equation (1.45) applied to an 8-pole rotor is in a good accordance with FEA results. The harmonic spectrum of such waveform can be computed by means of (1.46) where only harmonics with odd order are displayed (Figure 1.12). Generally, depending on the number of poles p, the order of the non-null rotor MMF harmonics are presented by np where n are odd.

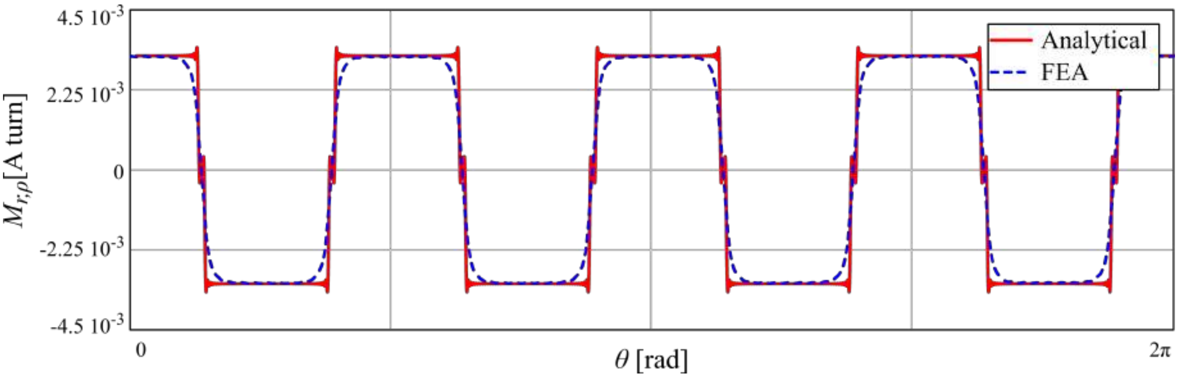

Figure 1.11: Comparison between analytical and FEA results of rotor MMF distribution along the angular coordinate θ of an 8 pole slotless stator SPM machine with magnet coercivity $H_c = 850000$ A/m and $c = 0.95$.

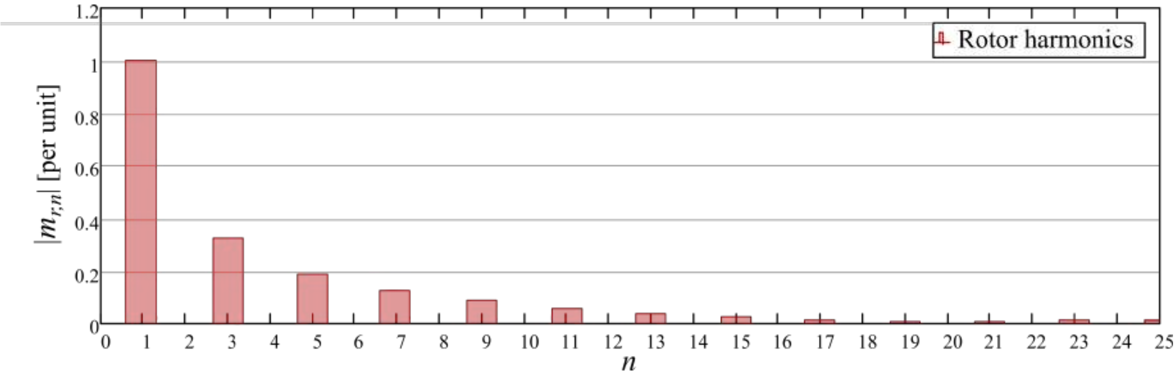

Figure 1.12: Rotor harmonic spectrum where harmonics' magnitude are presented per unit for $p = 1$.

1.4 Quadratic Programming Problem Formulation

By definition, the quadratic programming is a particular type of nonlinear programming that gives the process of solving mathematical optimization problems characterized by a quadratic objective function of several variables subject to linear constraints on these variables [25].
In our case and for the sake of defining the FSCW optimal design, the mathematical equations defined previously will be implemented in the quadratic programming procedure. For this purpose, the objective functions and constraints need to be separately identified.

1.4.1 Objective function

Theoretically, to obtain an optimal design of the multilayer FSCW, two objective functions have to be considered assuming two arbitrarily weighed objectives: one objective is to maximize the MMF fundamental and the other one is to minimize the parasitic behaviour subject to optimization. As explained in [20], the dual objective optimization problem was simplified into a single-objective form through a weighed sum using a weighing coefficient. However, in practice the dependency of the objective function to the weight makes it extremely sensitive to the very slight changes applied on it causing the instability of the process and leading either to unsatisfactory results or the divergence of the algorithm.
To cope with these numerical problems, one solution is to avoid the use of weighing coefficients by only considering a single objective function and assuming the other as a constraint. In our case, the main objective function to be minimized is the one dealing with the parasitic effects. The MMF fundamental maximization can be fixed for each case and moved to the constraints part. In more formal terms, the objective function can be written as:

$$f(\mathbf{x}) = \mathbf{x}^T \mathbf{F}\, \mathbf{x} \tag{1.47}$$

where **F** is $6Z \times 6Z$ symmetric matrix including the information of the quantity to be minimized. This matrix will be determined for each case depending on the optimization purpose in what follows.

1.4.2 Constraints

As mentioned previously, the condition on the MMF fundamental is formalized as a constraint by fixing the MMF amplitude for each optimization iteration. For a given machine ratings, the maximum MMF fundamental that can be obtained occurs when the FSCW topology corresponds to the one produced by the star of slots method. For this case, the turn vector $\mathbf{x}_0$ is determined using the star of slots winding matrix (1.4) presented in Table 1.1 (a) where

$$[\mathbf{x}_0]_{6k+j} = N_{k,j} = W_{k,j} \;\; \forall j = 0..5,\; k = 0..Z-1 \tag{1.48}$$

The MMF amplitude equation (1.23) applied to the fundamental harmonic using the star of slots turn vector $\mathbf{x}_0$ can be rewritten in the complex form as follows:

$$\begin{aligned} m_p^- &= \mathbf{v}_p^{-T}\mathbf{x}_0 = \mathbf{M}\, e^{j\phi} \\ &= \mathbf{M}\cos\phi + j\mathbf{M}\sin\phi \end{aligned} \tag{1.49}$$

where $\mathbf{M}$ is the module of the complex magnitude of the maximum MMF fundamental defined as:

$$\mathbf{M} = \sqrt{\mathbf{x}_0^T \mathbf{H}_p^- \mathbf{x}_0} \tag{1.50}$$

and $\phi = arg(\mathbf{v}_p^{-T}\mathbf{x}_0)$.

The condition on the MMF amplitude can be formulated compactly as follows:

$$\mathbf{A}_1\mathbf{x} = \mathbf{b}_1 \tag{1.51}$$

where $\mathbf{A}_1$ and $\mathbf{b}_1$ are the $2 \times 6Z$ matrix and 2-element vector below:

$$\mathbf{A}_1 = \begin{pmatrix} Re\{\mathbf{v}_p^{-T}\} \\ Im\{\mathbf{v}_p^{-T}\} \end{pmatrix}, \quad \mathbf{b}_1 = \begin{pmatrix} \alpha\mathbf{M}\cos\phi \\ \alpha\mathbf{M}\sin\phi \end{pmatrix} \tag{1.52}$$

with $0 < \alpha \leq 1$ is the reduction weight. The optimization is expected to yield different results depending on the value of the MMF fundamental amplitude. In fact, by varying the value of α, the algorithm generates a different range of solutions $\mathbf{x}$ for each optimization case. For $\alpha = 1$, the generated winding solution has to correspond to the one resultant from the star of slots method. By gradually reducing α, the fundamental magnitude gradually decreases during each iteration of the optimization allowing for the minimization of the objective function. It is to be noted that the value of the MMF phasor ϕ is tuned so that for each iteration of the optimization process, the MMF module corresponds to its maximum.

Another constraint is related to the symmetry of the winding. As explained in paragraph 1.3.4, all the three phases have to produce equal MMF fundamentals and any instant in order for the winding to be symmetric. Based on (1.41), this condition can be expressed in more compact form as follows:

$$\mathbf{A}_2\mathbf{x} = \mathbf{b}_2 \tag{1.53}$$

where $\mathbf{A}_2$ and $\mathbf{b}_2$ are respectively the $4 \times 6Z$ matrix and 4×1 vector below:

$$\mathbf{A}_2 = \begin{pmatrix} Re\{\mathbf{v}_p^{-T}(\mathbf{K}_b - \mathbf{K}_a)\} \\ Im\{\mathbf{v}_p^{-T}(\mathbf{K}_b - \mathbf{K}_a)\} \\ Re\{\mathbf{v}_p^{-T}(\mathbf{K}_c - \mathbf{K}_b)\} \\ Im\{\mathbf{v}_p^{-T}(\mathbf{K}_c - \mathbf{K}_b)\} \end{pmatrix}, \quad \mathbf{b}_2 = \begin{pmatrix} 0 \\ 0 \\ 0 \\ 0 \end{pmatrix} \tag{1.54}$$

The maximum number of turns N_0 which can be wound around one tooth as discussed in paragraph 1.3.1 has to be set as a constraint as well. The condition can be expressed compactly for all the teeth referring to (1.9) and using the turn vector as follows:

$$\mathbf{A}_3\mathbf{x} \leq \mathbf{b}_3 \tag{1.55}$$

where $\mathbf{A}_3$ is the $Z \times 6Z$ matrix and $\mathbf{b}_3$ is the Z-sized vector here under:

$$\mathbf{A}_3 = \begin{pmatrix} \mathbf{1}_{1\times 6} & \mathbf{0}_{1\times 6} & \cdots & \mathbf{0}_{1\times 6} \\ \mathbf{0}_{1\times 6} & \mathbf{1}_{1\times 6} & \cdots & \mathbf{0}_{1\times 6} \\ \vdots & \vdots & \ddots & \vdots \\ \mathbf{0}_{1\times 6} & \mathbf{0}_{1\times 6} & \cdots & \mathbf{1}_{1\times 6} \end{pmatrix}, \quad \mathbf{b}_3 = N_0\mathbf{1}_{Z\times 1} \tag{1.56}$$

with $\mathbf{1}_{m\times n}$ and $\mathbf{0}_{m\times n}$ referring to the $m \times n$-sized unit and zero matrices respectively.

The last constraint represents the convention established in Section 1.3 stating that all the turn vector elements must be greater or equal to zero can be written as:

$$\mathbf{A}_4\mathbf{x} \leq \mathbf{b}_4 \tag{1.57}$$

where

$$\mathbf{A}_4 = \mathbf{I}_{6Z}, \quad \mathbf{b}_4 = \mathbf{0}_{6Z\times 1} \tag{1.58}$$

with $\mathbf{I}_{6Z}$ being the opposite of $6Z \times 6Z$-sized identity matrix and $\mathbf{I}_{6Z\times 1}$ is the $6Z$-sized null vector.

1.4.3 Problem formulation

At this point, the overall FSCW optimization problem can be then presented as follows:

$$\begin{gathered} \mathit{minimize}\ f(\mathbf{x})\ \mathit{subject\ to} \\ \begin{pmatrix} \mathbf{A}_1 \\ \mathbf{A}_2 \end{pmatrix} \mathbf{x} = \begin{pmatrix} \mathbf{b}_1 \\ \mathbf{b}_2 \end{pmatrix}, \begin{pmatrix} \mathbf{A}_3 \\ \mathbf{A}_4 \end{pmatrix} \mathbf{x} \leq \begin{pmatrix} \mathbf{b}_3 \\ \mathbf{b}_4 \end{pmatrix} \end{gathered} \tag{1.59}$$

The objective function $f(\mathbf{x})$ is calculated depending on the case of study. The solution of (1.59) gives an optimal turn vector $\mathbf{x}$ which elements define the optimal FSCW configuration. More precisely; once the solution $\mathbf{x}$ is found; the number of turns $N_{k,j} \geq 0$ on the k^{th} tooth of the j^{th} sub-coil is determined directly from (1.22). The number of turns referring to the physical design of interest (Figure. 1.3-(a)) $N_{k,a}$, $N_{k,b}$ and $N_{k,c}$ for the three coils wound on the k^{th} tooth can be then calculated using (1.11). It may be worth noting that all the matrices $\mathbf{F}$, $\mathbf{A}_{1,2,3,4}$, and $\mathbf{b}_{1,2,3,4}$ do not depend on the machine geometry, as proved by their analytical formulations. Hence, the FSCW layout obtained from the solution of (1.59) is the same irrespective of machine geometry and dimensions.

1.5 Application of the quadratic programming on FSCW SPM machines for different optimization purposes

In what follows, the formulation of the objective function in the quadratic programming form applied to different optimization cases will be presented. Three optimization objectives will be put forward to be minimized: eddy currents magnet losses , UMP and torque ripple.

1.5.1 Machine model used for the optimization

For a comprehensive comparison, a FSCW SPM machine model is built for each machine configuration following a dimensional method which preserves the fundamental flux density produced by both permanent magnets and stator currents regardless of Z and p. To do so, a scaling law (reported in Figure 1.13) has been used.

The machine stack length L is kept constant with $L = 100$ mm. The number of conductors per slot is maintained constant as well as the slot fill factor so that each conductor cross-section changes proportionally to $p^2/(Z \times k_w)$. The fundamental winding factor k_w can be calculated

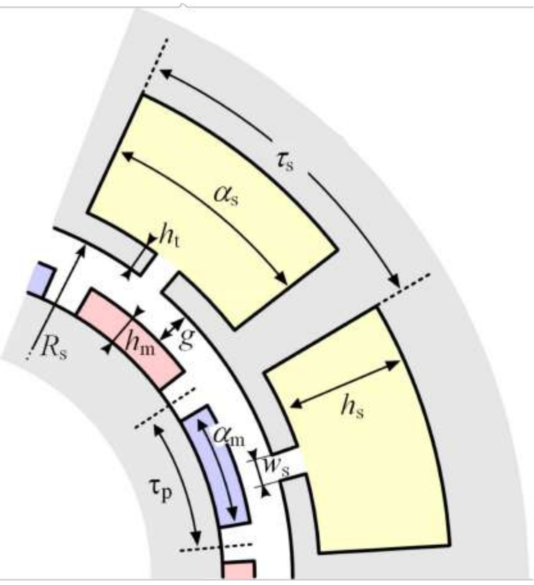

h_s	$10 \times p/k_w$
τ_s	$2\pi/Z$
τ_p	π/Z
α_s	$5/9 \times \tau_s$
w_s	2.5 mm
h_t	2 mm
h_m	$3 \times p$ mm
g	$0.5 \times p$ mm
α_m	$0.95 \times \tau_s$
R_s	$20 \times p$

Figure 1.13: Characteristic dimensions for the example machine.

Table 1.2: Characteristic data for the example machine.

N_0	Number of turns per tooth	100
I_0	Phase peak current	$3 \times 4.4 \times p^2/(Zk_w)$ A
H_c	Magnet coercive force	800 KA/m
σ_m	Magnet conductivity	0.67 MS/m
k_f	Slot fill factor	0.5
f	Stator frequency	50 Hz

easily based on the well-known relation [26]:

$$M_{fund} = \frac{3}{\pi}\frac{k_w}{p}\frac{ZN_0}{3}I_0 \tag{1.60}$$

and given in Table 1.3 for various Z-slot/2p-pole configuration. Only values for which $\frac{1}{4} < q < \frac{1}{2}$ are displayed since this criterion brings to an acceptable winding factor (i.e. grater than 0.7). Hence a constant conductor current density for all slot-pole combinations can be achieved by imposing a phase current equal to $3 \times 4.4p^2/(Z \times k_w)$ A. Consequently, the fundamental of the flux density due to the armature reaction does not change which can be written as:

$$B_{s,fund} = \mu_0\frac{M_{fund}}{g} = \mu_0\frac{3}{\pi}\frac{k_w}{gp}\frac{ZN_0}{3}I_0 \tag{1.61}$$

where $\mu_0 = 4\pi 10^{-7}$ is the permeability of air and M_{fund} is substituted by (1.60). Substituting the expression of the phase current I_0 into (1.61), it is clear that $B_{s,fund}$ is independent of both Z and p.

Besides, by keeping permanent magnet coercive force constant and changing both permanent magnet height and air-gap width proportionally to p, the flux density amplitude due to permanent magnet remains the same regardless of p.

Table 1.3: Winding factor for different slot/pole combinations. Only values for which configurations have $\frac{1}{4} < q < \frac{1}{2}$ are shown.

Number of slots Z	Number of poles $2p$											
	2	4	6	8	10	12	14	16	18	20	22	24
3	0.866	0.866										
6		0.866	\	0.866								
9			0.866	0.945	0.945	0.866						
12				0.866	0.933	\	0.933	0.866				
15					0.866	X	0.951	0.951	X	0.866		
18						0.866	0.902	0.945	\	0.945	0.902	0.866
21							0.866	0.890	X	0.953	0.953	X
24								0.866	X	0.933	0.949	\
27									0.866	0.877	0.915	0.945

1.5.2 Unbalanced magnetic pull minimization

1.5.2.1 Unbalanced magnetic pull: brief review

One important source of deflection in rotating electric machines is the UMP. This phenomenon can be described as an imbalance of the radial and tangential forces acting upon the rotor surface such that a net radial force is developed pulling the rotor away from the stator bore axis [27]. It can be a steady force in one direction, a rotating force vector (often at rotor rotational speed), or a radial vibration [28]. These forces are usually due to rotor eccentricity which can be either static (misplaced rotor but still turning on its own axis maybe due to a misaligned or worn bearing) or dynamic (rotor turning on the stator bore axis but not on its own axis maybe due to a bent shaft) eccentricity [29, 30]. It can also arise due to asymmetries in the windings[31] or electric faults [32]. The study of such a parasitic phenomena is important because it effects the wear of the bearings [33], causes noise and vibration [34] and under extreme conditions may lead to contact between rotor and stator.

A good part of the literature associates UMP to large induction and synchronous machines to be more subject to rotor eccentricity conditions and winding faults. However, smaller machines are also susceptible to UMP even without rotor anomalies especially when FSCW machines are used [35]. In fact, some particular Z-slots/$2p$-poles combinations create some substantial UMP even when the rotor is perfectly centred [8] due to the interaction of induced space harmonics. Several attempts have tackled the development of analytical models to identify the source of UMP in PM motors in order to quantify the frequency of any vibrations coming from rotor misalignment or star asymmetry and electrical faults. However, no attempts regarding the electrical machine optimization in terms of UMP limitation have been reported in the literature. With FSCW being employed, the complexity of the harmonic spectrum of the air-gap flux waves makes it necessary the modelling and investigation of the effect of the harmonics on the UMP.

In the following, an identification of FSCW SMP machines configurations susceptible to UMP due to space harmonics interaction is presented. Then, the application of the optimization quadratic algorithm from Section 1.4 on the identified configuration for the sake of UMP minimisation will be explained.

1.5.2.2 Analytical formulation of the UPM force

UMP is generally calculated analytically by evaluating the global magnetic force that acts on the rotor having an axial length L using the Maxwell's stress tensor method [31]. In our case, a $2D$ model of the machine is considered and the approximation for stress tensor applied on a closed contour in the air-gap is adequate to evaluate the pull force. Thus, the force components F_x and F_y can be computed by evaluating the following expressions along a surface of radius r in the middle of the air-gap [31]:

$$F_x = \frac{rL}{2\mu_0} \int_0^{2\pi} \left[(B_\rho^2 - B_\theta^2) \cos\theta + 2B_\rho B_\theta \sin\theta \right] d\theta \tag{1.62}$$

$$F_y = \frac{rL}{2\mu_0} \int_0^{2\pi} \left[(B_\rho^2 - B_\theta^2) \sin\theta - 2B_\rho B_\theta \cos\theta \right] d\theta \tag{1.63}$$

where B_ρ and B_θ are the normal and tangential components of the flux density B. In many publications the tangential flux density component is most of the time neglected since it is very small, thus it does not significantly affect the pull. Equations (1.62) and (1.63) are then reduced to:

$$F_x = \frac{rL}{2\mu_0}\int_0^{2\pi} B_\rho^2 \cos\theta \, d\theta \tag{1.64}$$

$$F_y = \frac{rL}{2\mu_0}\int_0^{2\pi} B_\rho^2 \sin\theta \, d\theta \tag{1.65}$$

For a straightforward identification of the space harmonics laying behind UMP generation, it is sufficient to concentrate on the stator MMF harmonic spectrum to determine the machine configurations having UMP. For that, equation (1.18) can be implemented in (1.64) and (1.65) to allow their formulation in terms of harmonic order n leading to the following expression of F_x:

$$\begin{aligned} F_x &= \frac{rL\mu_0}{2g^2}\int_0^{2\pi} \left[Re(M_s(\theta,t))\right]^2 \cos\theta \, d\theta \\ &= \frac{rL\mu_0}{2g^2}\int_0^{2\pi} \left\{ \sum_{n=1..\infty} Re\left[m_n^- e^{i(\omega t - n\theta)} + m_n^+ e^{i(\omega t + n\theta)}\right] \right\}^2 \cos\theta \, d\theta \end{aligned} \tag{1.66}$$

where g is the air-gap width. F_y is written in the same way as F_x by substituting the $\cos\theta$ by $\sin\theta$. According to [27], it is proved that UMP is generated by two air-gap flux waves with pole pair numbers differing by one . The relative velocity of the waves will determine the type of the pull whether it is steady or dynamic force. Indeed, if the sum or difference of the two neighbour waves is zero then it results in a steady pull in one radial direction. However, in our case, harmonic couples generated by FSCW space harmonics have different frequencies and are rotating in opposite directions. Thus the sum or difference of their velocities is non null giving the frequency of vibration and resulting in a dynamic pull.

1.5.2.3 Identification of harmonics causing UMP

In FSCW machines, even in absence of rotor eccentricity, radial forces may arise for some configurations having diametrically asymmetric distribution [31]. More particularly configurations characterized by slot/pole combinations in which the slot number Z and the number of poles $2p$ are different by one, i.e., $2p = Z \pm 1$ are characterized by asymmetric disposition of the stator slots and coils [36]. Their corresponding winding distributions are more likely to produce space harmonics with pole pairs differing by one leading to UMP generation.

For a more comprehensive investigation, the space harmonics spectrum of the 9 slots/6 poles-machine as well as the 9 slots/8 poles-machine configuration is presented in Figure 1.14. It can be seen that, for the same number of slot $Z = 9$, while all harmonics of the 6-pole machine are separate (Figure 1.14-(a)), the 8-pole machine (being $2p = Z - 1$) have a harmonic spectrum where all harmonic pole pairs differ by one order and rotate in opposite directions (Figure 1.14-(b)). This certainly generates UMP which is mainly caused by the interaction between fundamental harmonic

$n = p = 4$ and the one right next to it $n = 5$.

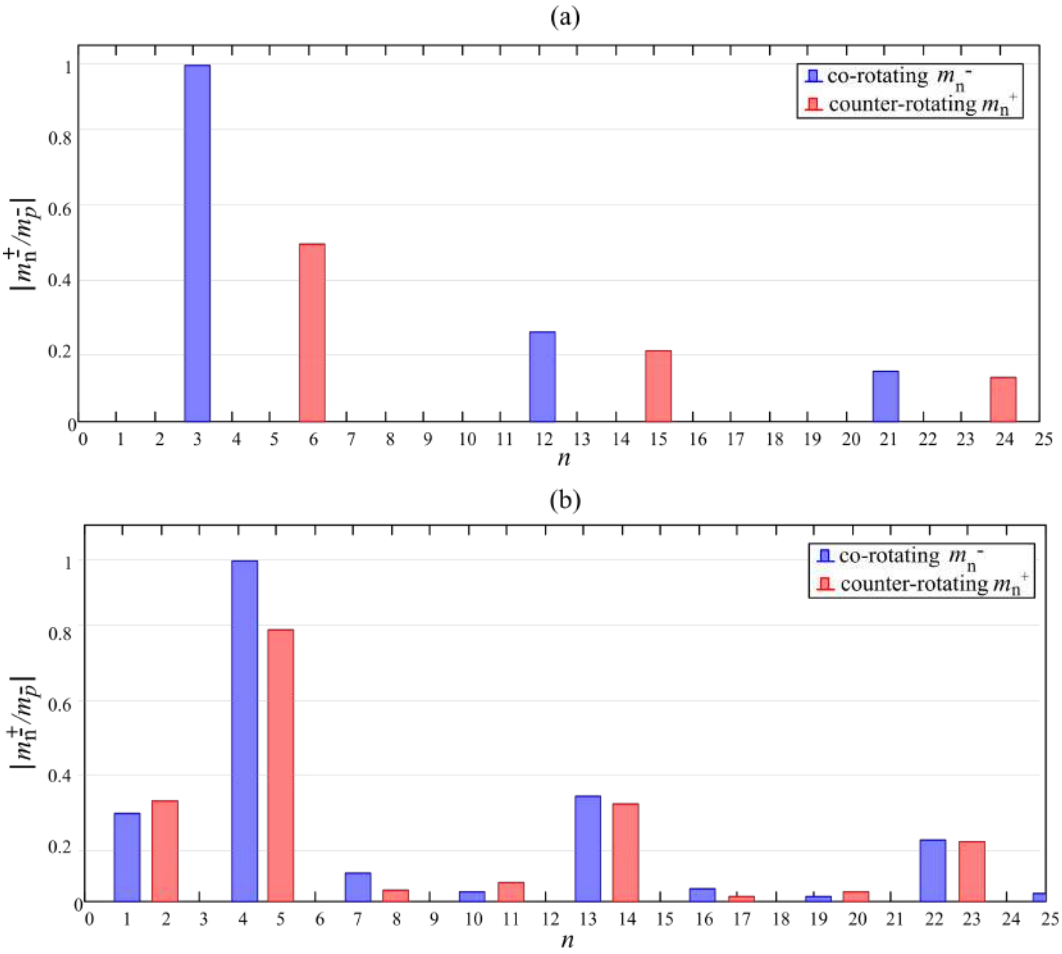

Figure 1.14: MMF stator Harmonic spectra for **(a)** 9 slots/6 poles and **(b)** 9 slots/8 poles configurations.

Following the same reasoning, the harmonic spectrum for each FSCW SPM machine configuration is determined (using (1.19) and (1.20)) and analysed to help identify the most problematic slot/pole combination. Table 1.4 summarizes the UMP status for various machine configurations based on the aforementioned harmonic spectrum analysis. Table cells marked by "X" refer to unconventional configurations which do not fulfill the FSCW feasibility constraint (1.5), i.e. unfeasible with the classical star of slots method.

As can be clearly seen from Table 1.4, there are some other configurations besides those having Z and $2p$ differing by one that can actually suffer from UMP mainly because of the diametrical asymmetry of their windings, e.g. 21- slot/16-pole and 27-slot/20-pole configurations. Conversely, it is noticeable that, for machines including a sequence of repeatable groups of coils and poles, the UMP is null [37] such that the radial forces generated by all groups have zero sum for symmetry reasons [36]. For example, it is well-known that 9-slot/8-pole combination suffers from high UMP since its configuration lacks rotational symmetry. On the other side, negligible UMP is found

Table 1.4: Summary of Z slots/ $2p$ poles combinations which present UMP based on stator space harmonic spectra analysis.

Number of slots Z	Number of poles $2p$										
	2	4	6	8	10	12	14	16	18	20	22
3	**UMP**	**UMP**									
6		no UMP	\	no UMP							
9			no UMP	**UMP**	**UMP**	no UMP					
12				no UMP	no UMP	\	no UMP	no UMP			
15					no UMP	X	**UMP**	**UMP**	X	no UMP	
18						no UMP	no UMP	no UMP	\	no UMP	no UMP
21							no UMP	**UMP**	X	**UMP**	**UMP**
24								no UMP	X	no UMP	no UMP
27									no UMP	**UMP**	**UMP**

for 18-slot/16-pole combination (double of 9-slot/8-pole machine), which enjoy a rotationally-symmetric winding layout.

1.5.2.4 Identification of optimizable configurations

One way to reduce the radial forces is to directly target the harmonics causing UMP. With the machine configurations presenting UMP being identified, it is easier to point out the machine candidates suitable for quadratic optimization. To do so, it is important to verify that the space harmonics to be minimized are not linked to the fundamental. Any reduction applied on the associated harmonics results in a direct proportional decrease in the fundamental harmonic. In fact, all harmonic orders n are related if they satisfy the following relation:

$$n = p\nu \pm iZ \;\; for \;\; i = 0, 1, 2, 3... \tag{1.67}$$

where ν are the harmonic wave orders developed by a two-layer FSCW which can be expressed as [38]:

$$\nu = \begin{cases} \pm\frac{1}{\eta}(6g+2) & if\ \eta\ is\ even \\ \pm\frac{1}{\eta}(6g+1) & if\ \eta\ is\ odd \end{cases} \quad and\ g = 0, \pm1, \pm2, \pm3, ... \tag{1.68}$$

where η being the denominator of the number of slots per pole per phase q ($q = Z/(6p) = z/\eta$). For example, by observing the harmonic spectrum of the 9-slot/8-pole machine (Figure 1.14 (b)), it is clear that the most harmful harmonic in terms of UMP generation is the 5^{th} harmonic having the highest amplitude after the fundamental. However, based on (1.67) it is found that m_5^+ and m_4^- are linked which makes the 9-slot/8-pole configuration unsuitable for optimization even if it generates high pull. Unfortunately, this fact leads to limiting the range of possibly "optimizable" configurations.

To validate the process, the UMP was calculated considering the various slot-pole combinations adopted in Table 1.4. For each of them, a FSCW SPM machine is properly sized and modeled to preserve the same fundamental flux density to insure comparison consistency between the different machine configurations [39]. These are then studied by time-stepping FEA simulating its steady-state operation at rated current in the maximum-torque working point (i.e., with the armature reaction fundamental aligned to the q axis). The specific UMP is then obtained in terms of maximum radial force acting on a cm^2 of stator inner surface. Such a specific UMP constitutes a good index for homogeneously comparing different slot-pole combinations. The specific UMP values obtained from the simulations are shown in Table 1.5.

Table 1.5: Specific UMP in [N/cm^2] for different Z slots/ $2p$ poles combinations.

Number of slots Z	Number of poles $2p$											
	2	4	6	8	10	12	14	16	18	20	22	24
3	1.67	4.52										
6		0	\	0								
9			0	3.96	1.65	0						
12				0	0	\	0	0				
15					0	X	5.59	0.98	X	0		
18						0	0	0	\	0	0	0
21							0	0.16	X	7.86	0.67	X
24								0	X	0	0	\
27									0	1.75	0.1	0

The results shown in Table 1.5 are in accordance with the evaluation of Table 1.4. The known fact of FSCW machines having a rotationally symmetric configuration have practically zero UMP in absence of rotor eccentricity has been confirmed. This is also noted to occur for all the slot-pole combinations for which Z and $2p$ are not relatively prime numbers. Unfortunately, configurations having number of slots and number of poles differing by one have to be avoided even if they exhibit the highest UPM because of the dependence of the harmful harmonics to the fundamental. The highlighted cells corresponding to the 21-slot/16-pole and 27-slot/20-pole configurations are chosen as a subject of winding layout optimization through quadratic programming for UMP minimization.

1.5.2.5 Application examples of the quadratic programming optimization

To verify the validity of quadratic programming in terms of UMP minimization, the problem (1.59) is herein solved for the two example slot/pole combinations which are highlighted in 1.5 (the 21-slot/16-pole and 27-slot/20-pole configurations). The dimensions of the example machines used for each configuration are built based on the scaling law presented in Figure 1.13 and their characteristics follow the data displayed in Table 1.2. For illustrative purposes, the FSCW layouts resultant from the conventional star of slot winding matrices (Figures 1.15-(a) and 1.16-(a)) for both configurations are displayed in Figures 1.15-(b) and 1.16-(b) as well as their corresponding MMF space harmonic spectrum (Figures 1.15-(c) and 1.16-(c)).

a)Winding matrix

	Phases		
Tooth index k	*a*	*b*	*c*
0	100	0	0
1	0	100	0
2	0	−100	0
3	0	0	−100
4	−100	0	0
5	0	−100	0
6	0	100	0
7	0	0	100
8	100	0	0
9	−100	0	0
10	0	−100	0
11	0	0	−100
12	−100	0	0
13	100	0	0
145	0	100	0
15	0	0	100
16	0	0	−100
17	−100	0	0
15	0	−100	0
19	0	0	−100
20	0	0	100

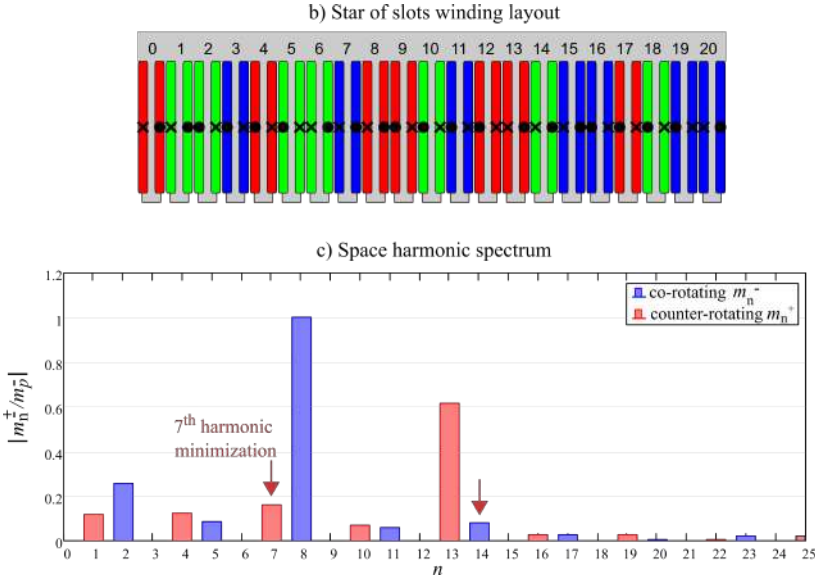

Figure 1.15: 21-slot/16-pole FSCW configuration: **a)** Winding matrix, **b)** winding layout and **c)** space harmonic spectrum.

a)Winding matrix

	Phases		
Tooth index k	*a*	*b*	*c*
0	100	0	0
1	0	100	0
2	0	0	100
3	0	0	−100
4	−100	0	0
5	0	−100	0
6	0	0	−100
7	0	0	100
8	100	0	0
9	0	100	0
10	0	0	100
11	100	0	0
12	−100	0	0
13	0	−100	0
14	0	0	−100
15	−100	0	0
16	100	0	0
17	0	100	0
18	0	0	100
19	100	0	0
20	0	100	0
21	0	−100	0
22	0	0	−100
23	−100	0	0
24	0	−100	0
25	0	100	0
26	0	0	100

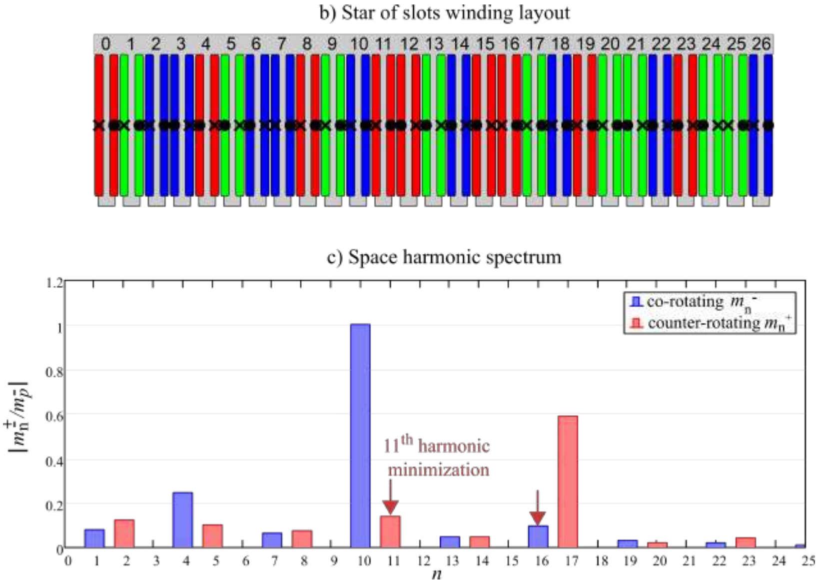

Figure 1.16: 27-slot/20-pole FSCW configuration: **a)** Winding matrix, **b)** winding layout and **c)** space harmonic spectrum.

For instance, Regarding the 21-slot/16-pole configuration, it can be seen that the main generator of UMP are the fundamental harmonic ($n = 8$) and its adjacent one ($n = 7$). Another relevant component of the pull is due to the $13^{th} - 14^{th}$ pair. Referring to (1.67), the minimization can be performed on the problematic harmonic order which consequently leads to a proportional decrease of the linked harmonics. Since the MMF fundamental has to be maximized, the 7^{th} harmonic is targeted in terms of minimization so that the objective function (1.47) is rewritten as:

$$f_{min7}(\mathbf{x}) = \mathbf{x}^T \mathbf{Q}_7^+ \mathbf{x} \tag{1.69}$$

A similar objective function as (1.69) is employed for the case of the 27-slot/20-pole configuration acting on the 11^{th} harmonic order as follows:

$$f_{min11}(\mathbf{x}) = \mathbf{x}^T \mathbf{Q}_{11}^+ \mathbf{x} \tag{1.70}$$

The quadratic algorithm is then solved as a single-objective problem under the linear constraints reported in (1.51), (1.53), (1.55) and (1.57). More particularly, while constraints (1.53), (1.55) and (1.57) are unchanging regardless of the optimization step, the variable α in the constraint (1.51) interpreting the applied decrease on MMF fundamental varies for each optimization iteration, i.e α is set for each optimization iteration so that the quadratic program is solved while guaranteeing the highest MMF fundamental amplitude. As a solution, the optimal winding vector is obtained, and from this, the whole winding layout of the machine with the minimum UMP can be determined by means of (1.21). The winding layout obtained from each optimization step is then applied to the sample SPM machine described in paragraph 1.5.1 and a time-stepping FEA simulations are performed in order to extract the maximum radial force acting on the stator surface. By way of illustration, the harmonic spectra generated by the improved winding layouts are illustrated by superposition in Figures 1.17 and 1.18 to assess the effect of the optimization under several fundamental MMF amplitude constraints. From this it can be clearly seen that a very small decrease of the fundamental MMF amplitude can lead to a significant reduction of the problematic harmonics subject of minimization. Furthermore, it can be confirmed that this gradual decrease is actually seen on the harmonics which are linked by the relation 1.67 in the same proportion.

For the sake of evaluation, the Pareto fronts resulting from the optimization sequence applied on the 21-slot/16-pole and the 27-slot/20-pole configurations illustrating the variation of the UMP with respect to the MMF fundamental percentage are illustrated in figures 1.19 and 1.20 respectively. For each optimization iteration, the MMF fundamental is decreased by 0.1% for both study cases. The minimum UMP is obtained for a fundamental reductions of 2.1% and 2.4% for the 21-slot/16-pole and the 27-slot/20-pole configurations respectively.

For a better visualization of the optimization effect on the UMP, the radial force components

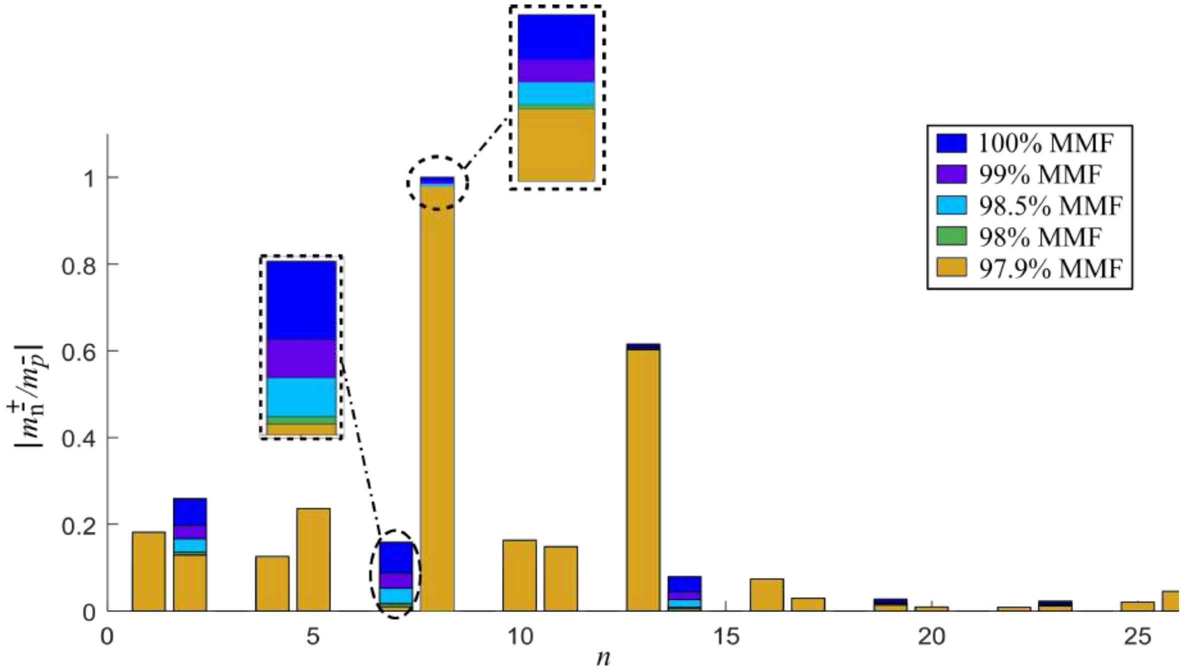

Figure 1.17: Superposition of harmonic spectra corresponding to different optimization steps of the 21-slot/16-pole FSCW configuration.

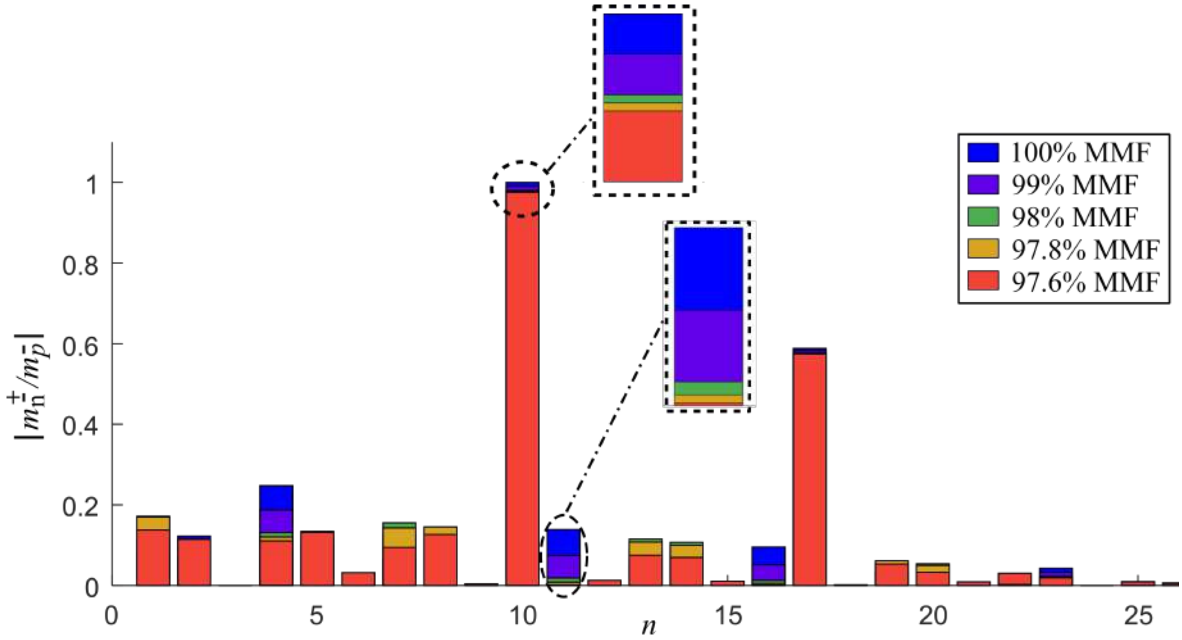

Figure 1.18: Superposition of harmonic spectra corresponding to different optimization steps of the 27-slot/20-pole FSCW configuration.

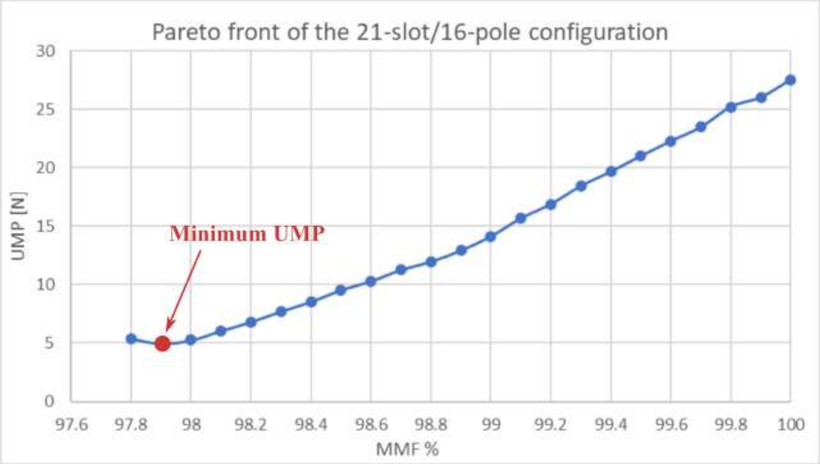

Figure 1.19: Pareto front of the UMP relative variation under quadratic optimization with the minimization of the 7^{th} harmonic as objective function .

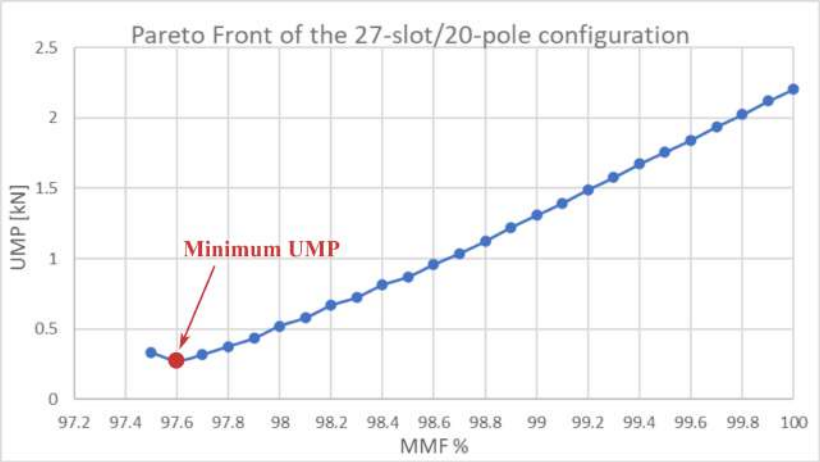

Figure 1.20: Pareto front of the UMP relative variation under quadratic optimization with the minimization of the 11^{th} harmonic as objective function .

F_x and F_y are extracted for each angular position of the rotor obtained from a sequence of magnetostatic FEA simulations forming the UMP trajectory. Such trajectories are compared in Figures 1.21 and 1.22 for a selection of optimization iterations for both studied FSCW configurations.

It can be clearly seen from Figures 1.21 and 1.22 that starting from the conventional star of slot winding configurations (corresponding to 100% fundamental MMF) down to 97.9% fundamental MMF, the area created by the UMP trajectory drastically shrinks which implies a significant decrease of the maximum radial force under the effect of the optimization. Indeed, as it can be drawn out from the Pareto front in Figure 1.19, a slight decrease of the fundamental MMF of just 2.1% has led to an important reduction of the maximum UMP force of 82%. This behaviour is similarly observed for the 27-slot/20-pole configuration in Figure 1.20 where a small decrease of 2.4% of the fundamental MMF engenders a depletion of 87.73% of the maximum radial force. The winding matrices of the optimal solutions for both configurations under study are presented

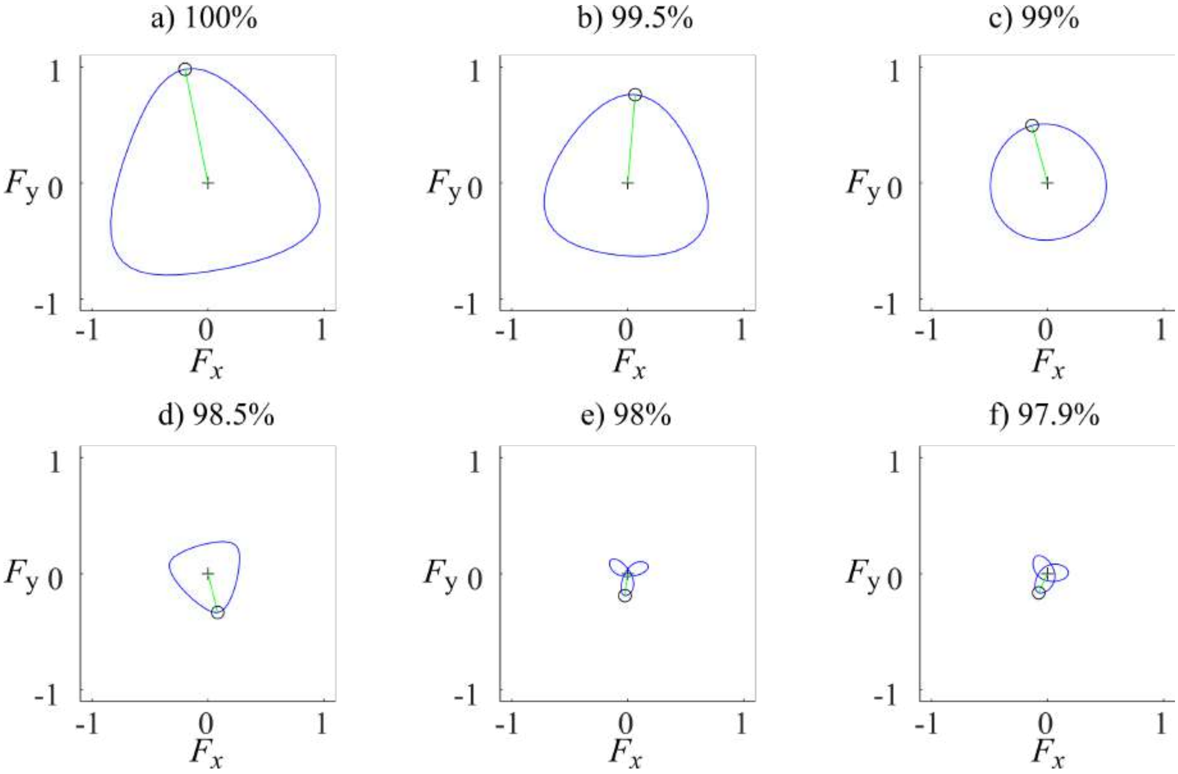

Figure 1.21: Normalized UMP trajectory of the 21-slot/16-pole FSCW configuration for different optimization iterations, the green line refers to the maximum pull force.

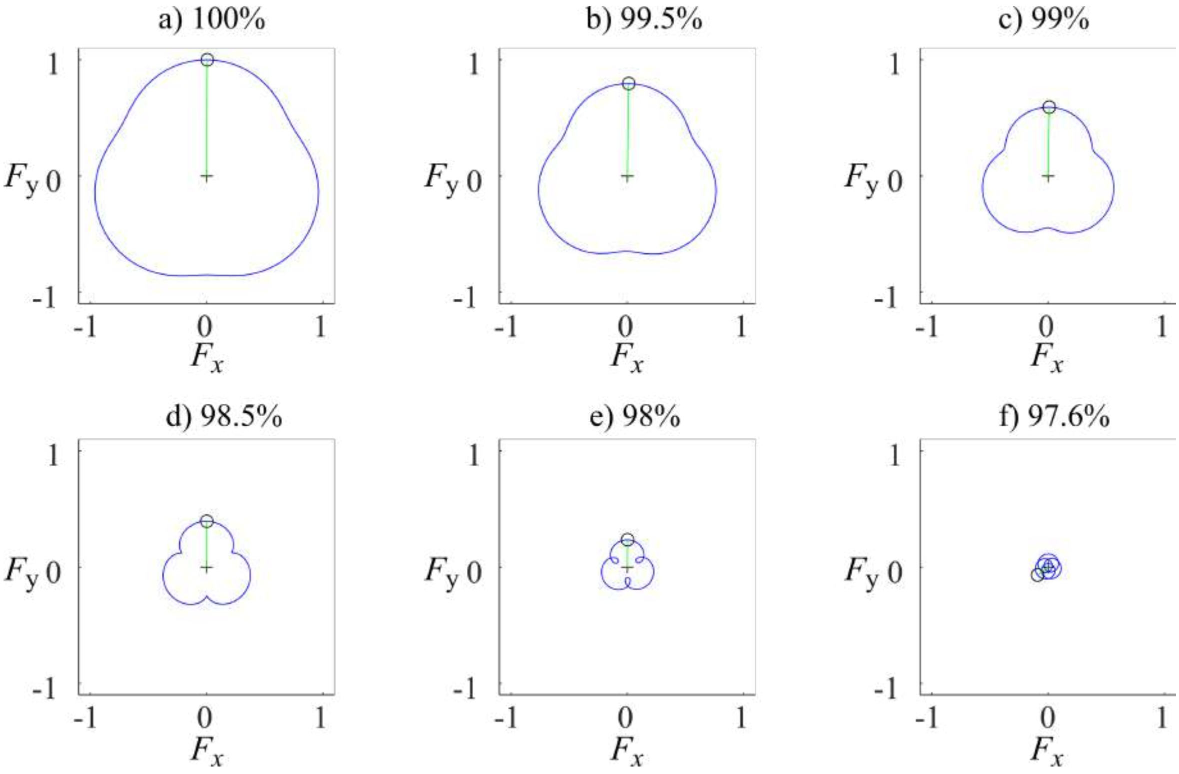

Figure 1.22: Normalized UMP trajectory of the 27-slot/20-pole FSCW configuration for different optimization iterations, the green line refers to the maximum pull force.

in Figures 1.23 and 1.24 together with their winding layouts and their resultant space harmonic spectra. Looking at Figures 1.23 and 1.24, it appears that the minimization of the problematic harmonics is achieved, at the expense of a lowered MMF fundamental, paying the toll of an increased winding complexity as shown in Figures 1.23, 1.24 (a) and (b). The increasing complexity is due to the growth in the number of layers and different coil sizes to be included in the winding design. In fact, the winding structure identified as "optimal" from UMP minimization viewpoint presents two coils of different size with an equal size which are wound around some of the teeth (e.g. #2, #5, #9... for the 21-slot/16-pole configuration). These winding layouts has been never reported in the previous literature, to the author's knowledge, and seems to represent the best solutions for the 21-slot/16-pole and the 27-slot/20-pole configuration FSCW example taken into account in terms of UMP minimization. However, while aiming at diminishing the targeted harmonics, some others arise with a certain proportion to compensate the imposed deficit of the field as can be deduced from Figures 1.17 and 1.18. This increase in amplitude occurring for certain harmonics does not seem problematic in terms of UMP generation until it reaches a certain step from which the UMP starts to rise again (Figures 1.17 and 1.18) which is probably due to the emergence of new harmonics. Another effect of the optimization approach can be noticed looking at Figure 1.24-(c) which shows the appearance of harmonics with the same order but rotating in different directions (e.g. harmonic #7, #13,... for the 27-slot/20-pole configuration. This phenomena does not seem to have a negative impact on the performance of the machine regarding the UMP generation however it may cause other issues that needs to be studied and taken into account (e.g. generation of torque ripple).

a)Winding matrix

Tooth index k	*Phases*		
	a	*b*	*c*
0	0	−100	0
1	0	0	−100
2	−94	0	6
3	100	0	0
4	0	100	0
5	0	−94	6
6	0	0	−100
7	−100	0	0
8	0	−100	0
9	0	6	−94
10	0	0	100
11	100	0	100
12	−94	6	0
13	0	−100	0
14	0	0	−100
15	−100	0	0
16	6	−64	0
17	0	100	0
15	0	0	100
19	6	0	−94
20	−100	0	0

b) Optimized winding layout (97.9% MMF)

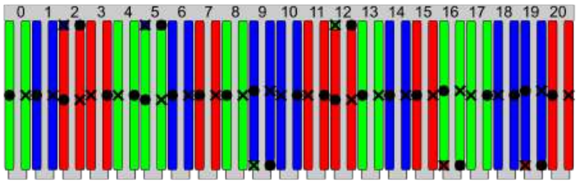

c) Space harmonic spectrum

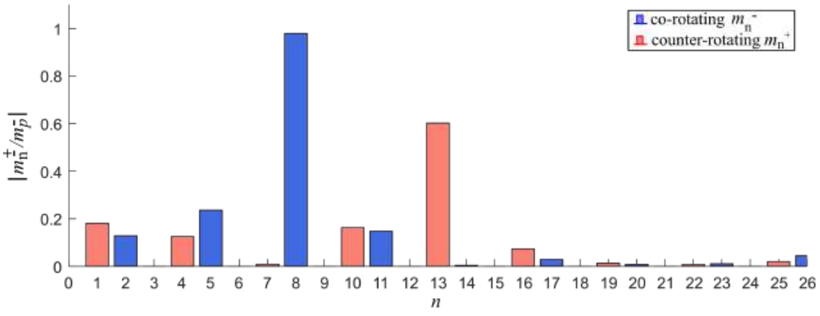

Figure 1.23: 21-slot/16-pole FSCW optimized configuration corresponding to 97.9 % of fundamental MMF: **a)** Winding matrix, **b)** winding layout, and **c)** space harmonic spectrum.

a)Winding matrix

Tooth index k	*Phases*		
	a	*b*	*c*
0	100	0	0
1	0	100	0
2	0	−68	32
3	26	0	−74
4	−100	0	0
5	0	−100	0
6	0	37	−63
7	−100	0	0
8	100	0	0
9	0	100	0
10	0	0	100
11	0	0	−100
12	−74	26	0
13	0	−100	0
14	0	0	−100
15	−74	0	26
16	0	−100	0
17	0	100	0
18	0	0	100
19	100	0	0
20	−100	0	0
21	0	−63	37
22	0	0	−100
23	−100	0	0
24	26	−74	0
25	0	32	−68
26	0	0	100

b) Optimized winding layout (97.6% MMF)

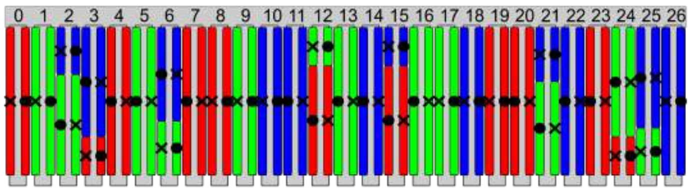

c) Space harmonic spectrum

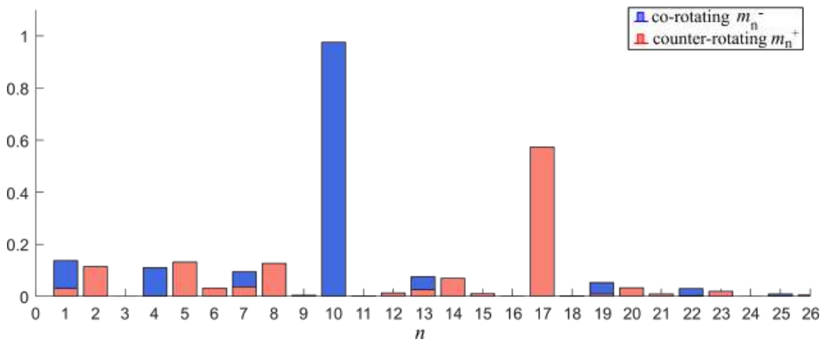

Figure 1.24: 27-slot/20-pole FSCW optimized configuration corresponding to 97.6 % of fundamental MMF: **a)** winding matrix, **b)** winding layout and **c)** space harmonic spectrum.

1.5.3 Torque ripple minimization

1.5.3.1 A brief review on torque ripple minimization techniques

Working on FSCW machines can be challenging given the type of winding topology which suffers from rich MMF space harmonic content causing additional parasite effect. For example, an improper slot/pole combination with inconvenient winding choice can create a very high harmonic content generating an excessive torque ripple. This could be unallowable especially for some specific applications such as electrical power steering systems, servo motors and direct-drive wind power generators for which a very low torque ripple is required [2, 40]. Two main components of torque pulsation can be defined as follows:

- cogging torque, caused by the magnetic interaction between the rotor PMs and stator slotted iron structure,
- torque ripple, which occurs as a result of the interaction between the rotor field distribution and the armature MMF distribution. In SPM motors with FSCW stator topology, the probability of interaction of the stator MMF space harmonics with the rotor field is even more frequent due to the high harmonic content of the stator's winding.

For that it exists an extensive literature with various techniques for minimizing torque pulsation for this type of machine. It can be found that some researchers dealt with the torque pulsation problem from the control view-point [41, 42] while some others rely on machine design concepts [43–47].

For example, the third harmonic has gained wide applications in the machine control and even in the machine design for ameliorating the quality of the output torque. In [41, 42], third harmonic currents which interacts with the third harmonic electromotive force (EMF) was injected to the windings of a multiphase machine to improve the torque capability in multi-phase machine. In three phase machines the third harmonic current cannot be injected. Alternatively, a radial sine-shaped PM with additional third order harmonic is used to reduce the torque ripple [43]. The existence of the third harmonic improves the fundamental in the magnetic loading, which is analogous to the third-harmonic current injection in the motor drive. However, the radial pole-shaping have negative impact on the torque production and shows some residual torque ripple with vulnerability to demagnetization near the magnet edge. Axial magnet shaping technique was proposed in [44] to overcome the demagnetization issue and preserve the magnet thickness in the radial direction while achieving high torque density with essentially zero torque pulsation. In spite of its advantages, PM shaping method adds more complication to the design of the machine which increases the manufacturing cost, reduces the yield of the material and decreases in anyway the output average torque.

Skewing is another effective method to suppress the torque ripple [45]. However, a minimal skewing stacks are generally adopted in industrial application designs given the complexity of the manufacturing process. Consequently, the practical effectiveness of this method could be limited. Furthermore, even if it is sufficient to cancel cogging torque, skewing technique in not appropriate for the reduction of harmonics causing electromagnetic torque ripple in FSCW SPM machines.

From the stator side, it was proven that; with a proper modification of some geometrical parameters and winding layout; a reduction of some harmonic orders of the stator field lying behind the generation of torque ripple could be achieved. For example, unequal teeth width design is proposed to reduce the sixth order torque variation of 12-slot/10-pole FSCW machine [46]. The teeth width adjustment method aims at decreasing the effect of local saturation in the stator caused by the non-symmetrical peak flux density distributions in the stator teeth which can produce some high-order harmonics in the SPM machine torque. However, the main disadvantage of this method is that it decreases the ripple only at the maximum torque per ampere (MTPA) point whereas for other loads it is not effective. It could be noted that the majority of the previously mentioned torque pulsation minimization technique were based on machine design concepts which inevitably complicate the manufacturing process.

To avoid complexity in the motor design, several provisions have been proposed in the literature dealing with FSCW winding layout to act on the MMF harmonic content in order to reduce the effect of harmful harmonics generating torque pulsation. In [10], a space shifted star-delta winding is proposed to minimize the interactive space harmonics and on-load cogging torque associated in 12-slot/10-pole FSCW machine to improve the torque quality. this strategy can achieve better ripple performance depending on the slot/pole combination without having any complex magnet shapes in the rotor. However, the torque producing component is also reduced by 10 to 12%.

Lately, the adoption of multi-layer arrangements has been considered as a promising method widely introduced in the literature to lower or even cancel the FSCW MMF harmonics causing torque perturbations [12, 15, 16]. As a study case and for the sake of torque ripple minimization, a four layer FSCW with unequal coils has been proposed in [16] for a 12-slot/10-pole IPM machine to reduce armature reaction induce space harmonics. However, to achieve a minimum torque ripple using this method, winding optimization was allied with a rotor flux barrier optimization in order to achieve a ripple reduction of 1.4% with the expense of an average torque decrease of 7%. Whereas the aforementioned method adopted multi-layer technique from the stator side, the optimization focused on IPM machines topology which has different behaviour toward torque ripple generation compared to SPM machines.

On the other hand, it is not certain that the proposed multilayer winding solutions can be considered as "optimal" in terms of reducing torque pulsations or if they can be actually further improved through some different changes in the stator winding layout. For this purpose, the potentiality of the quadratic optimization approach previously introduced will be evaluated in what follows in terms of torque pulsation reduction for different slot-pole combinations of FSCW SPM machines. The most problematic configuration producing the highest torque ripple will be directly targeted for which an optimal solution can be generated.

1.5.3.2 Torque analytical formulation in SPM machines

Generally SPM machines are fed by sinusoidal current source to have ideal ripple free torque. However the distortion from the ideal condition results in torque pulsation. One way to compute analytically the machine torque in load condition is to apply Lorentz force law along the air gap surface which leads to an expression of the instantaneous total electromagnetic torque as [48]:

$$\begin{aligned} T_{em} &= R_{med} L \int_0^{2\pi} B_{gap}\, dM_s \\ &= p\frac{\mu_0}{g} R_{med} L \int_0^{2\pi} (M_r + M_s) \frac{dM_s}{d\theta}\, d\theta \\ &= p\frac{\mu_0}{g} R_{med} L \left\{ \int_0^{2\pi} M_r \frac{dM_s}{d\theta}\, d\theta + \int_0^{2\pi} M_s \frac{dM_s}{d\theta}\, d\theta \right\} \end{aligned} \tag{1.71}$$

where R_{med} is the air-gap radius, B_{gap} is the air-gap flux density and M_s and M_r are the stator and the rotor MMF contributions respectively referring to equations (1.18) and (1.46). It follows from the machine periodicity that

$$\int_0^{2\pi} M_s \frac{dM_s}{d\theta}\, d\theta = \left[\frac{1}{2} M_s^2(\theta) \right]_0^{2\pi} = 0 \tag{1.72}$$

On the other hand, to facilitate the computation, it is convenient to substitute the term $\dfrac{dM_s}{d\theta}$ by its Fourier expansion by applying the spatial derivative on equation (I.18) which can be computed as follows:

$$\begin{aligned}\frac{dM_s}{d\theta} &= \sum_{n=1..\infty} -n|m_n^-|sin(\omega t - n\theta + \arg(m_n^-)) + n|m_n^+|sin(\omega t + n\theta + \arg(m_n^+)) \\ &= \sum_{n=1..\infty} \mp n|m_n^\mp|sin(\omega t \mp n\theta + \arg(m_n^\mp))\end{aligned} \tag{I.73}$$

Replacing $\dfrac{dM_s}{d\theta}$ and M_r in (I.71) by their Fourier expansions from (I.73) and (I.46) yields to the reformulation of the electromagnetic torque equation:

$$T_{em}(t) = A \sum_{n=1,3,5..} n|m_n^\mp|m_{r,n} \sin\left((n \pm 1)\omega t + \arg(m_n^\mp)\right) \tag{I.74}$$

where

$$A = p\frac{\mu_0}{g}R_{med}L\pi \tag{I.75}$$

By separating the fundamental from the harmonic components and considering the first harmonic as the fundamental component, it is possible to define the average torque $T_{em,1}$ as

$$T_{em,1} = A|m_1^-|m_{r,1} \sin\left(\arg(m_1^\mp)\right) \tag{I.76}$$

and the ripple torque by

$$T_{ripple} = A \sum_{\substack{h=6n\pm 1\\ n=1,2,3..}} h|m_h^\mp|m_{r,h} \sin\left((h \pm 1)\omega t + \arg(m_h^\mp)\right) \tag{I.77}$$

Using (I.76) and (I.77), the ratio of the ripple torque to the average torque is

$$\frac{T_{ripple}}{T_{em,1}} = \frac{1}{\sin(\arg(m_n^\mp))} \sum_{\substack{h=6n\pm 1\\ n=1,2,3..}} h\left(\frac{|m_h^\mp|}{|m_1^-|}\right)\left(\frac{m_{r,h}}{m_{r,1}}\right) \sin\left((h \pm 1)\omega t + \arg(m_h^\mp)\right) \tag{I.78}$$

From this compact expression it can be clearly proved that the torque ripple is the result of the interaction between the stator and the rotor MMF harmonics of the same order. Based on this formulation and under the idealized assumption of no magnetic saturation and no slotting effect, an analytical Torque Ripple Index (TRI) reflecting the amplitude of the torque ripple can be defined as follows:

$$TRI = \sum_{\substack{h=6n\pm 1\\ n=1,2,3..}} h\left(\frac{|m_h^\mp|}{|m_1^-|}\right)\left(\frac{m_{r,h}}{m_{r,1}}\right) \tag{I.79}$$

This tool can be used analytically to compare the ripple performance among various designs. With FSCW SPM machines being considered, the TRI can be a very useful tool to identify the configurations susceptible to generate torque ripple since it allows a straightforward prediction of the torque pulsation based on the space harmonic spectra of both the rotor and stator while avoiding the use of time consuming FEA simulations.

1.5.3.3 The cogging torque

The cogging torque in SPM machines is known to be independent from the winding layout. It is due to the position dependent reluctance variation and interaction between the PM flux with the stator lamination. However, it strongly depends on slot-pole combination, as well as on other design features like the slot opening width, the magnet to pole span ratio and the stator or rotor skew [45].

The cogging torque of a motor can be assumed as the summation of the interactions of each edge of the rotor PMs with the slot openings which can be expressed as [10]:

$$T_{cogging}(\theta) = \sum_{n=1}^{\infty} T_{c,n} \cos(nZ\theta) \tag{1.80}$$

where $T_{c,n}$ is the amplitude of the cogging torque components at the n^{th} cogging frequency. With special regard to the slot-pole combination, it is proved that the cogging torque is proportional to the following parameter [49]:

$$C_T = \frac{Z \times 2p}{LCM(Z, 2p)} \tag{1.81}$$

where $LCM(Z, 2p)$ is the least common multiple of Z and $2p$. The amplitude of the cogging torque goes down as $LCM(Z, 2p)$ increases. Slot pole combinations characterized by a large C_T are unfavourable in terms of cogging torque, while those having $C_T = 1$ (The lowest possible value) are preferred.

Since the adopted optimization technique acts principally on the winding arrangement, the cogging torque will not be affected. In other words, changing the winding layout will solely influence the space harmonic distribution along the airgap. Hence, the cogging torque will not be considered in the optimization procedure. In what follows, the TRI will be considered as an adequate tool to identify the machine configurations suffering from high torque pulsations.

1.5.3.4 Identification of torque ripple sources in FSCW SPM machines

Based on the TRI previously presented in (1.79), it is possible to evaluate the behaviour of different slot/pole combinations in terms of torque pulsation. For a more comprehensive comparison, the TRI for several FSCW SPM configurations is calculated and presented in Table 1.6. In order to identify the machine configurations suitable for optimization by quadratic programming, a first

Table 1.6: Torque Ripple Index (TRI) for different Z slots/ $2p$ poles combinations.

Number of slots Z	Number of poles $2p$											
	2	4	6	8	10	12	14	16	18	20	22	24
3	0.631	0.451										
6		0.451	\	0.367								
9			0.407	0.039	0.035	0.308						
12				0.367	0.022	\	0.022	0.185				
15					0.308	X	0.048	0.034	X	0.185		
18						0.308	0.026	0.027	\	0.027	0	0
21							0.308	0.012	X	0.035	0	X
24								0.185	X	0.013	0	\
27									0.185	0.018	0	0

check on the stator MMF space harmonics interdependence is made for each machine configuration based on (1.67). The highlighted cells of Table 1.6 correspond to the slot/pole combinations presenting stator MMF harmonics which are not linked to the fundamental harmonic. These configurations are referred to by "optimizable".Thus, acting on these harmonics can be feasible without affecting the average torque which is directly dependent on the fundamental component.
A second step is to identify which are the harmonics directly responsible for generating torque ripple, i.e. the ones interacting with the rotor harmonics. The cancellation or reduction of these problematic harmonics will help reducing the torque ripple. Table 1.6 gives an idea of how much ripple can a certain slot/pole combination present from which we can notice that the "optimizable" configurations are not necessarily the ones having the highest torque ripple. Indeed, it can emerge that the configurations that may present low torque ripple are those characterized by a close number of slots and number of poles. Moreover, it can be also noticed that the higher are $2p$ and Z the less is the generated torque ripple. Unfortunately, it can be deduced from the identification process that configurations suffering from the highest torque ripple are excluded from the range of possible "optimizable" configurations.

For illustrative purposes, a comparison of rotor and stator harmonic spectra for the 9-slot/6-pole, 9-slot/8-pole and the 12-slot/10-pole configurations are presented in Figure 1.26. For the sake of a clearer explanation, the common order harmonics between the rotor and stator spectra are highlighted. For example, by looking at Figure 1.26-(a) of the the 9-slot/6-pole machine harmonic spectrum, it can be seen that the 15^{th} and 21^{th} orders present common harmonics between rotor and stator characterised by a significant amplitude and producing a 6^{th} order ripple (which can be shown by its corresponding torque waveform in red in Figure 1.25 presenting 3 periods of pulsation during half of the machine electrical period). However, these harmonics cannot be minimized since they are connected to the fundamental harmonic, thus the 9-slot/6-pole configuration will not be considered for the optimization. In the other hand, by looking at Figure 1.26-(b), the 20^{th} harmonic order of the 9-slot/8-pole which contributes to creating torque ripple is actually independent from the fundamental harmonic. This fact makes it possible to consider the aforementioned configuration as suitable candidate with regard to quadratic optimization.

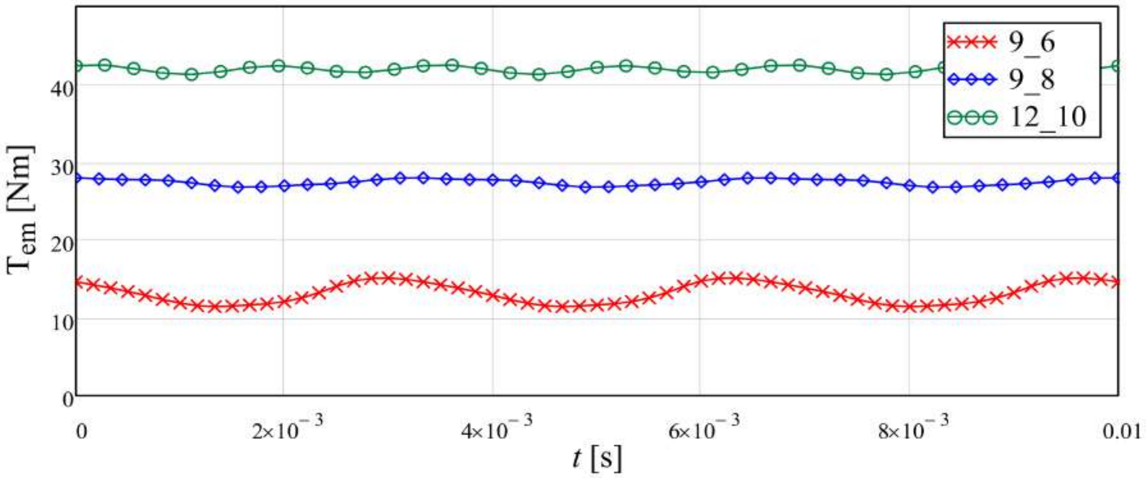

Figure 1.25: Torque waveforms for three different FSCW machine configurations: 9-slot/6-pole (red), 9-slot/8-pole (blue), and 12-slot/10-pole (green).

It is worth noting that, even if one machine configuration is regarded as "optimizable", it may present torque ripple which is caused by harmonic orders that are related to the fundamental, hence cannot be minimized. In fact, referring to Figure 1.26-(c), the 6^{th} and 12^{th} order variations in the torque of the 12-slot/10-pole machine are due to the interaction of common space harmonics of 25^{th}, 35^{th}, 55^{th} and 65^{th} orders which exist in both rotor and stator MMFs. However it can be clearly seen from Figure 1.25 that the 12^{th} order variation is the one characterizing the torque pulsation. This can prove the fact that higher order MMF harmonic components can disproportionately contribute to the torque ripple amplitude. Mathematically speaking, as noted in (1.78), the differentiation operation causes each stator MMF harmonic $m_h^{\mp}$ to be amplified by its harmonic order h.

Based on the previously explained identification process, The FSCW SPM machine configurations suitable for optimization can be easily determined. To assess the applicability of the quadratic programming, the 9-slot/8-pole configuration is chosen in what follows to be the object of optimization in terms of torque ripple minimization.

a) 9-slot/6-pole configuration

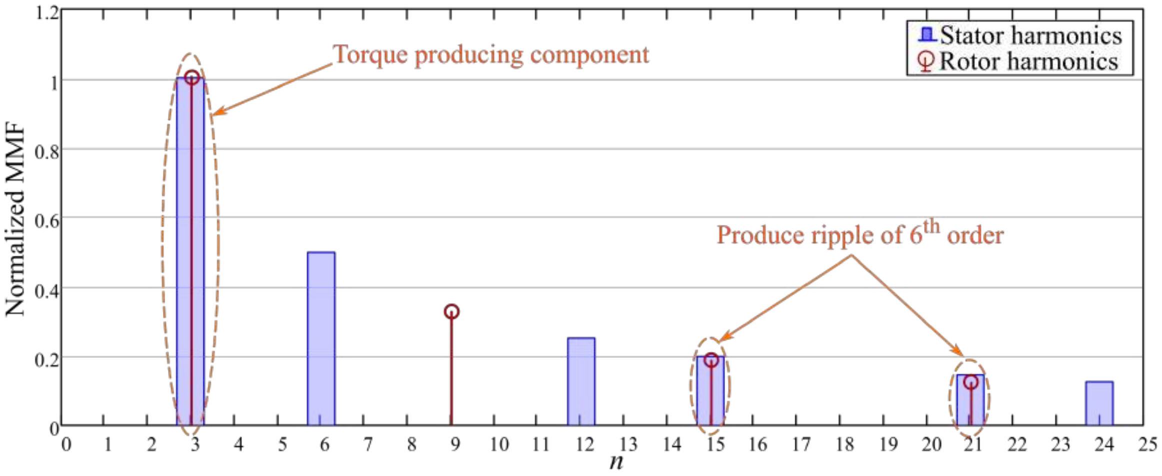

b) 9-slot/8-pole configuration

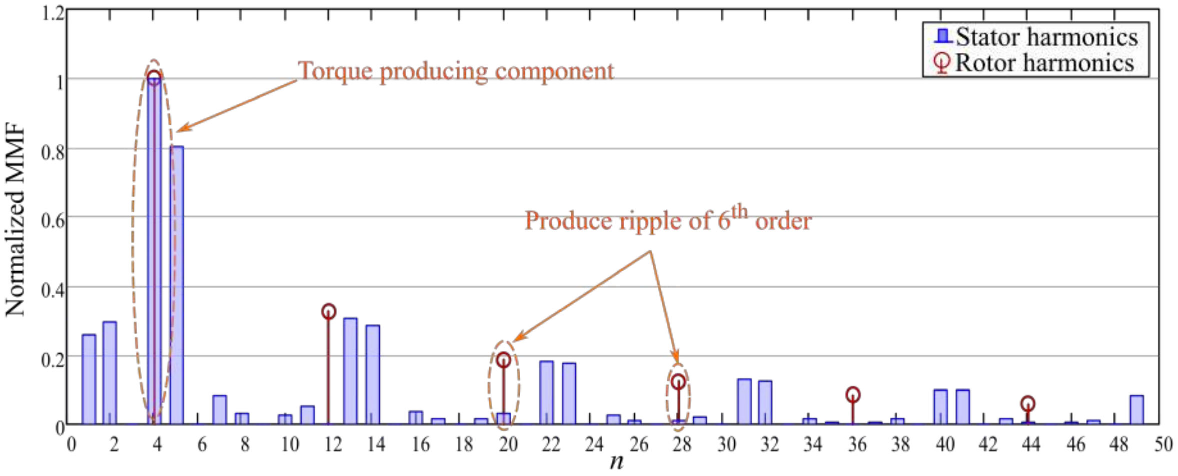

c) 12-slot/10-pole configuration

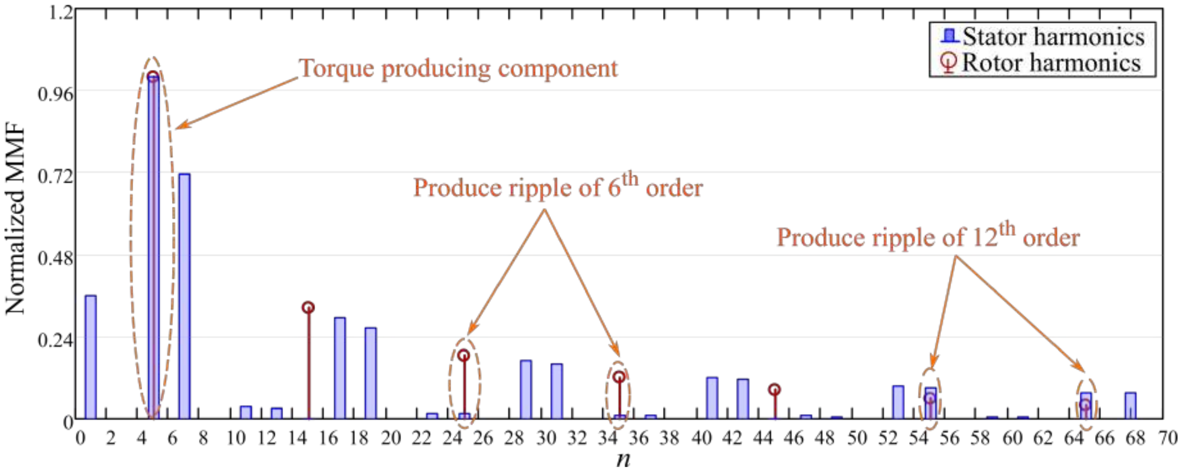

Figure 1.26: comparison of rotor and stator harmonic spectra of several FSCW configurations: **a)** 9-slot/6-pole configuration, **b)** 9-slot/8-pole configuration, and **c)** 12-slot/10-pole configuration.

1.5.3.5 Application example of the quadratic programming optimization

An application example is illustrated for the proposed algorithm (in section 1.4) to the 9-slot/8-pole FSCW SPM machine characterized by the data listed in Table 1.7. The same optimization methodology adopted in paragraph 1.5.2.5 for the sake of UMP minimization will be followed here to reduce the torque pulsation. Based on the spectrum analysis previously performed in 1.5.3.4 and looking at Figure 1.26-(b), the source of torque ripple generator has already been identified which mainly corresponds to the 20^{th} space harmonic order. For illustrative purposes, the minimization will be performed on the 2^{nd} sub-harmonic for the sake of a clear visualization of the optimization effect on the space harmonic spectrum. In fact, referring to (1.67), the 2^{nd} and the 20^{th} harmonics are actually linked so that both of them are effected proportionally. Thus, the quadratic programming problem is implemented and solved considering the following objective function:

Table 1.7: Characteristic data of the example 9-slot/8-pole FSCW machine

Z	Number of slots	9	N_0	Maximum number of turns per coil	100
p	Number of pole pair	4	I_0	Peak value of stator current	8 A
R_s	Stator bore radius	55 mm	f	Stator frequency	50Hz
h_m	PM height	4 mm	μ_0	Magnet permeability	$4\pi 10^{-7}$ H/m
g	Air gap width	2 mm	σ_m	Magnet electrical conductivity	0.667 MS/m
L	Core length	85 mm	c_m	Magnet to pole span ratio	0.95
H_c	Magnet coercivity	850 A/mm	k_f	slot fill factor	0.5

$$f_{min2} = \mathbf{x}^T \mathbf{Q}_2^+ \mathbf{x} \tag{1.82}$$

under the linear constraints reported in (1.51), (1.53), (1.55) and (1.57). For each optimization iteration, a 1% decrease of the fundamental MMF is performed and the corresponding winding vector is obtained as a solution from which the winding design can be determined by means of (1.21).

In order to evaluate the performance of the various optimization solutions in terms of torque pulsation, the winding layouts resultant from optimization process are applied to the example machine model which characteristics are presented in Table 1.7 and a time stepping FEA simulations are performed. For each winding design, the machine model is built and a simulation at steady state is performed at the maximum torque working point. The torque waveform is then extracted as well the ripple and the average torque. For a comprehensive comparison, the percentage of torque ripple for each design solution is calculated based on the FEA simulation results following the relation:

$$Torque\ Ripple = \frac{T_{p-p}}{T_{avg}} \times 100 \quad \% \tag{1.83}$$

where T_{p-p} is the peak-to-peak torque and T_{avg} is the average torque. The Pareto front illustrated in Figure 1.27 summarizes the variation of the torque pulsation under the effect of quadratic optimization. FEA-based torque ripple results variation is presented together with the analytical TRI

for each optimization step. It clearly emerges that both analytical and FEA analytical results show the same behaviour under the effect of MMF fundamental decrease. This assessment demonstrates the effectiveness of the TRI as a straightforward analytical tool in predicting the torque ripple behaviour without relying on time consuming FEA simulations. The gap between the resultant curves is due to the effect of cogging torque which is not taken into account in the analytical TRI formulation.

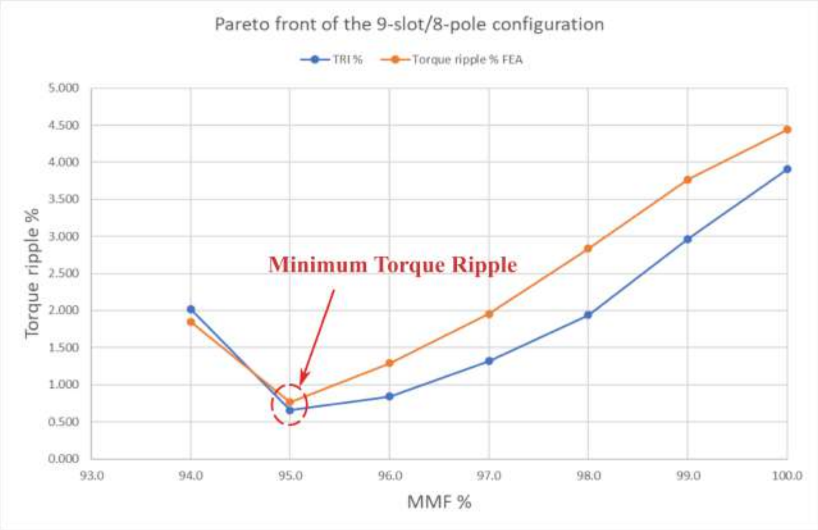

Figure 1.27: Pareto front of the torque ripple relative variation subject to quadratic optimization with the minimization of the 2^{nd} sub-harmonic as objective function.

Based on Figure 1.27, it appears that the torque ripple reduction from 4.5% to 0.7% can be achieved at the expense of 5% fundamental MMF decrease. For the sake of a clearer evaluation, The resultant stator MMF harmonic spectra for each optimization solution are superimposed in Figure 1.28. This latter confirms that the small reduction of 5% on the fundamental MMF (therefore a decrease in the average torque by the same percentage (Figure 1.29)) engenders a significant reduction on the problematic harmonic ($n = 20$) resulting in a decrease of 84.4% in the torque ripple.

The winding matrices and their corresponding winding layouts of the conventional star of slots and the optimal solution are displayed in Figure 1.30. A comparison between the harmonic spectra of the conventional star of slots machine and the optimal machine solution is illustrated in Figure 1.27. By comparing the torque performance of the studied machine for both conventional and optimized cases (Figure 1.32), it can be clearly deduced that employing the "optimal" multilayer configuration (Figure 1.30-(d)) yields to almost cancelling the torque ripple.

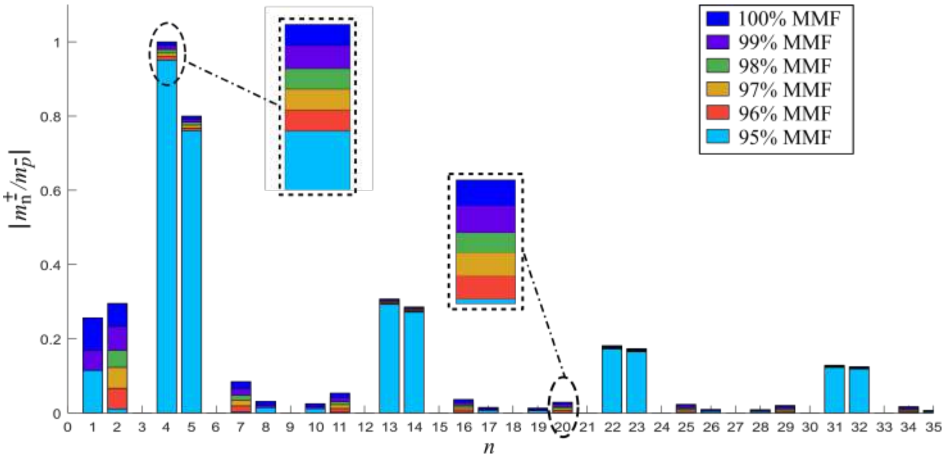

Figure 1.28: Superposition of harmonic spectra corresponding to different design configurations explored throughout the optimization for torque ripple reduction of the 9-slot/8-pole machine configuration.

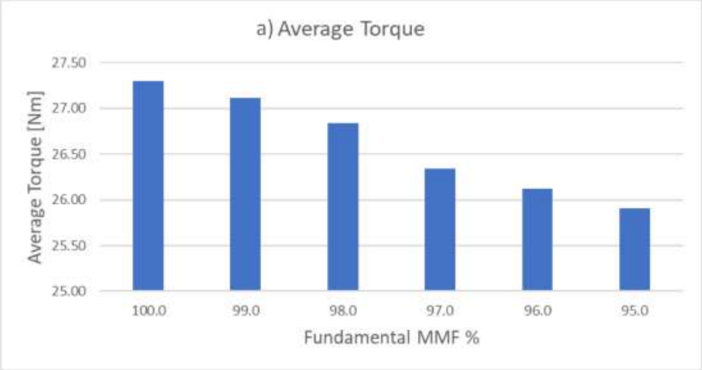

Figure 1.29: Average torque corresponding to different winding design solutions of the optimization.

1.5.4 Magnet eddy current losses minimisation

1.5.4.1 Rotor losses in FSCW SPM machines: brief review

Permanent-magnet losses minimization is one of the most common targets in the optimized design of PM machines with FSCWs. Potentially dangerous eddy currents, chich act as a possible cause for overheating and demagnetization, are mainly produced in permanent magnets by sub-harmonics [50, 51]. Among the several models proposed for the study of rotor losses, the analytical models are preferred to FEA models, which are very time consuming. Analytical methods have been proposed in the literature for computing PM losses in FSCW PM machines where the model of the machine is generally simplified where the rotor is formed by layers of homogeneous materials [52–54]. In spite of the simplicity of the geometry, the analytical models provide a favorable comparison among different solutions. In fact, a rapid estimation of the rotor losses is a key issue in any process design since it allows to decide for the viability of of the studied machine design as well as settling for a better choice of slots/ poles combination.

a) Conventional winding matrix

Phases	Tooth index k: 0	1	2	3	4	5	6	7	8
a	100	−100	0	0	0	0	0	0	−100
b	0	0	−100	100	−100	0	0	0	0
c	0	0	0	0	0	−100	100	−100	0

b) Optimized winding matrix

Phases	Tooth index k: 0	1	2	3	4	5	6	7	8
a	41	0	0	0	0	41	−59	100	−59
b	−59	100	−59	41	0	0	0	0	41
c	0	0	41	−59	100	−59	41	0	0

c) Conventional 9-slot/8-pole winding layout

d) Optimized 9-slot/8-pole winding layout

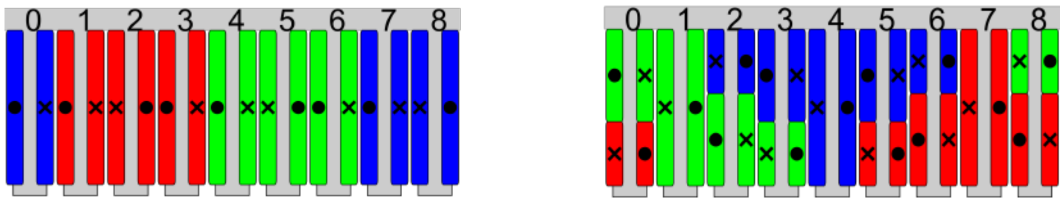

Figure 1.30: Winding matrices and winding layouts of both conventional and optimized 9-slot/8-pole FSCW SPM machine configuration; **(a)** Conventional winding matrix, **(b)** Optimized winding matrix (95% Fundamental MMF), **(c)** conventional winding layout corresponding to the winding matrix presented in **(a)**, and **(d)** optimized winding layout corresponding to the winding matrix presented in **(b)**.

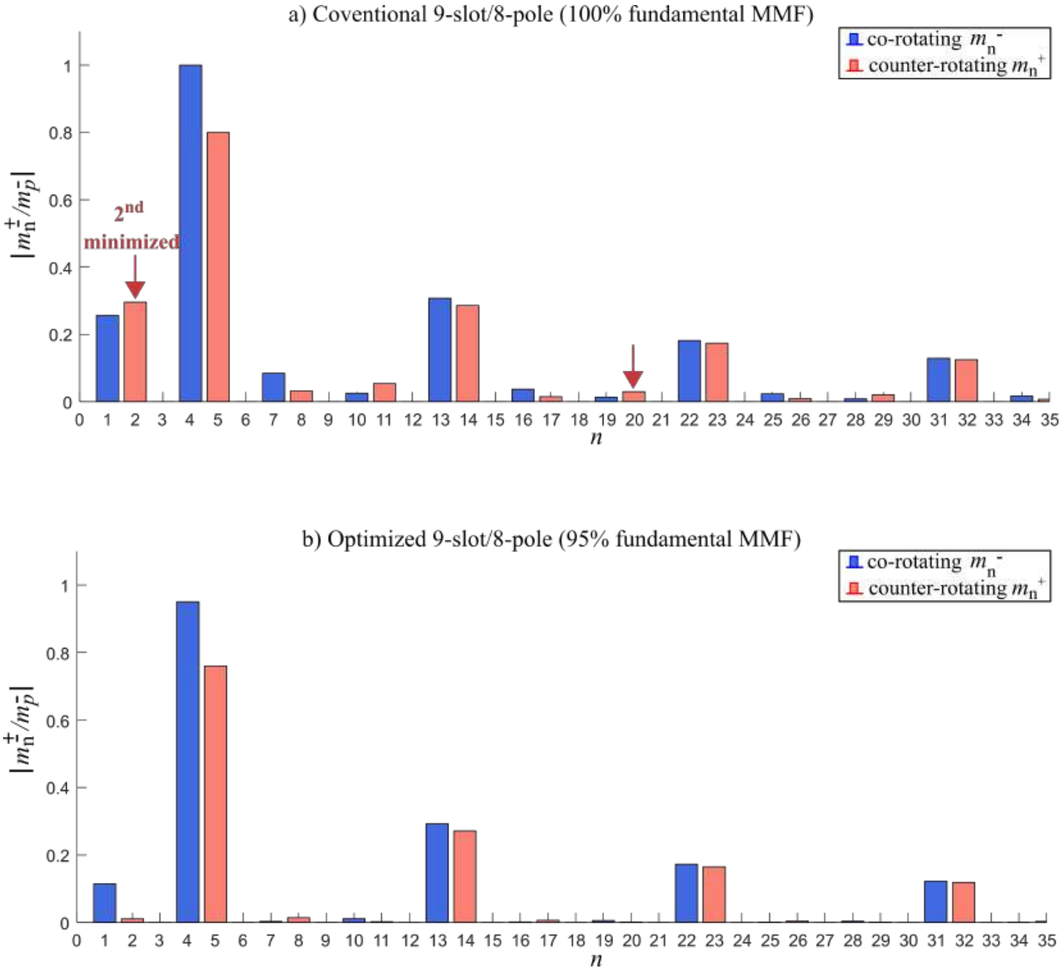

Figure 1.31: MMF space harmonic spectra of the 9-slot/8pole FSCW machine configuration: **a)** conventional star of slot winding machine, **b)** optimized winding machine corresponding to 95% of MMF fundamental.

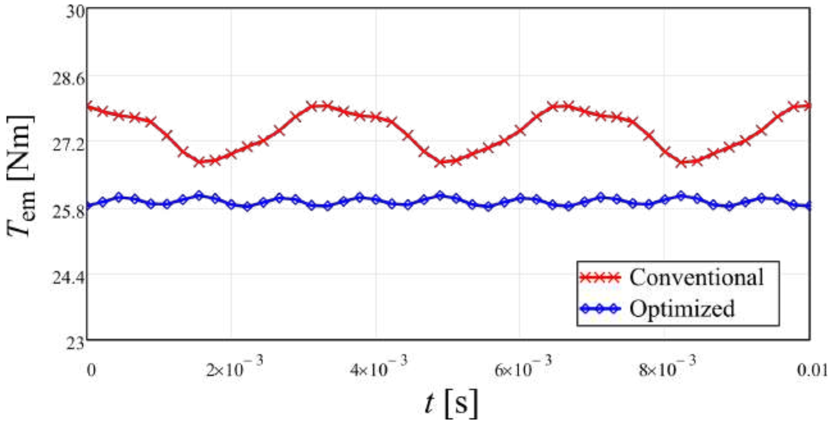

Figure 1.32: Comparison of the 9-slot/8-pole FSCW machine configuration torque waveforms of the conventional winding configuration (100 % fundamental MMF) and the "optimal" one (95% fundamental MMF).

More specifically, the problem has been often addressed through conformal mapping transformation leading to a linear geometry for the air-gap [53, 54]. However, the use of conformal transformations for energy or loss computation may introduce some inaccuracies [55]. For this reason, a simple annular air-gap model is proposed in [20] to be used for the formulation on an analytical expression for PM eddy-current losses estimation. Actually, it is important to have a fast but accurate formula that expresses the eddy-current losses produced in the magnets by each of the stator MMF space harmonic. This is particularly useful to be implemented into the quadratic optimization algorithm as it can allow a direct action on each single space harmonic to limit its parasitic effect.

In what follows, the analytical model to compute rotor losses under the effect of stator space harmonics is described and its application on different slot/ pole configurations is be performed. Then, an application of the quadratic programming with the aim of minimizing the magnet eddy-current losses is executed and results is validated with FEA simulations.

1.5.4.2 Analytical model for magnet losses computation

In this part, an analytical formulation to evaluate the magnet losses taking into account the stator space harmonics is developed. To simplify the process, the following assumptions are adopted as it is shown in Figure 1.33:

- the rotor magnets are modeled as a continuous annulus with a magnetic permeability μ_m and electric conductivity σ_m,
- the stator slotting effect is neglected,
- stator and rotor cores are assumed infinitely permeable,
- a rotor attached polar reference frame characterized by coordinates (r, θ_r) is introduced.

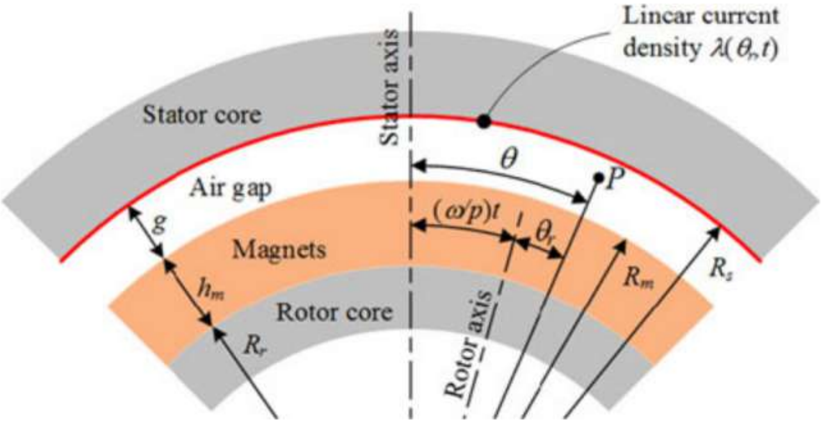

Figure 1.33: Simplified model for the analysis of magnet eddy-current losses due to air-gap MMF harmonics.

The angular position θ of a generic point P in the stator reference frame is written with respect to the rotor reference frame such that:

$$\theta = \theta_r + \frac{\omega}{p}t \tag{1.84}$$

By substituting (1.84) in (1.18), the expression of the stator MMF in the rotor reference frame can be rewritten as follows:

$$M_s(\theta_r + \frac{\omega}{p}t, t) = Re\left\{\sum_{n=1..\infty}\left[m_n^- e^{i(\omega(1-\frac{n}{p})t-n\theta_r)} + m_n^+ e^{i(\omega(1+\frac{n}{p})t+n\theta_r)}\right]\right\} \tag{1.85}$$

Since slotting effect is not considered, the stator MMF is represented by an equivalent linear current distribution $\lambda(\theta_r, t)$ spread around the stator bore as shown in Figure 1.33, such that [23]:

$$\lambda(\theta_r, t) = \frac{1}{R_s}\frac{\partial}{\partial\theta_r}M_s\left(\theta_r + \frac{\omega}{p}t, t\right) \tag{1.86}$$

This naturally imposes a tangential component of the air-gap magnetic field at $r = R_s$ given by:

$$\begin{aligned} H_\theta(\theta_r, t)|_{r=R_s} &= \lambda(\theta_r, t) \\ &= \frac{1}{R_s}Re\left\{\sum_{n=1..\infty}\left[-nm_n^- e^{i(\omega(1-\frac{n}{p})t-n\theta_r)} + nm_n^+ e^{i(\omega(1+\frac{n}{p})t+n\theta_r)}\right]\right\} \end{aligned} \tag{1.87}$$

Such magnetic field can be expressed by the following compact complex phasors function of θ_r as:

$$H_\theta(\theta_r)|_{r=R_s} = \pm\frac{1}{R_s}Re\sum_{n=1..\infty} nm_n^\pm e^{\pm in\theta_r} \tag{1.88}$$

associated to the rotor frequency:

$$\omega_n^\pm = \omega(1 \pm \frac{n}{p}) \tag{1.89}$$

In order to have a generic analytical formulation which takes into account every harmonic order n associated to the rotor frequency $\omega_n^{\pm}$, two complex vector potentials $U_n^{\pm}$ and $V_n^{\pm}$ produced respectively in the air-gap and the PM regions. These two vector potentials obey to the following Laplace's and Helmholtz's differential equations [56]:

$$\frac{\partial^2 U_n^{\pm}}{\partial r^2} + \frac{1}{r}\frac{\partial U_n^{\pm}}{\partial r} + \frac{1}{r^2}\frac{\partial^2 U_n^{\pm}}{\partial \theta_r^2} = 0, R_m \leq r \leq R_s \tag{1.90}$$

$$\frac{\partial^2 V_n^{\pm}}{\partial r^2} + \frac{1}{r}\frac{\partial V_n^{\pm}}{\partial r} + \frac{1}{r^2}\frac{\partial^2 V_n^{\pm}}{\partial \theta_r^2} = i\omega_n^{\pm}\mu_m\sigma_m V_n^{\pm}, R_r \leq r \leq R_m \tag{1.91}$$

where R_r and R_m and R_s are the radii shown in Figure 1.33. Using the method of separation of variables, the general solutions for (1.90) and (1.91) can be expressed in the from below [56]:

$$U_n^{\pm}(r,\theta_r) = (A_n^{\pm} r^n + B_n^{-n})e^{\pm in\theta_r} \tag{1.92}$$

$$V_n^{\pm}(r,\theta_r) = (C_n^{\pm} J_n(\kappa_n^{\pm} r^n) + D_n^{\pm} Y_n(\kappa_n^{\pm} r^n))e^{\pm in\theta_r} \tag{1.93}$$

where J_n and Y_n are the n^{th}-order Bessel functions of the first and second kind; $A_n^{\pm}$, $B_n^{\pm}$, $C_n^{\pm}$ and $D_n^{\pm}$ are complex coefficients depending on the boundary conditions; $\kappa_n^{\pm}$ is a complex coefficient such that $(\kappa_n^{\pm})^2 = -i\sigma_m\mu_0\omega_n^{\pm}$.

Thanks to the relationship between the flux density and the magnetic vector potential and by applying the appropriate boundary conditions, the following relationships can be established:

$$-\frac{1}{\mu_0}\left.\frac{\partial U_n^{\pm}}{\partial r}\right|_{r=Rs} = \pm\frac{1}{R_s} n m_n^{\pm} e^{\pm in\theta_r} \tag{1.94}$$

$$\left.\frac{\partial U_n^{\pm}}{\partial \theta_r}\right|_{r=Rm} = \left.\frac{\partial V_n^{\pm}}{\partial \theta_r}\right|_{r=R_m}, \quad \left.\frac{\partial U_n^{\pm}}{\partial r}\right|_{r=Rm} = \left.\frac{\partial V_n^{\pm}}{\partial r}\right|_{r=R_m} \tag{1.95}$$

$$\left.\frac{\partial V_n^{\pm}}{\partial r}\right|_{r=R_r} = 0 \tag{1.96}$$

where (1.94) imposes the magnetic field tangential component along the stator bore $r = R_s$ to be equal to the one given by (1.88); (1.95) imposes the continuity of the field radial and tangential components across the boundary $(r = R_m)$ between the air-gap and the magnet regions; (1.96) interprets that the field is purely radial on the rotor bore $(r = R_r)$ given the assumption of infinite permeability of the rotor core. By substituting (1.92) and (1.93) in (1.94)-(1.95), a linear set of equations is obtained from which the coefficients $C_n^{\pm}$ and $D_n^{\pm}$ are determined as follows:

$$C_n^{\pm} = -\frac{2i\mu_0 n\phi_n^{\pm} m_n^{\pm}}{\Delta_n^{\pm} R_s R_m^2} \tag{1.97}$$

$$D_n^{\pm} = \frac{2i\mu_0 n \epsilon_n^{\pm} m_n^{\pm}}{\Delta_n^{\pm} R_s R_m^2} \tag{1.98}$$

where $\epsilon_n^{\pm}$, $\phi_n^{\pm}$ and $\Delta_n^{\pm}$ are defined by:

$$\begin{aligned} \Delta_n^{\pm} =& (\beta_n^{\pm}\epsilon_n^{\pm} - \alpha_n^{\pm}\phi_n^{\pm} - i\delta_n^{\pm}\epsilon_n^{\pm} + i\chi_n^{\pm}\phi_n^{\pm}) R_s^{n-1} R_m^{-n-1} \\ &+ (\alpha_n^{\pm}\phi_n^{\pm} - \beta_n^{\pm}\epsilon_n^{\pm} - i\delta_n^{\pm}\epsilon_n^{\pm} + i\chi_n^{\pm}\phi_n^{\pm}) R_m^{n-1} R_s^{-n-1} \end{aligned} \tag{1.99}$$

$$\alpha_n^{\pm} = inJ_n(\kappa_n^{\pm} R_m) R_m^{-1} \tag{1.100}$$

$$\beta_n^{\pm} = -inY_n(\kappa_n^{\pm} R_m) R_m^{-1} \tag{1.101}$$

$$\chi_n^{\pm} = -\kappa_n^{\pm} J_{n+1}(\kappa_n^{\pm} R_m) + nR_m^{-1} J_n(\kappa_n^{\pm} R_m) \tag{1.102}$$

$$\delta_n^{\pm} = -\kappa_n^{\pm} Y_{n+1}(\kappa_n^{\pm} R_m) + nR_m^{-1} Y_n(\kappa_n^{\pm} R_m) \tag{1.103}$$

$$\delta_n^{\pm} = \kappa_n^{\pm} J_{n+1}(\kappa_n^{\pm} R_r) - nR_r^{-1} J_n(\kappa_n^{\pm} R_r) \tag{1.104}$$

$$\delta_n^{\pm} = \kappa_n^{\pm} Y_{n+1}(\kappa_n^{\pm} R_r) - nR_r^{-1} Y_n(\kappa_n^{\pm} R_r) \tag{1.105}$$

Once the vector potential (1.93) in the magnet region is evaluated, the eddy-current density phasor $j_n^{\pm}$ in the magnets due to the n^{th} harmonic order can be expressed as [56]:

$$j_n^{\pm}(r, \theta_r) = -i\omega_n^{\pm} \sigma V_n^{\pm}(r, \theta_r) \tag{1.106}$$

The eddy-current losses $P_n^{\pm}$ in the magnet region due to the n^{th} order of harmonic will then be:

$$\begin{aligned} P_n^{\pm} &= \frac{L}{2\sigma} \int_0^{2\pi} \int_{R_r}^{R_m} \left| j_n^{\pm}(r, \theta_r) \right|^2 r dr d\theta \\ &= \pi L \omega_n^{\pm 2} \sigma \int_{R_r}^{R_m} \left| C_n^{\pm} J_n(\kappa_n^{\pm} r^n) + D_n^{\pm} Y_n(\kappa_n^{\pm} r^n) \right|^2 r dr \end{aligned} \tag{1.107}$$

By substituting (1.97) and (1.98) in (1.107), the following expression can be obtained:

$$\begin{aligned} P_n^{\pm} &= \frac{4\pi\mu_0^2 n^2 L \omega_n^{\pm 2} \sigma_m}{R_m^4 R_s^2 |\Delta_n^{\pm}|^2} |m_n^{\pm}|^2 \int_{R_r}^{R_m} \left| \epsilon_n^{\pm} Y_n(\kappa_n^{\pm} r) - \phi_n^{\pm} J_n(\kappa_n^{\pm} r) \right| r dr \\ &= p_n^{\pm} |m_n^{\pm}|^2 \end{aligned} \tag{1.108}$$

where $p_n^{\pm}$ gives the losses coefficients due to the n^{th} MMF harmonic order associated to the rotor frequency $\omega_n^{\pm}$ and having a unit magnitude such as:

$$p_n^{\pm} = \frac{4\pi\mu_0^2 n^2 L \omega_n^{\pm 2} \sigma_m}{R_m^4 R_s^2 |\Delta_n^{\pm}|^2} \int_{R_r}^{R_m} \left| \epsilon_n^{\pm} Y_n(\kappa_n^{\pm} r) - \phi_n^{\pm} J_n(\kappa_n^{\pm} r) \right| r dr \tag{1.109}$$

The losses coefficients $p_n^{\pm}$, computed trough (1.109), are presented in Figure 1.34 for each harmonic order. Thanks to the superposition principle [57], the losses caused by different MMF harmonics can be summed up to determine the total losses P_{loss} which can be expressed as:

$$P_{loss} = \sum_{n=1..\infty} \left(P_n^+ + P_n^-\right) = \sum_{n=1..\infty} \left(p_n^+ |m_n^+|^2 + p_n^- |m_n^-|^2\right) \tag{1.110}$$

In order to be implemented in the optimization algorithm, it is convenient to express (1.110) in a quadratic form. Using (1.27) the total losses in the magnets can be written as:

$$\begin{aligned} P_{loss} &= \sum_{n=1..\infty} \left(p_n^+ \mathbf{x}^T \mathbf{Q}_n^+ \mathbf{x} + p_n^- \mathbf{x}^T \mathbf{Q}_n^- \mathbf{x}\right) \\ &= \mathbf{x}^T \left[\sum_{n=1..\infty} \left(p_n^+ \mathbf{Q}_n^+ + p_n^- \mathbf{Q}_n^-\right)\right] \mathbf{x} \end{aligned} \tag{1.111}$$

The total magnet losses are thus expressed in a quadratic form function of the turn vector $\mathbf{x}$. At this point of treatment, the equation to define the objective function is set. What remains is the proper implementation of the optimization problem following (1.59).

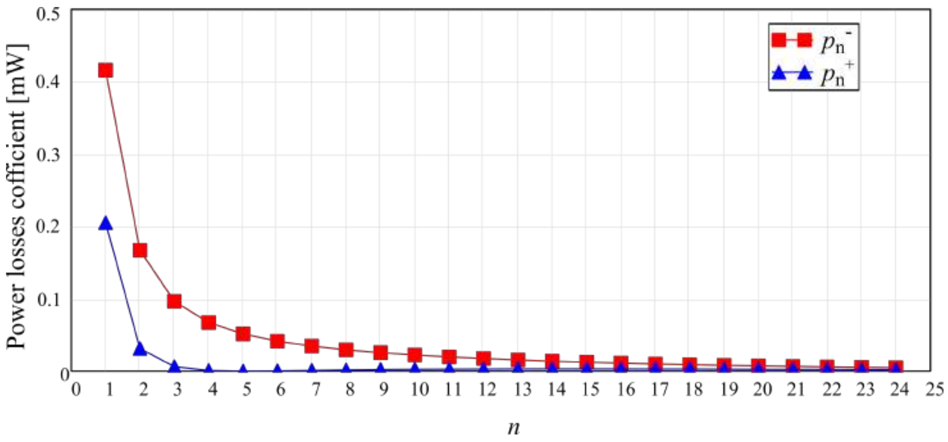

Figure 1.34: Magnet losses coefficients of the MMF harmonics computed by (1.109).

1.5.4.3 Identification of optimizable FSCW configurations

To investigate on how the magnets eddy current losses vary with the different slot/ pole combinations, an homogeneous comparison is needed between reasonably designed machines. For this purpose, the SPM machine model presented in subsection 1.5.1 is considered for the different number of slots Z and pole pair p. By selecting machine parameters as indicated in subsection 1.5.1, the current density is maintained invariable as well as the air-gap field due to PMs and armature reaction. Given the availability of the analytical equation (1.110), a straightforward evaluation of the magnets losses can be performed without referring to FEA simulations. In fact this method was validated by time harmonic FEA simulations in [20] and by time stepping FEA simulations in [39] showing good accordance. Analytical results of magnet eddy-current losses for various slot/ pole combinations are reported in Table 1.8 in terms of mW per magnet millimeter cube. Similarly to what was done for the UMP and torque ripple application cases, it is it crucial to investigate on the feasibility of the considered optimization on the several machines configurations. Taking into account the type of the considered algorithm which is a harmonic-based optimization, the interconnection between stator MMF space harmonic orders of each machine has to be studied. Based on (1.68), "optimizable" configurations characterized by MMF stator harmonics independent from the fundamental are identified and highlighted in Table 1.8. Doing so, the range of machine configurations suitable for the optimization is limited.

Table 1.8: Magnet specific losses in [mW/mm^3] for various Z slots/ $2p$ poles combinations. highlighted cells refer to "optimizable" configurations.

Number of slots Z	Number of poles $2p$											
	2	4	6	8	10	12	14	16	18	20	22	24
3	0.185	7.828										
6		0.177	\	7.758								
9			0.171	0.817	2.220	7.670						
12				0.165	0.604	\	2.920	7.570				
15					0.160	X	0.862	1.659	X	7.466		
18						0.156	0.420	0.773	\	2.106	3.803	7.369
21							0.153	0.414	X	0.885	1.435	X
24								0.151	X	0.575	0.73	\
27									0.148	0.327	0.476	0.752

It is to be noted that "optimizable" configurations may still present harmonics that can produce losses but cannot be reduced due to their dependence on the fundamental harmonic. As can be seen in the example spectrum of the 9-slot/8-pole configuration illustrated in Figure 1.35, the highlighted harmonic orders obeying to the relation 1.68 such that $p - nZ = -5, -23, -41...$ and $p + nZ = 13, 31, 49...$ have significant amplitude but cannot be reduced. However, previous works have proved that harmonics contribute differently in generating rotor losses and major part of magnet losses are found to be caused by subharmonics [50, 51]. For this reason, focusing on the reduction or cancellation of subharmonics can be more beneficial in terms of rotor losses reduction. In fact, for the case of the 9-slot/8-pole configuration shown in Figure 1.35, subharmonics are independent from the fundamental which is beneficial for the optimization process. Each color refers to a group of harmonics which are linked to each other by the relation 1.68. This interdependence certainly helps in ameliorating the efficiency of the optimization method.
It emerges from the previously explained investigation that not all FSCW configurations are suitable to be optimized. However, referring to Table 1.8, it seems that the highlighted slot/pole configurations are the most susceptible to generate eddy-current losses which makes the optimization useful to mitigate the impact of this issue.

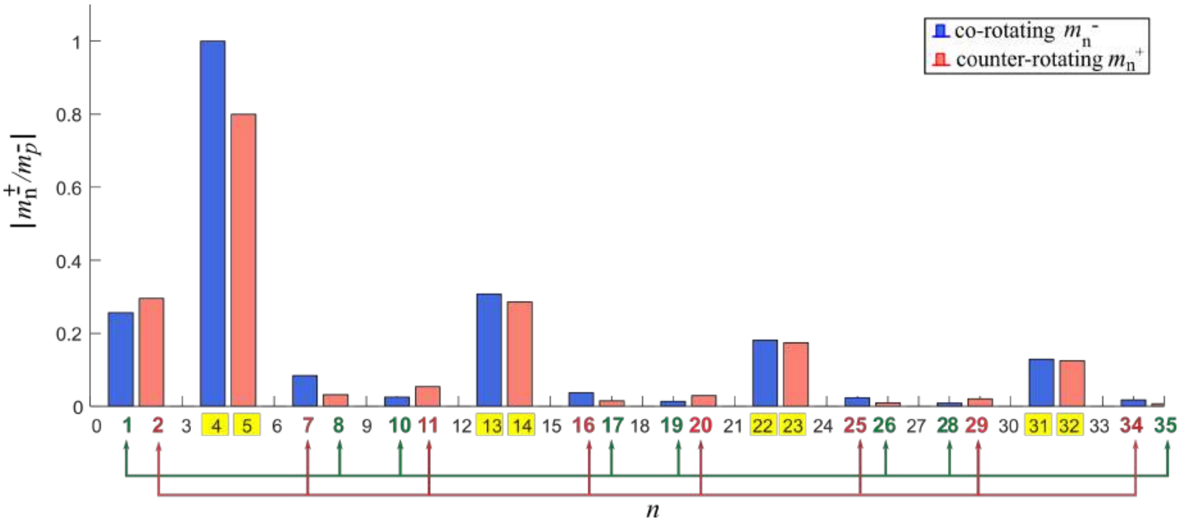

Figure 1.35: stator MMF space harmonic spectrum of the 9-slot/ 8-pole configuration; red and green lines illustrates examples of the different interconnection between harmonics, harmonic orders linked to the fundamental are highlighted in yellow.

1.5.4.4 Application example of the quadratic programming

To assess the applicability of the proposed optimization technique, the quadratic programming algorithm is solved for different FSCW SPM machine configurations highlighted in Table 1.8. To do so, the optimization problem is formulated following the form reported in (1.59) with introducing the objective function aiming to minimize the rotor losses due to MMF space harmonics as:

$$f_{loss}(\mathbf{x}) = \mathbf{x}^T \left[\sum_{n=1..\infty} \left(p_n^+ \mathbf{Q}_n^+ + p_n^- \mathbf{Q}_n^- \right) \right] \mathbf{x} \tag{1.112}$$

For each machine configuration, the resolution of the optimization problem is executed while decreasing the fundamental MMF by 1% for each optimization iteration. The magnet losses are calculated analytically for each "optimal" solution corresponding to each fundamental MMF decrease ranging from 100% (corresponding to the star of slot configuration) down to 90% fundamental MMF. A common practice to decrease the rotor losses caused by the armature MMF harmonic content is to decrease the current. In order to highlight the effect of the optimization procedure on the rotor losses, the trend representing the eddy-current magnet losses under the effect of current decrease (leading to a proportional MMF decrease) and keeping the conventional winding layout unchanged is presented in Figure 1.36 along with the optimization results (normalized). Through this comparison it can be seen from the gap between both curves that the "optimal" solutions of the proposed optimization lead to considerable decrease in the losses ranging from 23% to 58% even under a slight percentage of fundamental MMF reduction (less than 6%).

For the sake of clarity, optimisation results of the 12-slot/ 10-pole machine configuration chosen as an application example of the quadratic optimization algorithm characterized by the data listed in Table 1.9 are illustrated in what follows. As explained previously, the quadratic programming is

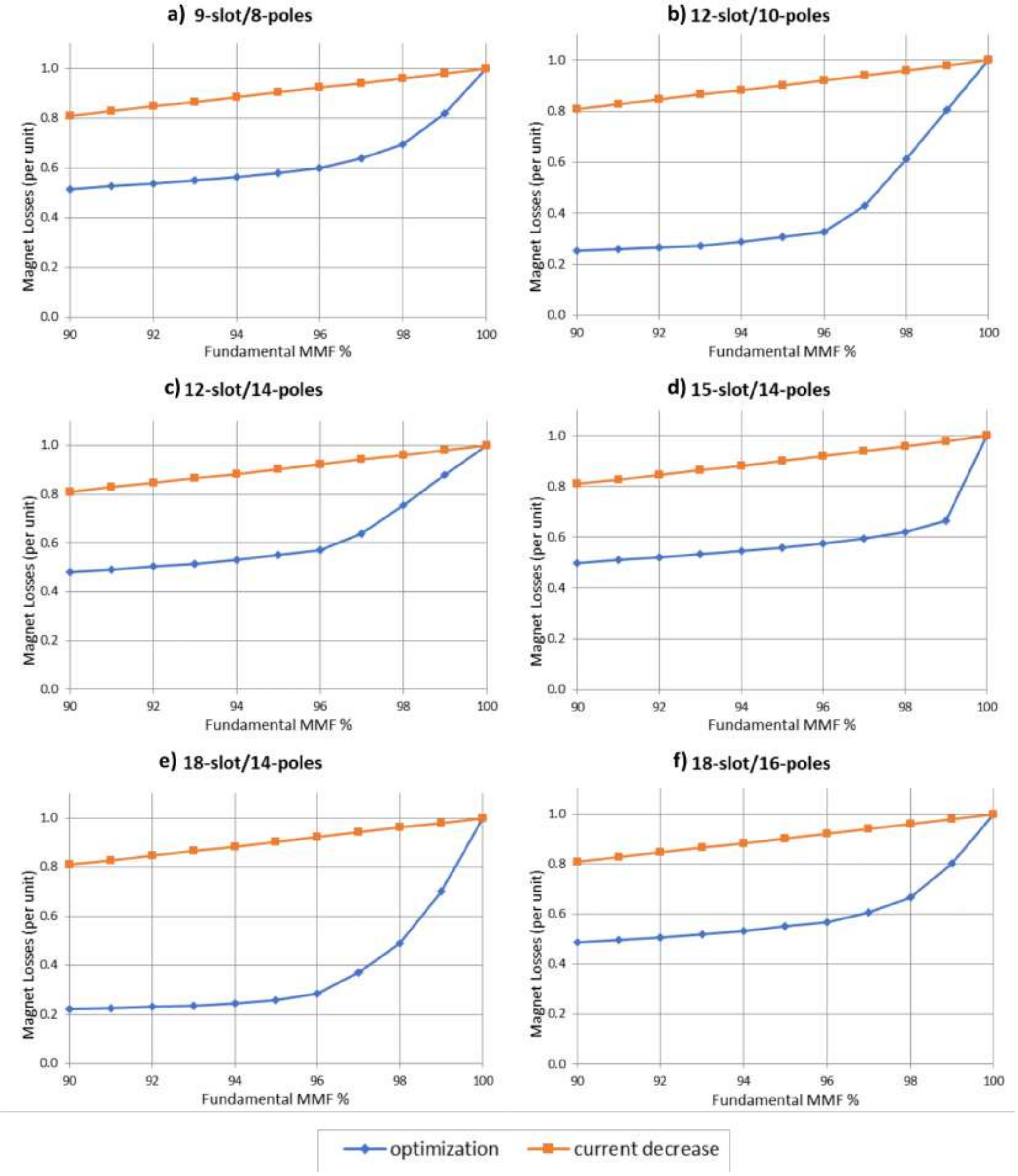

Figure 1.36: Pareto fronts resulting from the quadratic optimization subject to eddy-current losses minimization applied on different FSCW machine configurations. In the same graphs are presented the trends of magnet losses under the effect of stator current decrease with keeping unchanged the conventional stator of slot winding layout.

Table 1.9: Characteristic data of the example 12-slot/10-pole FSCW machine

Z	Number of slots	12	N_0	Maximum number of turns per coil	100
p	Number of pole pair	5	I_0	Peak value of stator current	6 A
R_s	Stator bore radius	55 mm	f	Stator frequency	50Hz
h_m	PM height	4 mm	μ_0	Magnet permeability	$4\pi 10^{-7}$ H/m
g	Air gap width	3 mm	σ_m	Magnet electrical conductivity	0.667 MS/m
L	Core length	100 mm	c_m	Magnet to pole span ratio	0.95
H_c	Magnet coercivity	850 A/mm	k_f	slot fill factor	0.5

solved for different fundamental MMF reduction percentages (100%, 99%, 98%,..90%) to obtain the corresponding multilayer winding layouts designated as #1, #2, #3...#11 respectively. Figure 1.37 represents the Pareto front of the magnet losses resultant from the optimization process. For more clarity, only results issued from the first nine winding layout solutions are presented. The optimization output winding matrices corresponding to the first nine winding layout solutions are summarized in Table 1.10 in terms of number of turns per phase wound around each stator tooth. Table 1.11 summarizes the number of layers and the number of different coil sizes of the different winding designs solution of the optimization. Looking at Figure 1.37 it appears that magnet losses reduction is achieved, at the expense of a lowered MMF fundamental paying the toll of increasing winding complexity. Indeed, from the results it emerges that the number of layers ranges from 2 to 4 for the first eight winding layouts whilst starting from the design #9 the winding layout gets more complex and the number of layers can reach 6. Despite its effectiveness, such a complex solution is better to be avoided as it is not practical from the manufacturing point of view especially when it is possible to get similar results by employing simpler winding designs. In fact, it can be seen from the Pareto front that from 96% fundamental MMF (design #5) to 90% (design #11) , the drop in the generated magnet losses resultant from optimal winding solution deviates and tends do follows a low slope. The effectiveness of the optimization within this range is no more significant and the complex winding layout solutions (with a number of layers grater than 4) can be avoided. For illustrative purposes, The FSCW arrangements of the optimal solutions are presented in Figure 1.37. The characteristic number of turns n', n'' and n''' for the various unequal coils are detailed in Table 1.10 for the eight first designs. The characteristic sizes for the various unequal coils are detailed in Table 1.12.

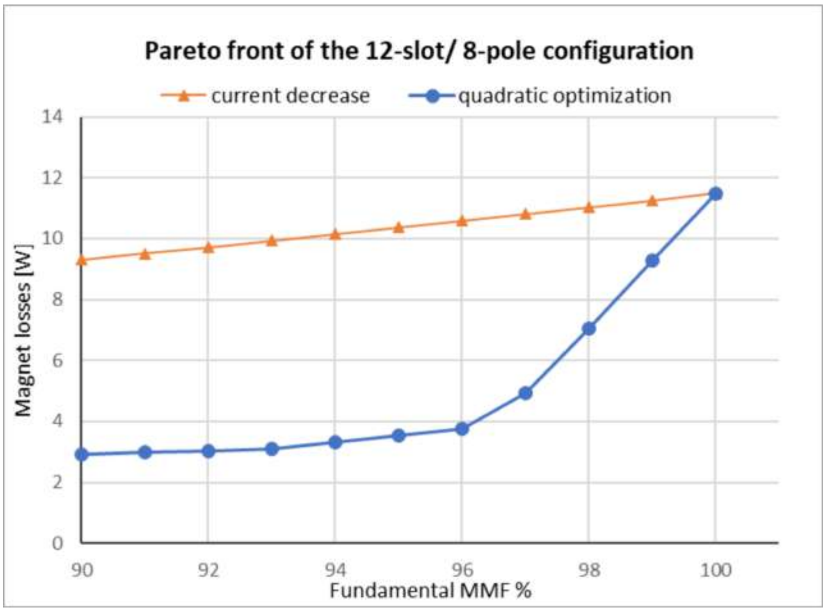

Figure 1.37: Quadratic optimization Pareto front of the 12-slot/10-pole FSCW machine configuration subject to eddy-current losses minimization.

Table 1.10: Winding matrices of the nine first winding layouts resultant from the quadratic optimization.

			Tooth index k											
			0	1	2	3	4	5	6	7	8	9	10	11
Design #1	Phases	*a*	0	100	−100	0	0	0	0	−100	100	0	0	0
		b	0	0	0	−100	100	0	0	0	0	100	−100	0
		c	100	0	0	0	0	100	−100	0	0	0	0	−100
Design #2	Phases	*a*	7	0	0	1	−93	99	−7	0	0	−1	93	−99
		b	−93	99	−7	0	0	−1	93	−99	7	0	0	1
		c	0	−1	93	−99	7	0	0	1	−93	99	−7	0
Design #3	Phases	*a*	−17	0	0	0	83	−100	17	0	0	0	−83	100
		b	83	−100	17	0	0	0	−83	100	−17	0	0	0
		c	0	0	−83	100	−17	0	0	0	83	−100	17	0
Design #4	Phases	*a*	0	0	0	31	−100	69	0	0	0	−31	100	−69
		b	−100	69	0	0	0	−31	100	−69	0	0	0	31
		c	0	−31	100	−69	0	0	0	31	−100	69	0	0
Design #5	Phases	*a*	−48	98	−52	2	0	0	48	−98	52	−2	0	0
		b	0	0	48	−98	52	−2	0	0	−48	98	−52	2
		c	52	−2	0	0	−48	98	−52	2	0	0	48	−98
Design #6	Phases	*a*	−7	0	0	−43	93	−57	7	0	0	43	−93	57
		b	93	−57	7	0	0	43	−93	57	−7	0	0	−43
		c	0	43	−93	57	−7	0	0	−43	93	−57	7	0
Design #7	Phases	*a*	36	0	0	14	−64	86	−36	0	0	−14	64	−86
		b	−64	86	−36	0	0	−14	64	−86	36	0	0	14
		c	0	−14	64	−86	36	0	0	14	−64	86	−36	0
Design #8	Phases	*a*	26	0	0	26	−74	74	−26	0	0	−26	74	−74
		b	−74	74	−26	0	0	−26	74	−74	26	0	0	26
		c	0	−26	74	−74	26	0	0	26	−74	74	−26	0
Design #9	Phases	*a*	27	−2	0	28	−71	73	−28	0	2	−27	73	−71
		b	−73	70	−27	1	1	−27	70	−73	27	−1	−1	27
		c	0	−28	73	−71	28	0	−2	27	−71	73	−27	2

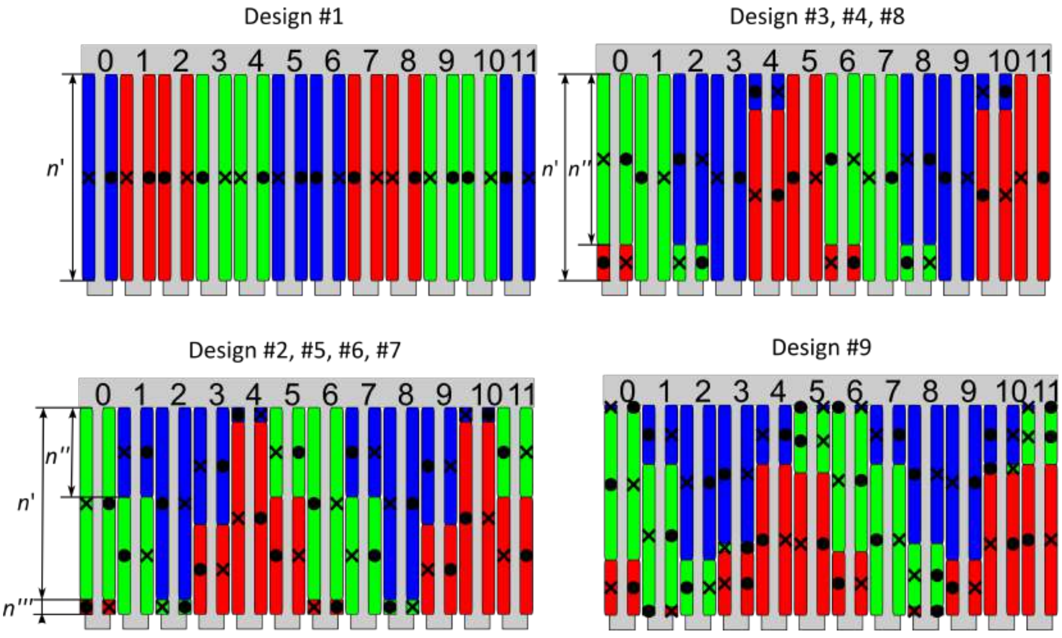

Figure 1.38: FSCW design configurations resulting from the quadratic optimizations. Colors indicate different phases; symbols "•" and "×" indicate current conventional directions.

As a results of the optimization approach herein adopted, it is observed that, even if every

Table 1.11: Number of layers and number of different coil sizes for the different winding layout solutions.

	Design #								
	#1	#2	#3	#4	#5	#6	#7	#8	#9
Number of layers	2	4	2 to 3	2 to 3	4	4	4	4	4 to 6
Number of different coil sizes	1	4	3	3	4	4	4	2	6

Table 1.12: Characteristic number of turns for the tooth coils corresponding to each optimization winding layout solution.

	Design #							
	#1	#2	#3	#4	#5	#6	#7	#8
n'/N_0	1	0.99	1	1	0.98	0.93	0.86	0.74
n''/N_0	-	0.93	0.83	0.69	0.52	0.57	0.64	0.26
n'''/N_0	-	0.01	-	-	0.2	0.07	0.14	-

winding layout design is considered as a local "optimal" solution for the considered fundamental decrease, a global "optimal" can be obtained in terms of rotor losses minimization point of view under the effect of fundamental MMF decrease to a certain point. In fact, it can be seen that the structure of designs #2, #3, #4 cannot be identified as "optimal" as it can be further enhanced using the designs #5, #6, #7 and #8 characterized by four layers per slot where two coils of different phases with unequal size are wound around each tooth as shown in Tables 1.10, 1.11 and 1.12.. Conversely, decreasing the fundamental MMF down from 92% (design #9) increases the complexity of the winding layout solutions resulting in more than four layers per slot as reported in Tables 1.10 and 1.11. In fact, designs #9, #10 and #11 present slightly less losses than designs #5, #6 and #7 and #8 and yet characterized by a high number of layers per slot as well as a large number of different coil sizes. From that rises the importance of compromising between choosing the best winding design for achieving rotor losses minimization and the feasibility of the winding arrangement.

Finally, a short insight is next provided into the way how the proposed optimization algorithm automatically achieves the optimal solution under any constraint of the fundamental MMF percentage. This can be seen looking at the MMF harmonic content in Figure 1.39 of the eight designs #1, #2,...,#8 obtained from the optimization. In fact, in the attempt to minimize rotor losses, the algorithm acts differently on the various harmonics. For instance, the subharmonic of order 1 is significantly abated for a decreasing fundamental MMF because they are responsible of the major part of magnet losses (p_1^+ in Figure 1.34. Consequently, all the harmonics related to the subharmonic by equation (1.67) (i.e. $-1 + nZ = 11, 23, 35..$ and $-1 - nZ = -13, -25, -37..$) are reduced similarly by the same proportion as can be seen in Figures 1.40-a, c and d. Conversely, the harmonics with orders 7, 17, 19, 29 and 31, although large, are only slightly reduced proportionally to the decrease of the 5^{th} harmonic. This is because all these harmonics are related to the fundamental with the relation (1.67) such that $p + nZ = 17, 29, 41...$ and $p - nZ = -7, -19, -31...$ where $n = 1, 2, 3....$ Nevertheless, while performance of the optimization process on the large harmonics is small, their effect on magnet losses generation compared to the subharmonic is very limited as they are associated to very small loss coefficients (p_7^+, p_{17}^-, p_{19}^+, p_{29}^-, p_{31}^+,...in Figure 1.34). It is also important to observe how the algorithm does not act on a given subharmonic separately.

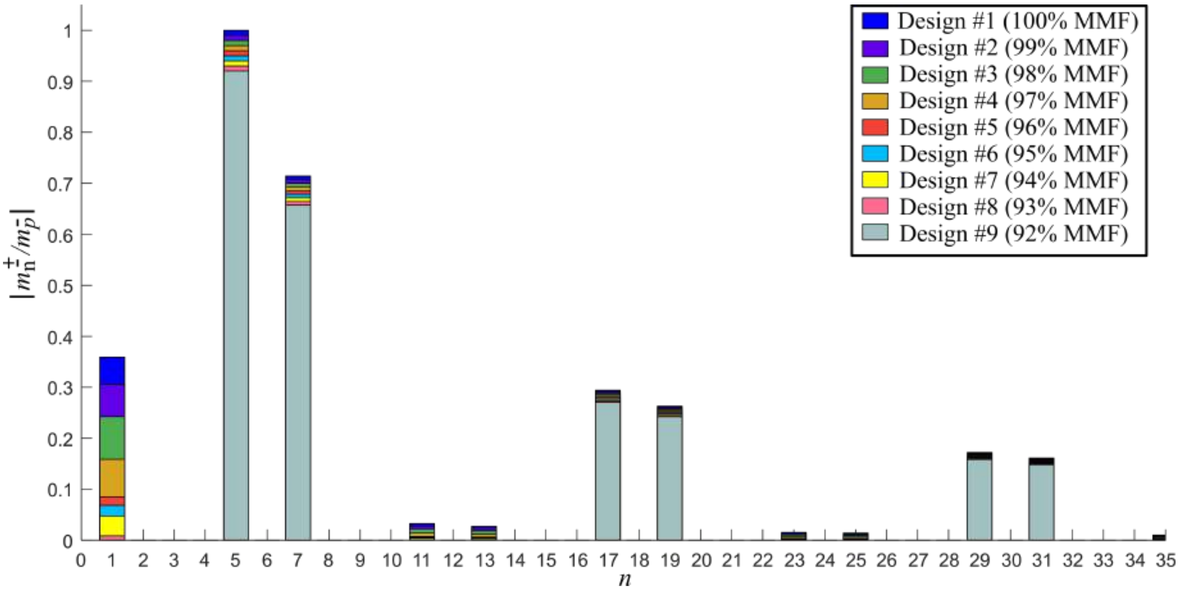

Figure 1.39: Superimposition of different optimization solutions stator MMF harmonic spectra of the 12-slot/10-pole FSCW machine configuration.

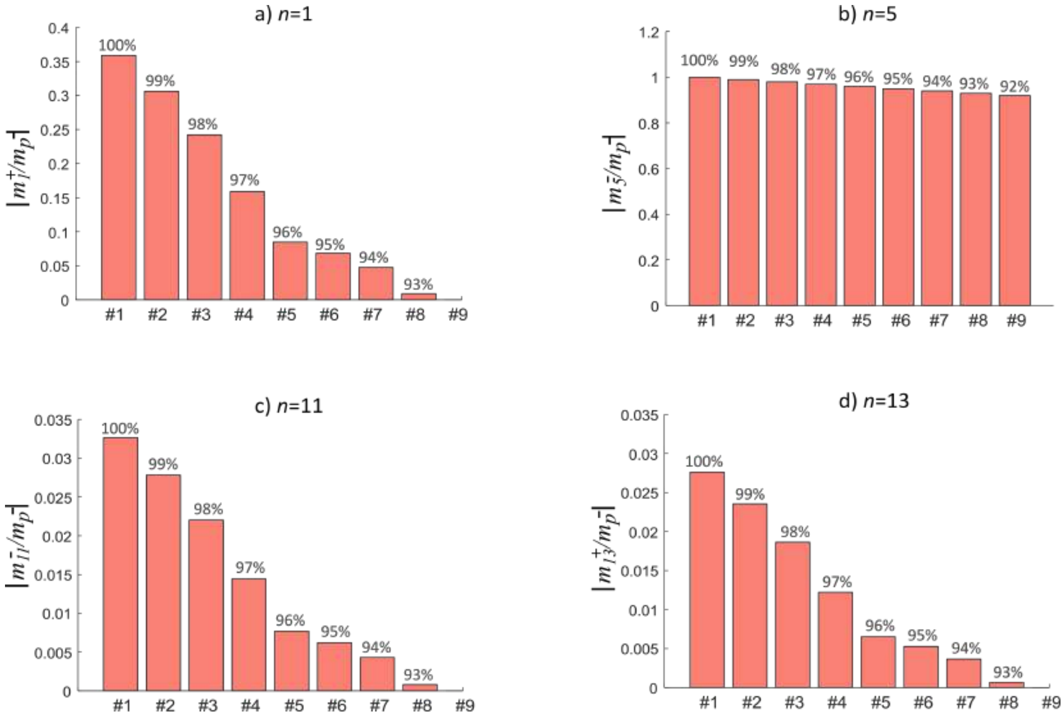

Figure 1.40: Magnitude of the stator MMF space harmonics for the first 9 output solution designs corresponding to: **a)** 1^{st} subharmonic, **b)** the fundamental harmonic, **c)** the 11^{th} harmonic and **d)** the 13^{th} harmonic.

Differently from what is usually done in the literature, the minimization of the rotor losses is the goal instead of the cancellation of the single subharmonic. Indeed, optimal solutions can be found without the cancellation of the first subharmonic. For instance, a significant drop of the magnet losses is observed (Figure 1.37) using designs #5, #6 and #7 even if their first MMF subharmonic is not totally cancelled (Figure 1.40-a). Evidently, the strength of the proposed algorithm is its capability of automatically identifying which harmonics are to be decreased and to what extent in order for the total rotor losses to be reduced.

For a clearer visualisation of the optimization effect on the magnet losses, the 12-slot/10-pole FSCW machine example which characteristics are presented in Table 1.9 is modeled and analysed by time-stepping FEA simulations in order to compute magnet losses at steady state. The optimized winding layout corresponding to design #4 is considered to be compared to the conventional star of slot winding layout (design #1). It can be seen from Figure 1.41 that-as expected-the case of design #4 shows lower amount of losses with respect to the design #1. The maximum current density corresponding to the "hot spots" presented especially on the magnets surface is reduced from 0.676 A/mm^2 for design #1 down to 0.465 A/mm^2 for design #4 i.e. a decrease of approximately 31%.

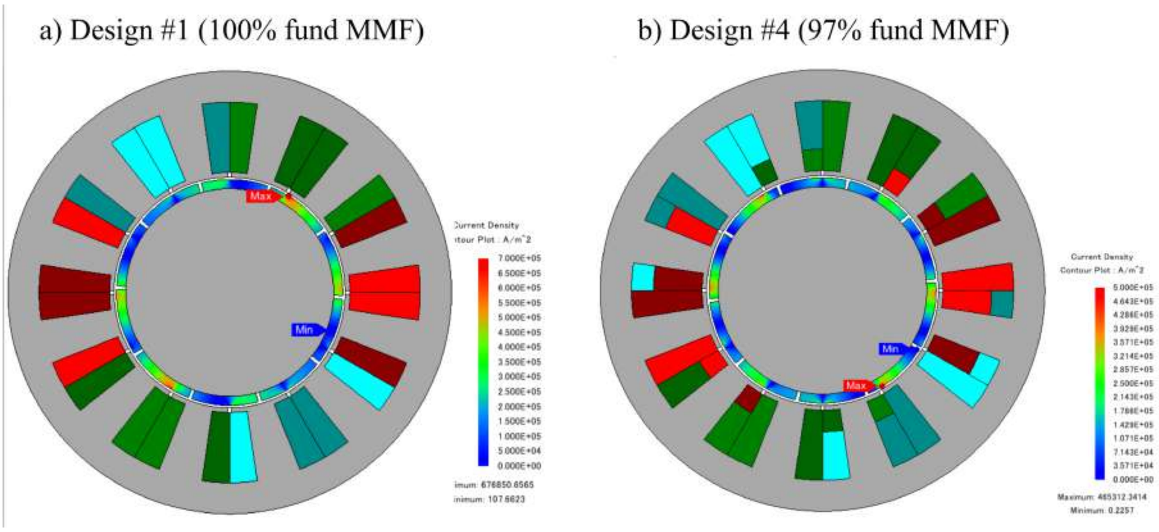

Figure 1.41: Example of the magnet losses computation by time stepping FEA simulations applied on the 12-slot/10-pole machine under study; **a)** corresponds to design #1 (100% fundamental MMF) and **b)** is for design #4 (97% fundamental MMF).

1.5.5 Investigation into the applicability of FSCW to squirrel cage induction motors

1.5.5.1 Introduction

Up to now, three-phase induction machines (IM) commonly use single or double layer, overlapping, distributed windings (DW). This winding configuration leads to more sinusoidal air-gap MMF distribution, hence a good machine performance. In fact, the MMF waveform quality strongly depends on the number of slots per pole per phase q whereby the higher is the q the more sinusoidal is the MMF waveform. It is also demonstrated that the higher the coil pitch, the lower is the parasitic effects and the higher is the efficiency [58]. From that comes the necessity of employing high number of slots to fulfill the winding requirements. Consequently, the complexity of the winding layout and the manufacturing process increases. Large end-winding length results in higher Joule losses, low slot filling factor and packaging problems which are further drawbacks of DW. From the design viewpoint, the use of overlapping windings can be constraining if a high power density is to be achieved which means smaller machine size leading to insufficient space to place a large number of slots. To mitigate this issue, FSCW can be considered as an alternative for high torque density applications offering a simple and fully automatized manufacturing as well as higher fault-tolerant capability and shorter end-windings reducing the weight/torque ratio of the machine[1]. Indeed, while FSCW are commonly used for PM machines, the interest on the application of this type of winding on IMs is growing recently [58–65]. However, the well-known drawback of FSCWs remains in its rich MMF harmonic content which usually limits the winding application to PM machines only. In [58–63] performance of different IMs with squirrel cage in the rotor and FSCW in the stator are studied. Different approaches for the assessment of the IMs behaviour with employing concentrated windings were adopted. For instance, an attempt to evaluate the effect of each MMF harmonic component on the torque using Time Harmonic Finite Element Analysis (THFEA) is proposed in [62]. Another method relying on the analytical winding function theory [58] is used to help in evaluating the induced current in the cage produced by each harmonic. In [63], a study based on the analysis of the coil pitch in IMs is presented to study the influence of such a parameter on the performance of squirrel cage induction machine including FSCW topology. All presented results of these previous works shows that FSCW offer low performance mainly due to the MMF harmonics which cause parasitic torque and high losses as well as high torque ripple and high vibration and acoustic noise.

However, in order to alleviate these unwanted characteristics, some approaches to improve the performance of FSCW IMs have been addressed in the literature [64–67]. For instance, improved winding layout with a dual slot-layer stator characterized by a secondary winding which aims at compensating some of the parasitic harmonic is proposed in [64]. Multilayer windings with a different numbers of turns per coil have been used to minimize the space harmonics magnitudes [65]. In addition to the three-phase solutions, FSCWs multi-phase IMs considerations and trade-offs are studied and presented in [66]. Multi-phase IMs allied with multi-layer winding topologies were also considered as an alternative to ameliorate the quality of the MMF space harmonic spectrum as well as to enhance their fault tolerant capability [67].

While The majority of the aforementioned attempts has focused on suppressing some high order MMF harmonics, no specific study dealing with identifying harmonics contributing the most in performance deterioration is proposed. Referring to the studies existing in the literature, comparisons has been made between the different winding topologies (DW, concentrated windings and FSCW) but an extensive study on the different FSCW configurations applied to squirrel cage IMs with an appropriate analysis on each MMF harmonic spectrum is lacking. Actually, as previously mentioned, the IMs equipped with squirrel cage in the rotor are very sensitive to air-gap flux density harmonics and it seems that this problem was not solved completely with above solutions especially for the three phase case. However, it is found that in some specific combinations of phase and slot numbers, concentrated windings can provide close performances compared to DW [66]. Nonetheless, it is clear that using a multiphase arrangement impacts on the equipment needed for the electric machine supply preventing the possibility to use a single three-phase inverter as practically preferable in most applications. In the three phase machine case, some incomprehensive performance comparison studies have been addressed [58–63] still without pointing out the potential FSCW configurations that may present comparable performance with respect to the DW counterpart.

1.5.5.2 Problem description and study motivation

In squirrel cage three phase IMs, the torque production depends on the interaction between the stator MMF and the rotor MMF produced by the induced rotor currents. In machines with FSCW; if the windings are excited with a certain frequency, a number of torque and rotor bar losses are generated at various slips due to stator winding space harmonics. According to the direction of rotation of these harmonics, some of them will produce negative torque tending to brake the main fundamental torque as well as generating excessive rotor bar losses. Despite of the several attempts presented in the literature to ameliorate the performance of such a motor by reducing some orders of the stator MMF harmonics, no effective solution have been presented for the three phase machine case. This may be due to the fact that all these attempts do not necessarily target the most harmful harmonic orders laying behind the deterioration of the machine performance. From this arises the need to further investigate on the effect of each harmonic component on the machine performance characteristics for different slot/pole configurations and for different operating ranges. On the other hand, the potentialities of applying FSCW configurations in inverter-fed induction machines are worth to be looked over. To the best of the author's knowledge, no comprehensive study examining quantitatively the effects of the different armature MMF harmonics of the FSCW on the performance of the IMs.

The aim of this study is to present a comprehensive investigation to reveal the influence of MMF harmonic content on the performance characteristics of the FSCW squirrel cage IMs. For that, several methodologies are considered for the sake of an accurate quantification of the effect of each harmonic order on the torque performance and the efficiency of the machine. Typically, time-stepping FEA (TSFEA) simulations are usually used where the detailed geometry of the machine has to be considered to predict the overall machine performance taking into account the contribution of all stator harmonics. In spite of the accuracy of this method, it is impossible to identify the effect of each harmonic order on the performance of the machine. As a fast alternative to FEA simulations, Time Harmonic Finite Element analysis (THFEA) is considered. In this case, a machine with a squirrel cage in the rotor and a current sheet spread in the stator inner bore to produce the air-gap revolving field generated by each space harmonic component is modeled. This type of analysis provides insights as to the contribution of various space harmonic components to torque production as well as to rotor bar losses at various rotor speeds (slip values). Saturation effects are not taken into account since the THFEA is a linear analysis. In order for a faster prediction of the several harmonics effect on the machine behaviour, a simple analytical method based on the IM equivalent circuit is presented for a fast estimation of the torque and losses generated by each harmonic order separately. The application results of the proposed techniques on an example 9-slot/8-pole FSCW squirrel cage IM (Figure 1.42-(a)) are presented and compared with time-stepping transient FEA to evaluate the effectiveness of the proposed techniques. For the sake of a comprehensive comparison, an 8-pole DW squirrel cage IM motor (Figure 1.42-(b)) taken as a reference machine is suitably modeled having the same geometric specifications and key operation to be comparable to the FSCW IM study case. The performance characteristics such as torque and power losses of both type of machines are compared extensively to evaluate the viability of FSCW on IMs. Starting capability as well as steady state performance are assessed to investigate the influence of MMF harmonics on such performance characteristics of IMs.

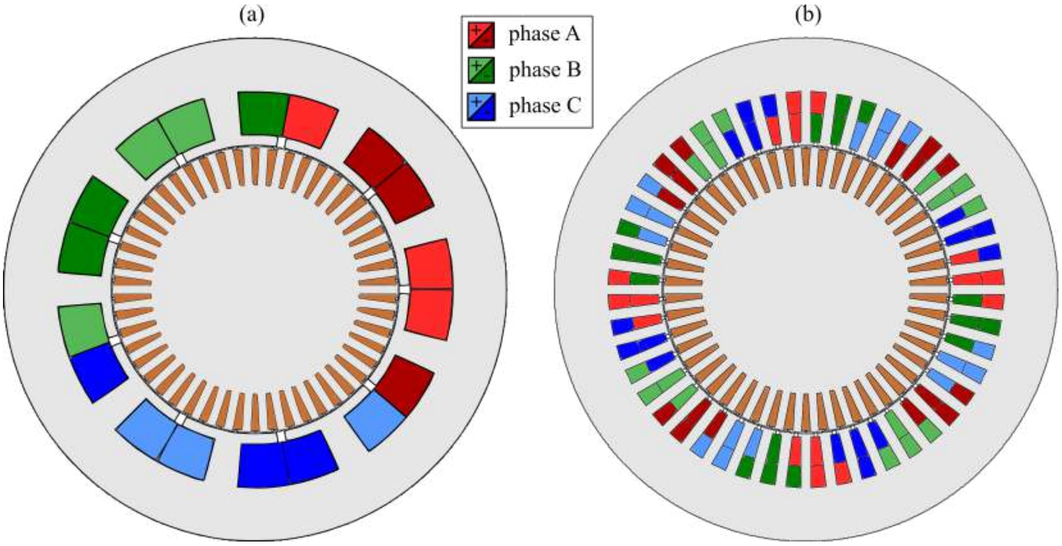

Figure 1.42: Cross sections of the squirrel cage IMs examples under study, **(a)** equipped with a 9-slot/8-pole FSCW stator; **(b)** equipped with a DW stator.

1.5.5.3 Study of the problem by THFEA

In order to clearly quantify the effects of individual harmonic components, a simplified machine model with a squirrel cage in the rotor and an infinitely permeable non-conductive ferromagnetic smooth stator with uniform air-gap g and radius $R_s = R_r + g$ is considered as shown in Figure 1.43. Since the slotting effect is not taken into account, the stator MMF can be represented by an equivalent linear current distribution $\Lambda(\theta, t)$ spread around the stator bore expressed in the stator reference frame (r, θ) such that:

$$\Lambda(\theta, t) = \frac{1}{R_s} \frac{\partial}{\partial \theta} M_s(\theta, t) \tag{1.113}$$

By substituting (1.18) in (1.113), the equivalent linear current density can be expressed in complex form as:

$$\overline{\Lambda}(\theta, t) = \sum_{n=1..\infty} \overline{\lambda_n}(\theta) e^{i\omega t} \tag{1.114}$$

where $\overline{\lambda_n}(\theta)$ is the equivalent current density for the n^{th} harmonic order written as:

$$\overline{\lambda_n}(\theta) = \pm \frac{1}{R_s} n m_n^{\pm} e^{\pm in\theta} \tag{1.115}$$

Thus, each n^{th} space harmonic is represented by a thin fictitious current sheet spread around the stator bore surface characterized by the linear current density $\overline{\lambda_n}(\theta)$ [3]. Expression (1.114) is useful because it proves that thanks to the superposition principle, it is possible to approach the computation of the torque and rotor losses through a set of THFEA simulations for each harmonic order n corresponding to the MMF harmonic amplitude $m_n^{\pm}$.

Since we are dealing with FSCW IM case, a rich harmonic content is generated where each harmonic component rotates at different speeds from the fundamental. The frequency imposed for each THFEA simulation needs to be determined depending on the harmonic slip value S_n which depends by definition on the fundamental slip value S_p. Indeed, the fundamental slip value is defined as the function of the synchronous speed $N_{sync} = \frac{60f}{p}$ and the rotational speed N_{rot} as:

$$S_p = \frac{N_{sync} - N_{rot}}{N_{sync}} \tag{1.116}$$

The harmonic slip for the co-rotating harmonics (harmonics rotating like the rotor) is computed as follows:

$$S_n = \frac{N_{sync,n} - N_{rot}}{N_{sync,n}} = \frac{\frac{pN_{sync}}{n} - N_{rot}}{\frac{pN_{sync}}{n}} = (1 - \frac{n}{p}) + \frac{n}{p} S_p \tag{1.117}$$

As for the counter-rotating harmonics (rotating opposite to the rotor), the corresponding slip is determined as:

$$S_n = \frac{N_{sync,n} + N_{rot}}{N_{sync,n}} = \frac{\frac{pN_{sync}}{n} + N_{rot}}{\frac{pN_{sync}}{n}} = (1 + \frac{n}{p}) - \frac{n}{p} S_p \tag{I.118}$$

Thus, for each rotor speed of the machine corresponding to a fundamental slip S_p, the harmonic slips S_n are calculated and the frequency of each THFEA simulation is determined as $\omega_n = S_n \omega$ where ω is the stator frequency. The torque T_n and rotor Joule losses P_n produced by each harmonic order for any rotor speed can then be obtained by running a THFEA on the simplified model presented in Figure I.43 where the complex current density $\overline{\lambda_n}(\theta)$ given by (I.115) is impressed on the inner stator surface at a frequency equal to ω_n.

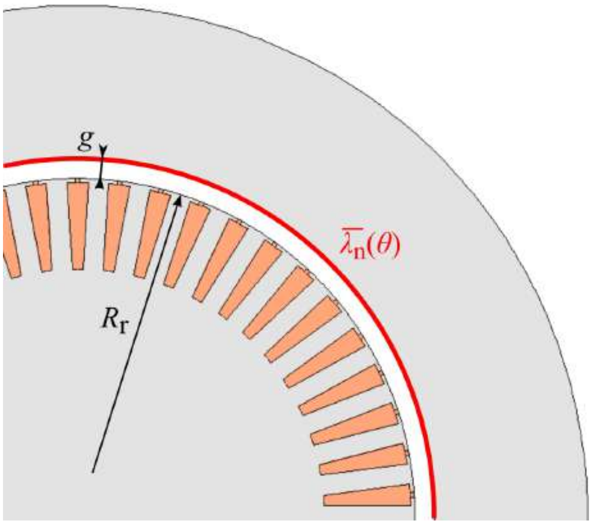

Figure I.43: THFEA model with fictitious linear current density spread on the stator surface for the n^{th} harmonic at frequency $n\omega$.

Once the torque and Joule losses for all significant harmonic orders n are extracted, the total quantities can be determined by summing up all the results caused by the whole air-gap field such that for the total torque:

$$T_{tot} = \sum_{n=1..\infty} T_n \tag{I.119}$$

and for the total rotor Joule losses:

$$P_{tot} = \sum_{n=1..\infty} P_n \tag{I.120}$$

It is worth to be noted that applying the superposition principle to the generated electromagnetic torque as per (I.119) and to the rotor power losses as per (I.120) is possible because for each harmonic order n, currents of different frequencies are induced in the rotor bars and, hence, torques associated with all values of n can be summed up as well as for the generated power losses.

1.5.5.4 Study of the problem analytically based on harmonics equivalent circuit

Usually in IMs, the classical steady state equivalent circuit shown in Figure 1.42 is commonly used to study the machine performance [68, 69], where R_1 and X_1 are the stator winding resistance and leakage reactance, R_2 and X_2 are the rotor resistance an leakage reactance referred to the stator, X_m is the magnetization reactance and S is the rotor slip. Since DW stator topologies are the most popular winding layouts employed in IMs, only the fundamental air-gap MMF harmonic contributes to the electromechanical energy conversion. The amplitude of the higher order harmonics are usually very low compared to the amplitude of the fundamental, hence, their effect on the net output torque in generally limited. For that, the single phase equivalent circuit of the DW IM case usually assumes a sinusoidal air-gap field wave from of the fundamental component and neglects the presence of harmonics. Based on the aforementioned assumption, for a p-pole squirrel cage IM equipped with a DW, the equivalent circuit parameters are determined as in [68] and the machine performance characteristics are calculated by considering the fundamental slip S_p as the rotor slip.

As for IMs with FSCW, the corresponding equivalent circuit needs to involve the influence of MMF spacial harmonics [58, 70]. In order to separately quantify the effect of each space harmonic, an equivalent circuit corresponding to the n^{th} harmonic is proposed in Figure 1.45. In this circuit, each harmonic frequency forms an individual electric machine with n pole pairs where $X_{m,n}$ refers to the harmonic magnetization reactance, $R_{2,n}$ and $X_{2,n}$ are the rotor resistance and leakage reactance of the n^{th} harmonic respectively and S_n is the rotor harmonic slip as defined in (1.118). For the sake of simplicity, no voltage drop from the stator side is considered i.e. the stator winding resistance as well as the leakage reactance are neglected. This assumption is in accordance with the simplifications made for the IM in the previous paragraph 1.5.5.3 which considers no stator slots and windings. For a given harmonic order n, the equivalent circuit parameters $X_{m,n}$, $R_{2,n}$ and $X_{2,n}$ as well as the harmonic stator current $I_{1,n}$ and the harmonic rotor current reported to the stator $I_{2,n}$ can be determined as presented in Appendix A. Once the equivalent circuit is properly defined, it is possible to determine the rotor Joule losses $P_{ana,n}$ and the developed torque $T_{ana,n}$ for each harmonic order as follows:

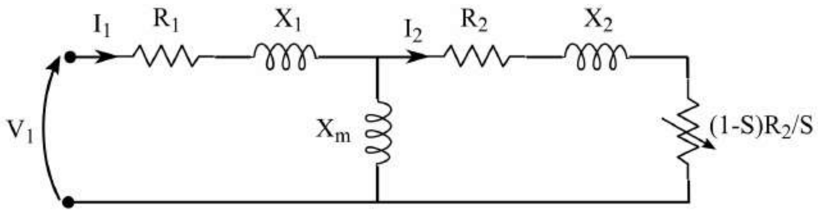

Figure 1.44: Conventional equivalent circuit of IMs.

$$P_{ana,n} = 3R_{2,n}I_{2,n}^2 \tag{1.121}$$

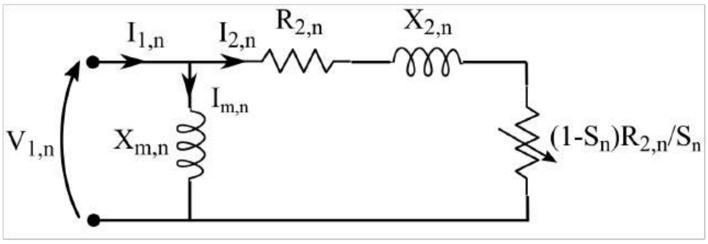

Figure 1.45: Simplified equivalent circuit corresponding to the n^{th} stator MMF space harmonic of an IM.

$$T_{ana,n} = \frac{\frac{P_{ana,n}}{S_n}}{\Omega_n} = \frac{3R_{2,n}I_{2,n}^2}{S_n\Omega_n} \tag{1.122}$$

where $\Omega_n = \dfrac{2\pi}{60}N_{sync,n}$ is the harmonic synchronous speed in rad/s. Based on the superposition principle, the analytically predicted total torque $T_{ana,tot}$ and rotor Joule losses $P_{ana,tot}$ can be obtained by summing up the different individually computed harmonic torque and losses using the equivalent circuit as:

$$T_{ana,tot} = \sum_{n=1..\infty} T_{ana,n} \tag{1.123}$$

and for the total rotor Joule losses:

$$P_{ana,tot} = \sum_{n=1..\infty} P_{ana,n} \tag{1.124}$$

Despite its simplicity, the equivalent circuit analytical method may provide an instantaneous prediction of each harmonic influence on the IM behavior in terms of torque and rotor losses. In what follows, the accuracy and the effectiveness of such a method will be assessed by comparison with THFEA and TSFEA methods.

1.5.5.5 Application of the THFEA and analytical methods and results discussion

As an example, a squirrel cage IM equipped with a 9-slot/8-pole FSCW configuration in the stator as illustrated in Figure 1.42-(a) is considered which characteristic data are summarized in Table 1.13. This machine is modeled and reproduced through the described THFEA method presented in Figure 1.43 and the analytical method based on the equivalent circuit approach explained in paragraph 1.5.5.4. It is worth noticing that, in order to further simplify the process, the effect of the rotor cage end rings is not accounted for while applying the THFEA based method. The same assumption is considered for the analytical method as could be noticed from the rotor bar resistance calculations presented in Appendix A to guarantee comparability between both methods. Since the main goal of this study is to give insights into the impact of individual harmonic on the machine performance, the same conclusions can be drawn on the relative torque and Joule losses even without considering the end rings.

Table 1.13: Dimensions and ratings of the 9-slot/8-pole FSCW IM example.

Z	Number of slots	9	L	Core length	120 mm
p	Number of pole pair	4	V_{max}	Rated phase peek voltage	572 A
Z_b	Number of rotor bars	50	I_{max}	Rated phase peek current	10 A
R_s	Stator outer radius	70 mm	f	Rated frequency	50 Hz
R_r	Rotor radius	39.67 mm	N_t	Number of turns per phase	300
g	Air-gap width	0.33 mm	σ_b	rotor bars electrical conductivity	58 MS/m
J	Current density	$4\ A/mm^2$	k_w	Winding factor	0.945

As can be noticed from the space harmonic spectrum of the 9-slot/8-pole FSCW layout presented in Figure 1.46, several harmonic components have significant amplitude with respect to the fundamental which can create high currents that may generate significant torques. To quantify the impact of such harmonics, a larger range of harmonic components are taken into account in the study which varies from the 1^{st} to the 40^{th} harmonic order. For a comprehensive comparison, results of THFEA simulations of torque vs speed characteristics (in per unit based on the pullout torque of the fundamental harmonic component) of the harmonic components under consideration are compared in Figures 1.47. The bars Joule losses function of the rotational speed generated from each considered harmonic component are similarly illustrated in per unit (relative to the maximum power loss value of the fundamental) in Figure 1.48.

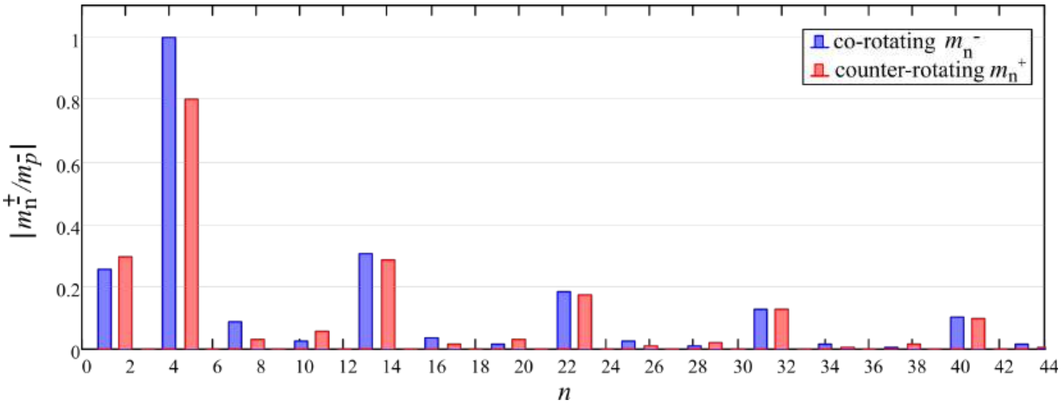

Figure 1.46: MMF space harmonic spectrum of the 9-slot/8-pole FSCW layout.

Looking at Figure 1.47, it can be clearly understood that the harmonic components contribute differently to torque generation depending on their rotational direction. Indeed, it can be noticed that, in the low speed region and high slip values (starting region), higher harmonic orders rotating like the rotor (such as harmonics number 13, 22, 31, 40...) produce a positive torque while the ones rotating opposite to the rotor (such as harmonics number 5, 14, 23, 32...) contribute negatively to the torque production. As for the operating speed region (high speed region near to the synchronous speed with low slip values), it can be easily noticed that regardless of the sense of rotation, all harmonic orders generate a negative torque. This is because in such speed region, the majority of higher harmonic orders operate in the generator region where the harmonic field rotates in the opposite direction even for the case of co-rotating harmonics. Conversely, in

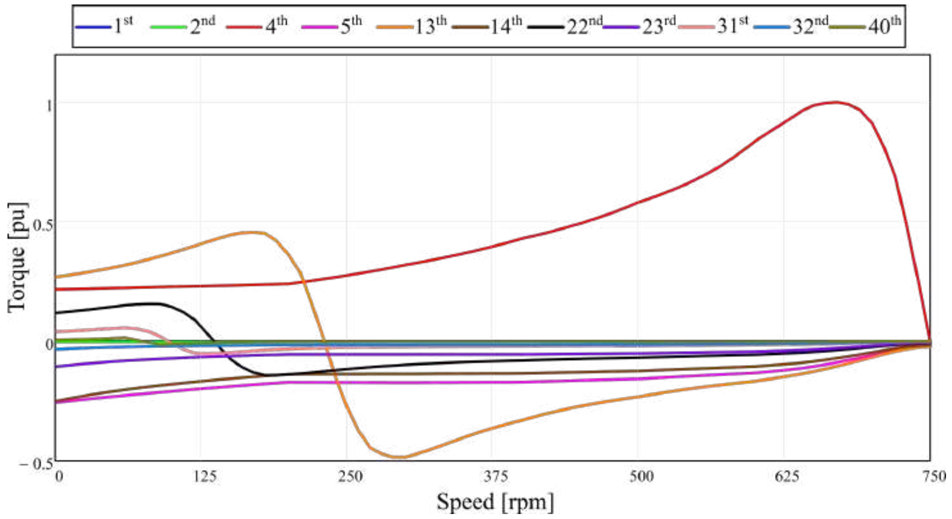

Figure 1.47: Comparison of the torque vs speed curves produced by the individual space harmonics of the example 9-slot/8-pole FSCW IM. Only harmonic orders of significant MMF amplitude with respect to the fundamental are presented.

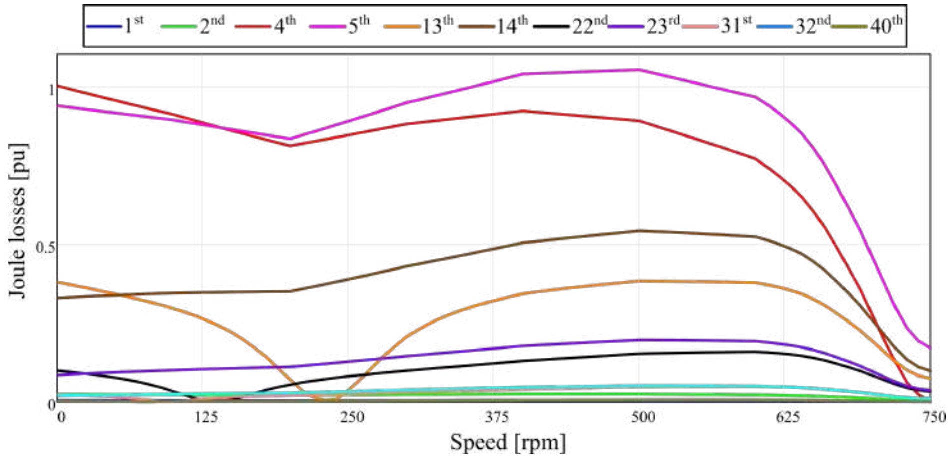

Figure 1.48: Comparison of the rotor Joule losses generated by the individual space harmonics of the example 9-slot/8-pole FSCW IM. Only harmonic orders of significant MMF amplitude with respect to the fundamental are presented.

spite of their significant amplitude with respect to the fundamental, the 1^{st} and 2^{nd} subharmonics produces very low torque with negligible relative amplitudes in both low and high speed ranges. From the power losses viewpoint, it is shown from Figure 1.48 that, compared to the fundamental losses, higher order harmonic losses are relatively high. For instance, it is found that the losses caused by the 5^{th} harmonic are higher that the fundamental losses especially in the high speed range mainly because of the strong coupling between this harmonic and the rotor. Moreover, a significant impact of higher order harmonics such as the 13^{th} and 14^{th} can be clearly seen as they may approximately produce 40% and 50% of the fundamental losses respectively. Furthermore, it can be clearly understood that in the operation speed range with low slip values, higher order harmonics actually still have a high impact on the losses even if they seem to have a slight impact on the torque production for the same speed region. This fact certainly results in the deterioration of the machine performance especially in terms of efficiency. It is worth mentioning that differently than expected, this study proves that high harmonic orders should not be neglected. The accumulation of the total effects of each harmonic engenders a considerable braking in the torque performance while generating high additional losses leading to a poor machine efficiency.

To validate the efficiency of the proposed THFEA and analytical methods, results are compared with TSEFA. For that, an accurate modeling of the machine geometry including the details of the stator winding structure have to be considered. Transient TSFEA for different rotor speeds (slip values) is applied to the 9-slot/8-pole IM example machine illustrated in Figure 1.42-(a) which characteristics are displayed in Table 1.13. This captures the overall MMF harmonic effect on the torque and losses generation. The ringing effect is neglected here as well to guarantee the comparability of the results with the other presented methods. As to magnetic saturation, its impact on the machine performance on the presence of harmonic is neglected in this study since the main target consists only in visualizing the behaviour of the IM under the effect of a rich harmonic content. To be compared with TSFEA, the total torque and Joule losses from the TSFEA and analytical methods are calculated by summing up the individual harmonic contributions as done by equations (1.119), (1.120), (1.123) and (1.124). The torque vs speed characteristics and the rotor Joule losses predicted by the different approaches of the IM under study are illustrated in Figures 1.49 and 1.50 respectively. The good accordance between the THFEA and TSFEA results proves the effectiveness of the THFEA method in spite of the simplifying assumption considered by neglecting the stator slots and winding.

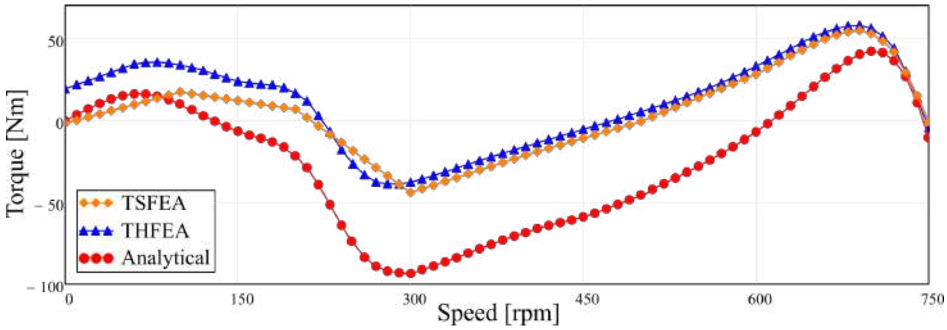

Figure 1.49: Comparison of the torque vs speed characteristics of the different.

In addition to its capability to evaluate the effect of each harmonic individually, the proposed THFEA method can be considered as a fast alternative to simulate IMs of high space harmonic content to overcome the shortcomings of TSFEA related to the computational burden and model complexity. However, regarding the analytical approach based on the harmonic equivalent circuit, the estimated performance characteristics seem to be far from the TSFEA results considered as reference. Indeed, it can be seen from Figure 1.49 that the analytical approach underestimates the torque for almost all the speed range. On the other hand, the same approach overestimates the

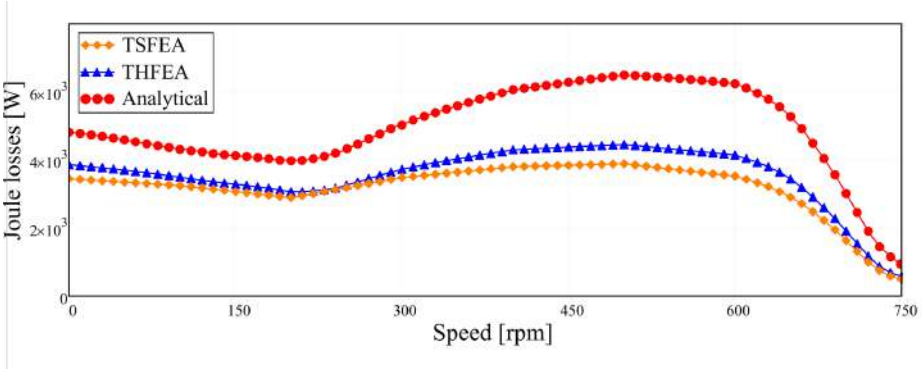

Figure 1.50: Comparison of the induced torques and rotor Joule losses generated by several harmonic components resultant from THFEA and analytical methods.

prediction of the rotor Joule losses as shown in Figure 1.50.

To explain this fact, a comparison of the analytical torque and rotor losses of several harmonics with the THFEA results is illustrated in Figure 1.51. It can be clearly observed that, the higher is the harmonic order, the larger is the gap between analytical and THFEA results. Indeed, one can notice that, for the fundamental and the other nearby MMF harmonic components such as the 1^{st}, 2^{nd} and 5^{th}, the analytical and THFEA torque vs speed curves and Joule losses curves are almost superimposed. For higher harmonic orders like the 13^{th} and 22^{nd}, the analytically predicted torque seams to be higher in absolute value for the speed values different from the harmonic synchronous speed. The same observation can be made for the predicted rotor losses. This shows that the analytical computation of harmonic torque and losses based on the corresponding harmonic equivalent circuit loses its reliability for high harmonic orders. One reason behind this is that the number of bars of the squirrel cage are suitably chosen to work solely with the fundamental component of the stator MMF in such a way to avoid magnetic locking, excessive noise and vibration [69]. A minimum number of bars per pole has to be selected (usually set to 4 [71]) in order to guarantee a strong level of magnetic coupling between the rotor and stator. By considering each harmonic frequency as an individual electrical machine modeled, the number of bars per pole decreases as the number of harmonic order rises which weakens the coupling with the rotor. This fact is not taken into account in the considered harmonic equivalent circuit presented in Figure 1.45 which explains the overestimated results with respect to THFEA.

Finally, what evidently emerges is the strong impact of the harmonics on the starting properties of squirrel cage machines. It can be clearly deduced that the presence of the rich harmonic content caused by the 9-slot/8-pole FSCW configuration mostly brakes the fundamental starting torque making the machine unable to self-start . Hence, considering FSCW for IMs is not beneficial for the starting performance which makes it unsuitable for Direct-On-Line (DOL) starting applications.

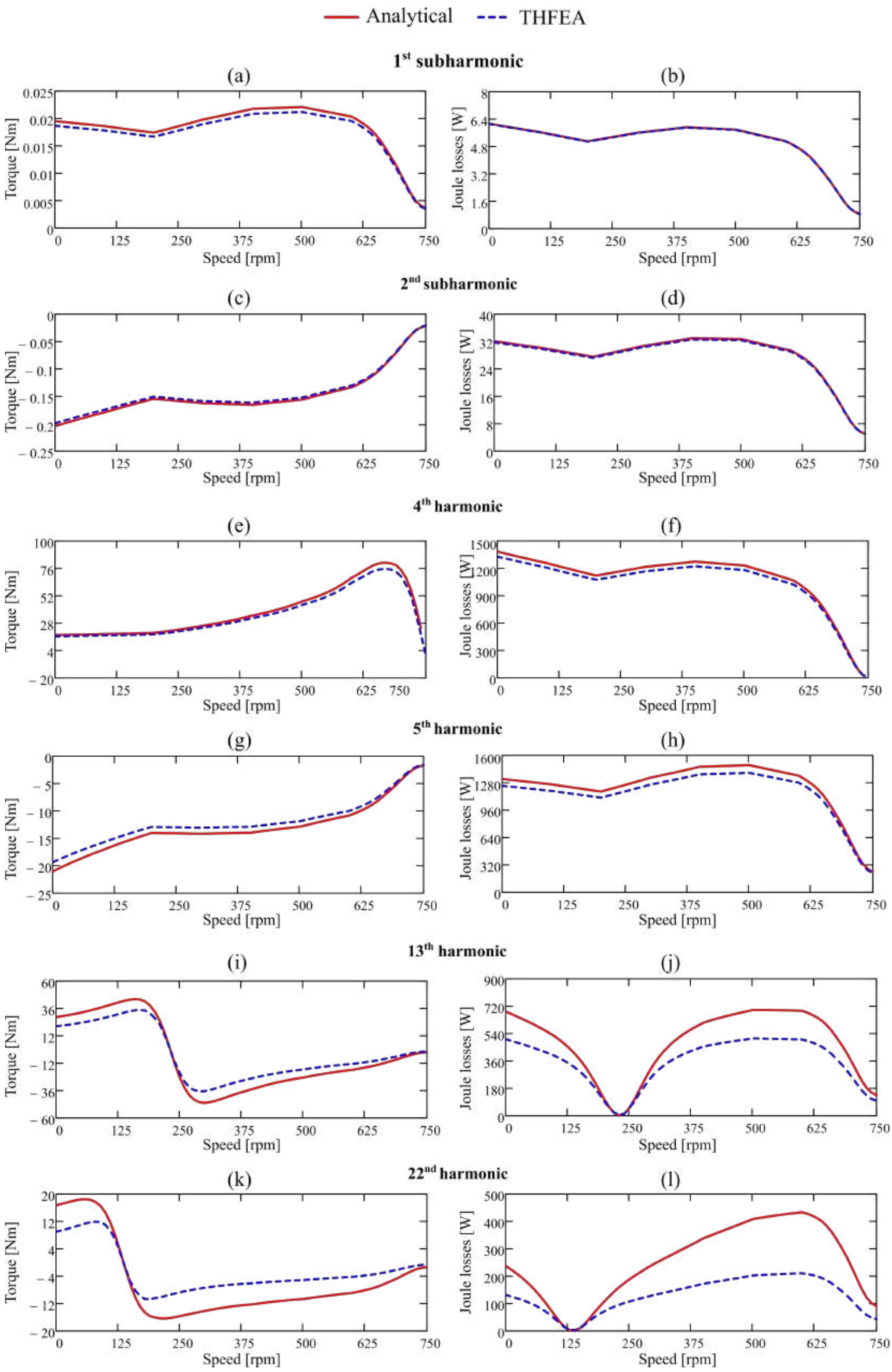

Figure 1.51: Comparison of the induced torques and rotor Joule losses generated by several harmonic components resultant from THFEA and analytical methods.

1.5.5.6 Performance comparison of the FSCW against DW IMs

In this paragraph, a squirrel cage IM equipped with 48 slots and 8 poles DW as shown in Figure 1.42-(b) which characteristics are displayed in Table 1.14 is considered as machine reference. For a comprehensive comparison, the DW induction machine is designed is such a way to have the same fundamental MMF component as the FSCW machine example. For that, both designs under consideration are chosen to have the same rotor, characteristic dimensions (air-gap width, stack length,stator outer radius...), rated current, current density, number of turns per phase in series and therefore the electric loading. The DW MMF space harmonic spectrum of the 8-pole IM example is shown in Figure 1.52. It can be clearly seen that the amplitudes of the higher harmonic components are very low compared to the amplitude of the fundamental.

Table 1.14: Dimensions and ratings of the the 8-pole DW IM example.

Z	Number of slots	48	r	coil to pole pitch ratio	0.83
p	Number of pole pair	4	k_w	Winding factor	0.933
Z_b	Number of rotor bars	50	σ_b	Rotor bars electrical conductivity	58 MS/m
R_s	Stator outer radius	70 mm	J	Current density	4 A/mm^2
R_r	Rotor radius	39.67 mm	V_{max}	Rated phase peek voltage	375 A
g	Air-gap width	0.33 mm	I_{max}	Rated phase peek current	10 A
L	Core length	120 mm	f	Rated frequency	50 Hz
N_t	Number of turns per phase	300	k_w	Winding factor	0.933

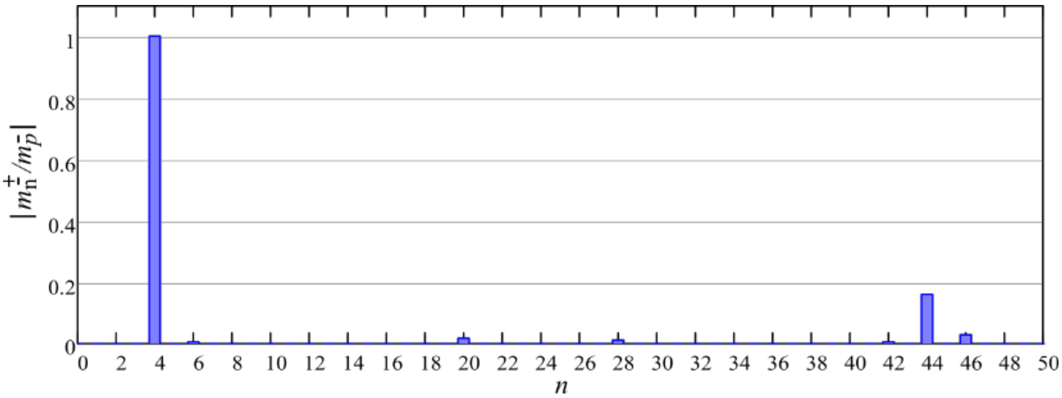

Figure 1.52: Normalized MMF space harmonic spectrum of the 8-pole DW layout.

For illustration purposes, steady state TSFEA simulations are performed for both FSCW and DW example machines which are supposed to operate at different speeds (slip value). The investigation only focuses on the behaviour of the machines in the high speed region (low slip values). In fact, comparing the starting capability of the DW IM with The FSCW one is not worth considering since it can be intuitively understood that FSCW IMs cannot compete with their DW machine counterpart when the self starting is needed. Nonetheless, DOL starting condition were simulated by TSFEA on the DW and FSCW IMs understudy by imposing the rated phase voltages V_{max} for both machines at high operational speeds. Results of comparisons in terms of torque, Joule losses and maximum phase currents function of the rotational speed are illustrated in Figure 1.53.

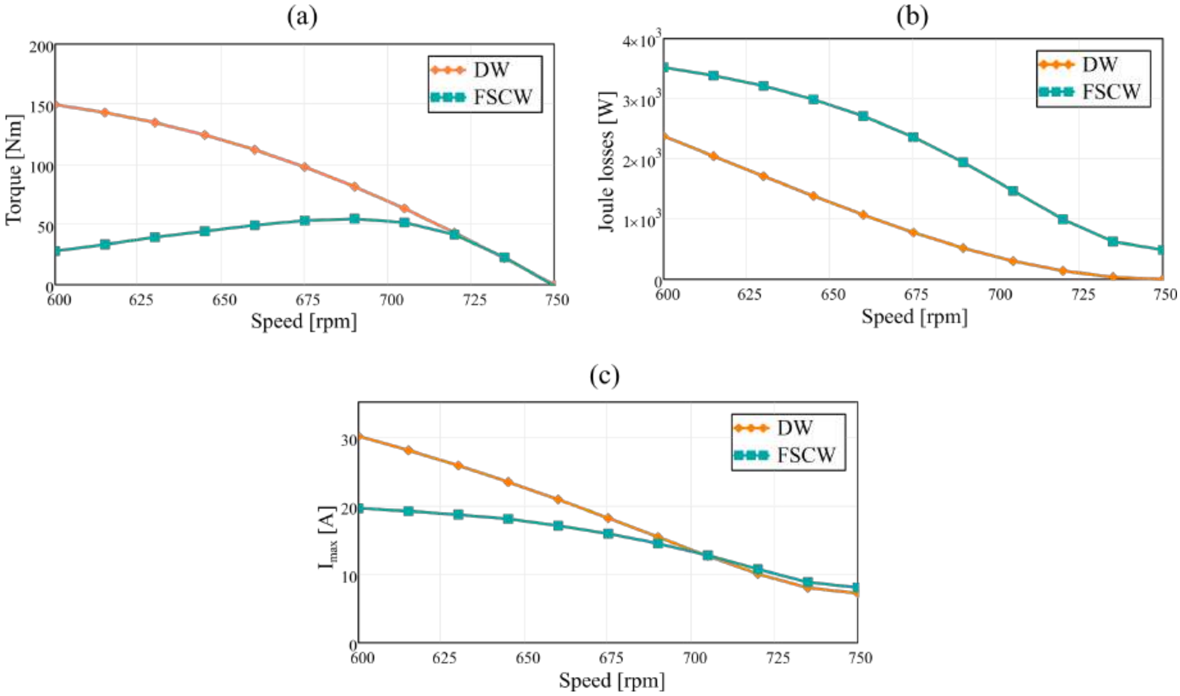

Figure 1.53: Comparison of the FSCW and DW IMs performance characteristics under rated voltage in terms of: **(a)** Torque vs speed, **(b)** Rotor Joule losses and **(c)** stator maximum phase current.

It can be seen from Figures 1.53-(a) and (c), by imposing the rated voltage, the FSCW and DW IMs can have the same torque performance for very low slip values (for speeds higher then 720 rpm corresponding to slip values less then 0.04) and consume almost the same phase current. However, for the same speed region, excessive rotor Joule losses produced by the FSCW IM are observed in Figure 1.53-(b) which may exceed ten times the losses produced by the DW machine configuration. Furthermore, it can be seen that, while the FSCW machine has already reached its peak torque at a speed equal to 690 rpm (at 0.08 slip), the DW machine torque is still rising for lower speed values leading to a much larger operating range with respect to the FSCW machine. Such behaviour of the torque speed characteristic is not common and does not reflect the reality since the the rotor cage end-ring effect is not considered in our case. Again, the same conclusion can be drawn here regarding the capability of the FSCW IM to be used as a direct-on-line plugged machine. On the other hand, in case of inverter-fed machine, operating parameters can be set in order for the machine to work in steady-state operating region under the rated phase current. For this reason, further investigations on the potentiality of FSCW IM to be employed by inverter-fed machines applications are worth to be looked on.

Thereby, the steady state behaviour of both machines understudy are simulated by TSFEA for high speed values imposing a constant rated current I_{max}. Simulation results in terms of torque vs speed characteristics, rotor Joule losses and maximum phase voltages are displayed in Figure 1.54. Regarding the torque performance, it appears in Figure 1.54-(a) that both machines understudy have comparable behavior at high speed range at steady state. In contrast, a huge constant gap between the rotor losses trends of both machines can be clearly seen in Figure 1.54-(b). The FSCW IM generates more than three times the rotor Joule losses induced by DW machine which is true for all the considered range of speed. Actually, this can be predicted from the results of the studies on the individual harmonics which showed that all harmonic currents induced in the rotor bars generate considerable losses even at low slip values. In fact, even at synchronous speed for which no Joule losses are produced by the DW machine case, excessive losses induced by the harmonic currents of different frequencies are produced by the FSCW stator. Therefore, although the steady state torque capability of the FSCW IM seems promising in contrast with the classically adopted DW layout, this kind of machine shows a very poor performance in terms of efficiency. Another observation which can be made from Figure 1.54-(c) is that, in order to maintain the same loading current, the FSCW machine needs more voltage to ensure the same torque performance as the DW one. This voltage difference can be explained in a major part by the presence of harmonics which create different additional voltages to be summed up with the fundamental one.

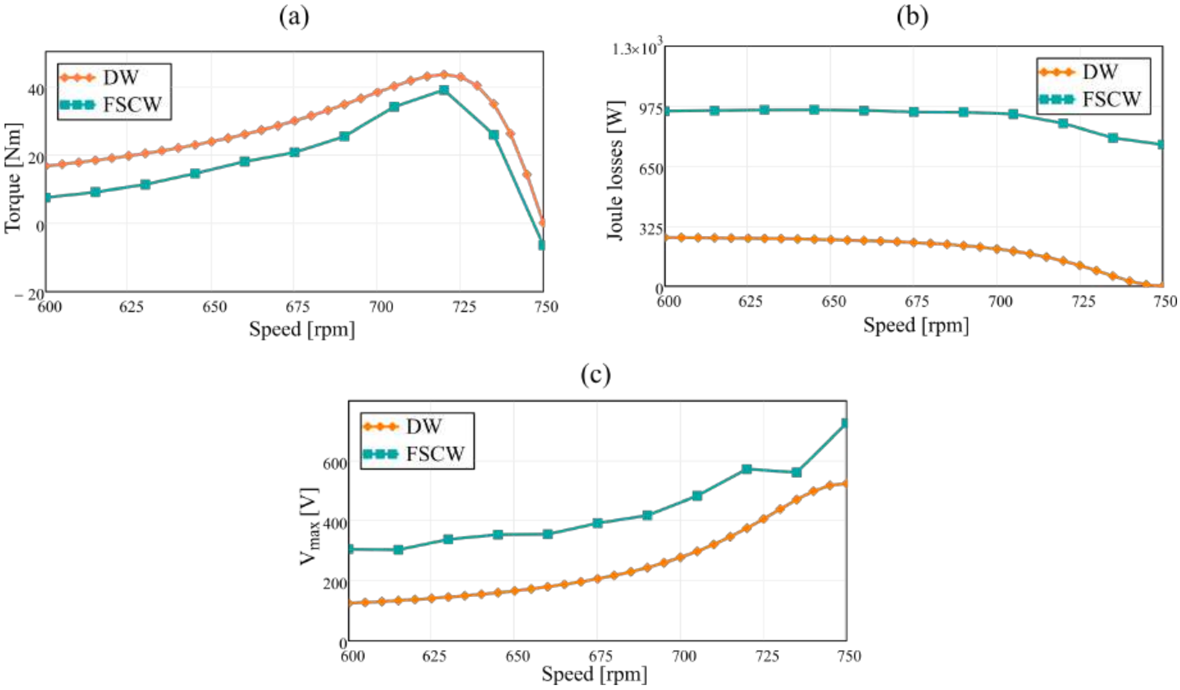

Figure 1.54: Comparison of the FSCW and DW IMs performance characteristics under rated current in terms of: **(a)** Torque vs speed, **(b)** Rotor Joule losses and **(c)** stator peak phase voltage.

1.5.5.7 Potentials of FSCW multilayer quadratic optimization applied to squirrel cage IMs

The main motivation behind the substantial investigation on the impact of the different harmonic produced by conventional FSCW on the squirrel cage IM performance is to identify the harmful harmonic contributing the most to the deterioration of the machine performance. This allows to quantitatively address the tradeoffs involved using FSCW in induction machines with the aim of investigating on the potentialities of this type of machine to be optimized by quadratic programming. In particular, exploring the performance characteristics of the 9-slot/8-pole FSCW IM example in terms of electromagnetic torque and efficiency gave insights into the specific harmonics causing parasitic effects and degenerating the machine performance. Indeed, it was shown that the most serious impact on the torque and rotor losses originate from the accumulation of the individual effects of the several harmonics of significant amplitude. For the chosen example, these harmonics (such as 5^{th}, 13^{th}, 14^{th}, 22^{nd}, 23^{rd}...)-according to the relation stated in (1.52)-are all related to the fundamental in the sense that they vary proportionally to it as shown in Figure 1.35. This implies that no kind of optimization (regardless of the algorithm used) can be effective in reducing these harmonics without reducing the fundamental exactly by the same amount. Despite the existence of some harmonic orders that may be reduced by the quadratic optimization (because of their independence from the fundamental), their influence on the machine performance appears to be negligible. For instance, based on the results analysis presented previously, it is found that the subharmonics (that can be affected by the optimization) produce a very low torque and losses despite their significant amplitude. The same conclusion can be also drawn for the other slot/pole FSCW configurations since it can proved that, in all cases, problematic harmonics consists of the higher order harmonics usually with significant amplitude which are "linked" to the fundamental. On the other hand, some FSCW slot/pole configurations were found to have promising results in terms of torque production such as the 12-slot/8-poles configuration [59] which is not suitable for optimization by the proposed quadratic algorithm. Consequently, alleviating the drawbacks of the FSCW rich harmonic content applied to squirrel cage IMs on the machine performance is not possible by multilayer arrangement through quadratic optimization approach.

1.6 Conclusion

FSCWs in three-phase permanent-magnet machines are known to bring important advantages, especially from the manufacturing point of view, but also to have negative impacts on machine performance due to their richness in airgap MMF space harmonics. It is already known that increasing the number of layers and also using coils with different number of turns can be beneficial for reducing FSCW harmonics. So far, however, FSCW design optimization has been usually approached on a case-by-case basis and finding the optimum, though extensive theoretical or heuristic reasoning, for any individual slot/pole combination. In this Part, a general and systematic methodology has been presented to optimize the FSCW of the three-phase SPM machine through multilayer winding quadratic programming. An overview of the potentials and limits of FSCW optimization has been discussed resorting to multiple-layer arrangements when the target is to reduce three major performance issues, namely: UMP, torque ripple and permanent magnet eddy-current losses. It has been shown that the three parasitic phenomena in question are caused by different groups of space harmonics and the FSCW optimization, regardless of the algorithm used, is intrinsically incapable of suppressing certain well-defined space harmonics. In particular, it has been emphasized that some space harmonics can be necessarily reduced by the same amount as the MMF fundamental independently of the multilayer winding layer being adopted. It has been illustrated how this fact makes design optimization effective only if applied to a limited number of slot/pole combinations and how the slot/pole combinations for which useful results can be expected introducing optimized multilayer arrangements strongly vary depending on the objective. In particular, exploring combinations with number of slots in the range between 3 and 27 and number of poles in the range between 2 and 24, the following conclusions can be drawn:

- UMP reduction can be achieved for only two slot/pole combinations, namely 21 slot/ 16 poles and 27 slot/ 20 poles,
- torque ripple can be effectively reduced only on those slot-pole combinations for which it already has very small values when the winding is conventionally designed with the star-of-slot method,
- permanent-magnet loss reduction is the goal for which design optimization can be effectively applied to the widest set of slot-pole combinations and leading to the largest benefits.

Finally, an attempt to examine induction machine performances with FSCW has been presented in order to provide insights on the behaviour of such winding layout on the IM performance for the sake of a possible application of the optimization approach. For that, a fast computation approach to compute the impact of the individual harmonic components in terms of torque and cage Joule losses through THFEA has been proposed using a simplified model where the stator winding is replaced by a an equivalent current sheet reproducing the harmonic air-gap field. Approaching the problem analytically based on the harmonic equivalent circuit could be an alternative for an instantaneous prediction of the harmonics impacts on the machine performance. The sum of the overall effects of the single harmonics resultants from both methodologies has been compared with TS-FEA applied on a FSCW IM machine example. A shortcoming of the analytical method has been shown which consists of its inaccuracy in predicting torque and Joule losses for high harmonic orders. Based on the analysis results of the studies conducted on the different harmonic impacts, it has been possible to identify the specific harmonic components responsible for the deterioration of the IM performance. Consequently, the FSCW IM was proven to be unsuitable for self starting DOL applications. For the sake of comprehensiveness, the FSCW machine case has been compared with a standard distributed winding machine taken as a reference. Therefore, TSFEA simulations have been performed on both machines working for high speeds range under steady state conditions. The FSCW IM solution was shown to be capable to have comparable torque capability with the DW IM. However, the penalty was always the excessive additional rotor bars losses due to the higher order harmonic MMF components. In the end, it was shown how the quadratic optimization is incapable to reduce the harmful harmonics without reducing the MMF fundamental by the same amount. This implies that no kind of optimization (regardless of the algorithm used) can be effective to reducing this harmonics in order to ameliorate the IM performance when equipped with FSCW architecture.

Bibliography

[1] A. M. EL-Refaie, “Fractional-slot concentrated-windings synchronous permanent magnet machines: Opportunities and challenges,” *IEEE Transactions on Industrial Electronics*, vol. 57, no. 1, pp. 107–121, 2010.

[2] E. Fornasiero, L. Alberti, N. Bianchi, and S. Bolognani, “Considerations on selecting fractional-slot nonoverlapped coil windings,” *IEEE Transactions on Industry Applications*, vol. 49, no. 3, pp. 1316–1324, 2013.

[3] A. Tessarolo, F. Luise, S. Pieri, A. Benedetti, M. Bortolozzi, and M. De Martin, “Design for manufacturability of an off-shore direct-drive wind generator: An insight into additional loss prediction and mitigation,” *IEEE Transactions on Industry Applications*, vol. 53, no. 5, pp. 4831–4842, 2017.

[4] C. M. Spargo, B. C. Mecrow, J. D. Widmer, C. Morton, and N. J. Baker, “Design and validation of a synchronous reluctance motor with single tooth windings,” *IEEE Transactions on Energy Conversion*, vol. 30, no. 2, pp. 795–805, 2015.

[5] X. Zhang, J. Ji, J. Zheng, and X. Zhu, “Improvement of reluctance torque in fault-tolerant permanent-magnet machines with fractional-slot concentrated-windings,” *IEEE Transactions on Applied Superconductivity*, vol. 28, no. 3, pp. 1–5, 2018.

[6] N. Bianchi and E. Fornasiero, “Impact of mmf space harmonic on rotor losses in fractional-slot permanent-magnet machines,” *IEEE Transactions on Energy Conversion*, vol. 24, no. 2, pp. 323–328, 2009.

[7] A. Tessarolo, “A survey of state-of-the-art methods to compute rotor eddy-current losses in synchronous permanent magnet machines,” in *2017 IEEE Workshop on Electrical Machines Design, Control and Diagnosis (WEMDCD)*, 2017, pp. 12–19.

[8] D. G. Dorrell, M. Popescu, and D. M. Ionel, “Unbalanced magnetic pull due to asymmetry and low-level static rotor eccentricity in fractional-slot brushless permanent-magnet motors with surface-magnet and consequent-pole rotors,” *IEEE Transactions on Magnetics*, vol. 46, no. 7, pp. 2675–2685, 2010.

[9] J. Y. Song, K. J. Kang, C. H. Kang, and G. H. Jang, “Cogging torque and unbalanced magnetic pull due to simultaneous existence of dynamic and static eccentricities and uneven magnetization in permanent magnet motors,” *IEEE Transactions on Magnetics*, vol. 53, no. 3, pp. 1–9, 2017.

[10] M. S. Islam, M. A. Kabir, R. Mikail, and I. Husain, "Interactive ripple harmonic minimization of fractional slot permanent magnet machines using space-shifted wye-delta winding," in *2019 IEEE International Electric Machines Drives Conference (IEMDC)*, 2019, pp. 288–294.

[11] A. S. Abdel-Khalik, S. Ahmed, and A. M. Massoud, "Low space harmonics cancelation in double-layer fractional slot winding using dual multiphase winding," *IEEE Transactions on Magnetics*, vol. 51, no. 5, pp. 1–10, 2015.

[12] Y. Wang, R. Qu, and J. Li, "Multilayer windings effect on interior pm machines for ev applications," *IEEE Transactions on Industry Applications*, vol. 51, no. 3, pp. 2208–2215, 2015.

[13] A. Sun, J. Li, R. Qu, and D. Li, "Effect of multilayer windings on rotor losses of interior permanent magnet generator with fractional-slot concentrated-windings," *IEEE Transactions on Magnetics*, vol. 50, no. 11, pp. 1–4, 2014.

[14] A. Tessarolo, M. Mezzarobba, and N. Barbini, "Improved four-layer winding design for a 12-slot 10-pole permanent magnet machine using unequal tooth coils," in *IECON 2016 - 42nd Annual Conference of the IEEE Industrial Electronics Society*, 2016, pp. 1686–1691.

[15] M. V. Cistelecan, F. J. T. E. Ferreira, and M. Popescu, "Three phase tooth-concentrated multiple-layer fractional windings with low space harmonic content," in *2010 IEEE Energy Conversion Congress and Exposition*, 2010, pp. 1399–1405.

[16] L. Alberti, M. Barcaro, and N. Bianchi, "Design of a low-torque-ripple fractional-slot interior permanent-magnet motor," *IEEE Transactions on Industry Applications*, vol. 50, no. 3, pp. 1801–1808, 2014.

[17] N. Bianchi and M. Dai Pre, "Use of the star of slots in designing fractional-slot single-layer synchronous motors," *IEE Proceedings - Electric Power Applications*, vol. 153, no. 3, pp. 459–466, 2006.

[18] A. M. Silva, F. J. T. E. Ferreira, M. V. Cistelecan, and C. H. Antunes, "Multiobjective design optimization of generalized multilayer multiphase ac winding," *IEEE Transactions on Energy Conversion*, vol. 34, no. 4, pp. 2158–2167, 2019.

[19] N. Tang and I. P. Brown, "Framework and solution techniques for suppressing electric machine winding mmf space harmonics by varying slot distribution and coil turns," *IEEE Transactions on Magnetics*, vol. 54, no. 5, pp. 1–12, 2018.

[20] A. Tessarolo, "A quadratic-programming approach to the design optimization of fractional-slot concentrated windings for surface permanent-magnet machines," *IEEE Transactions on Energy Conversion*, vol. 33, no. 1, pp. 442–452, 2018.

[21] T. F. Coleman and Y. Li, "A reflective newton method for minimizing a quadratic function subject to bounds on some of the variables," *SIAM Journal on Optimization*, vol. 6, no. 4, pp. 1040–1058, 1996.

[22] L. Alberti and N. Bianchi, "Theory and design of fractional-slot multilayer windings," *IEEE Transactions on Industry Applications*, vol. 49, no. 2, pp. 841–849, 2013.

[23] F. Luise, S. Pieri, M. Mezzarobba, and A. Tessarolo, "Regenerative testing of a concentrated-winding permanent-magnet synchronous machine for offshore wind generation—part i: Test concept and analysis," *IEEE Transactions on Industry Applications*, vol. 48, no. 6, pp. 1779–1790, 2012.

[24] A. Tessarolo, F. Agnolet, F. Luise, and M. Mezzarobba, "Use of time-harmonic finite-element analysis to compute stator winding eddy-current losses due to rotor motion in surface permanent-magnet machines," *IEEE Transactions on Energy Conversion*, vol. 27, no. 3, pp. 670–679, 2012.

[25] J. Nocedal and S. Wright, *Numerical optimization*. Springer Science & Business Media, 2006.

[26] R. F. Burbidge, "A rapid method of analysing the m.m.f. wave of a single or polyphase winding," *Proceedings of the IEE - Part C: Monographs*, vol. 105, no. 7, pp. 307–311, 1958.

[27] A. C. Smith and D. G. Dorrell, "Calculation and measurement of unbalanced magnetic pull in cage induction motors with eccentric rotors. i. analytical model," *IEE Proceedings - Electric Power Applications*, vol. 143, no. 3, pp. 193–201, 1996.

[28] D. G. Dorrell and D. Ionel, "Radial forces and vibrations in permanent magnet and induction machines," in *2012 IEEE Power and Energy Society General Meeting*, 2012, pp. 1–6.

[29] P. Frauman, A. Burakov, and A. Arkkio, "Effects of the slot harmonics on the unbalanced magnetic pull in an induction motor with an eccentric rotor," *IEEE Transactions on Magnetics*, vol. 43, no. 8, pp. 3441–3444, 2007.

[30] D. G. Dorrell, M. Hsieh, and Y. Guo, "Unbalanced magnet pull in large brushless rare-earth permanent magnet motors with rotor eccentricity," *IEEE Transactions on Magnetics*, vol. 45, no. 10, pp. 4586–4589, 2009.

[31] Z. Q. Zhu, D. Ishak, D. Howe, and J. Chen, "Unbalanced magnetic forces in permanent-magnet brushless machines with diametrically asymmetric phase windings," *IEEE Transactions on Industry Applications*, vol. 43, no. 6, pp. 1544–1553, 2007.

[32] E. Sarani, K. Abbaszadeh, and M. Ardebili, "Modeling and simulation of turn-fault and unbalance magnetic pull in induction motor based on magnetic equivalent circuit method," in *2005 International Conference on Electrical Machines and Systems*, vol. 1, 2005, pp. 52–56 Vol. 1.

[33] D. Dorrell, "The sources and characteristics of unbalanced magnetic pull in cage induction motors with either static or dynamic rotor eccentricity," in *Proceedings of the 1995 IEEE International PowerTech Conference*, 1995, pp. 229–234.

[34] P. Vijayraghavan and R. Krishnan, "Noise in electric machines: a review," *IEEE Transactions on Industry Applications*, vol. 35, no. 5, pp. 1007–1013, 1999.

[35] D. G. Dorrell, M. Popescu, C. Cossar, and D. Ionel, "Unbalanced magnetic pull in fractional-slot brushless pm motors," in *2008 IEEE Industry Applications Society Annual Meeting*, 2008, pp. 1–8.

[36] G. H. Jang, J. W. Yoon, N. Y. Park, and S. M. Jang, "Torque and unbalanced magnetic force in a rotational unsymmetric brushless dc motors," *IEEE Transactions on Magnetics*, vol. 32, no. 5, pp. 5157–5159, 1996.

[37] Y. Yokoi, T. Higuchi, and Y. Miyamoto, "General formulation of winding factor for fractional-slot concentrated winding design," *IET Electric Power Applications*, vol. 10, no. 4, pp. 231–239, 2016.

[38] P. Salminen, M. Niemela, J. Pyhonen, and J. Mantere, "Performance analysis of fractional slot wound pm-motors for low speed applications," in *Conference Record of the 2004 IEEE Industry Applications Conference, 2004. 39th IAS Annual Meeting.*, vol. 2, 2004, pp. 1032–1037 vol.2.

[39] A. Tessarolo, C. Ciriani, M. Bortolozzi, M. Mezzarobba, and N. Barbini, "Investigation into multi-layer fractional-slot concentrated windings with unconventional slot-pole combinations," *IEEE Transactions on Energy Conversion*, vol. 34, no. 4, pp. 1985–1996, 2019.

[40] H. Jussila, P. Salminen, M. Niemela, and J. Pyrhonen, "Guidelines for designing concentrated winding fractional slot permanent magnet machines," in *2007 International Conference on Power Engineering, Energy and Electrical Drives*. IEEE, 2007, pp. 191–194.

[41] R. O. C. Lyra and T. A. Lipo, "Torque density improvement in a six-phase induction motor with third harmonic current injection," *IEEE Transactions on Industry Applications*, vol. 38, no. 5, pp. 1351–1360, 2002.

[42] M. Farshadnia, M. A. Masood Cheema, A. Pouramin, R. Dutta, and J. E. Fletcher, "Design of optimal winding configurations for symmetrical multiphase concentrated-wound surface-mount pmsms to achieve maximum torque density under current harmonic injection," *IEEE Transactions on Industrial Electronics*, vol. 65, no. 2, pp. 1751–1761, 2018.

[43] K. Wang, Z. Zhu, and G. Ombach, "Torque enhancement of surface-mounted permanent magnet machine using third-order harmonic," *IEEE transactions on magnetics*, vol. 50, no. 3, pp. 104–113, 2013.

[44] Z. S. Du and T. A. Lipo, "High torque density and low torque ripple shaped-magnet machines using sinusoidal plus third harmonic shaped magnets," *IEEE Transactions on Industry Applications*, vol. 55, no. 3, pp. 2601–2610, 2019.

[45] T. M. Jahns and W. L. Soong, "Pulsating torque minimization techniques for permanent magnet ac motor drives-a review," *IEEE Transactions on Industrial Electronics*, vol. 43, no. 2, pp. 321–330, 1996.

[46] I. Petrov, P. Ponomarev, Y. Alexandrova, and J. Pyrhönen, "Unequal teeth widths for torque ripple reduction in permanent magnet synchronous machines with fractional-slot non-overlapping windings," *IEEE Transactions on Magnetics*, vol. 51, no. 2, pp. 1–9, 2015.

[47] G. J. Li, B. Ren, and Z. Q. Zhu, "Cogging torque and torque ripple reduction of modular permanent magnet machines," in *2016 XXII International Conference on Electrical Machines (ICEM)*, 2016, pp. 193–199.

[48] S. Han, T. M. Jahns, W. L. Soong, M. K. Güven, and M. S. Illindala, "Torque ripple reduction in interior permanent magnet synchronous machines using stators with odd number of slots per pole pair," *IEEE Transactions on Energy Conversion*, vol. 25, no. 1, pp. 118–127, 2010.

[49] L. Zhu, S. Z. Jiang, Z. Q. Zhu, and C. C. Chan, "Analytical methods for minimizing cogging torque in permanent-magnet machines," *IEEE Transactions on Magnetics*, vol. 45, no. 4, pp. 2023–2031, 2009.

[50] H. Toda, Zhenping Xia, Jiabin Wang, K. Atallah, and D. Howe, "Rotor eddy-current loss in permanent magnet brushless machines," *IEEE Transactions on Magnetics*, vol. 40, no. 4, pp. 2104–2106, 2004.

[51] A. M. EL-Refaie and T. M. Jahns, "Optimal flux weakening in surface pm machines using fractional-slot concentrated windings," *IEEE Transactions on Industry Applications*, vol. 41, no. 3, pp. 790–800, 2005.

[52] M. R. Shah and A. M. EL-Refaie, "Eddy current loss minimization in conducting sleeves of high speed machine rotors by optimal axial segmentation and copper cladding," in *2007 IEEE Industry Applications Annual Meeting*, 2007, pp. 544–551.

[53] N. Bianchi, S. Bolognani, and E. Fomasiero, "A general approach to determine the rotor losses in three-phase fractional-slot pm machines," in *2007 IEEE International Electric Machines Drives Conference*, vol. 1, 2007, pp. 634–641.

[54] N. Bianchi and E. Fornasiero, "Impact of mmf space harmonic on rotor losses in fractional-slot permanent-magnet machines," *IEEE Transactions on Energy Conversion*, vol. 24, no. 2, pp. 323–328, 2009.

[55] M. Olivo, A. Tessarolo, and M. Bortolozzi, "On the use of conformal mapping in the analysis of electric machines," in *2016 XXII International Conference on Electrical Machines (ICEM)*, 2016, pp. 492–498.

[56] P. Arumugam, T. Hamiti, and C. Gerada, "Estimation of eddy current loss in semi-closed slot vertical conductor permanent magnet synchronous machines considering eddy current reaction effect," *IEEE Transactions on Magnetics*, vol. 49, no. 10, pp. 5326–5335, 2013.

[57] N. Bianchi, S. Bolognani, and E. Fornasiero, "An overview of rotor losses determination in three-phase fractional-slot pm machines," *IEEE Transactions on Industry Applications*, vol. 46, no. 6, pp. 2338–2345, 2010.

[58] G. Rezazadeh, S. Vaschetto, F. Tahami, G. A. Capolino, H. Henao, and Z. Nasiri-Gheidari, "Analysis of six-phase induction motor with distributed and concentrated windings by using the winding function method," in *2018 XIII International Conference on Electrical Machines (ICEM)*, 2018, pp. 2423–2429.

[59] A. M. El-Refaie and M. R. Shah, "Comparison of induction machine performance with distributed and fractional-slot concentrated windings," in *2008 IEEE Industry Applications Society Annual Meeting*, 2008, pp. 1–8.

[60] T. Gundogdu, G. Komurgoz, and B. Mantar, "Implementation of fractional slot concentrated windings to induction machines," in *7th IET International Conference on Power Electronics, Machines and Drives (PEMD 2014)*, 2014, pp. 1–6.

[61] J. P. Bacher and A. Mütze, "Comparison of an induction machine with both conventionally distributed and fractional-slot concentrated stator windings," *e & i Elektrotechnik und Informationstechnik*, vol. 132, no. 1, pp. 39–45, 2015.

[62] A. El-Refaie and M. Shah, "Induction machine performance with fractional-slot concentrated windings," *COMPEL: Int J for Computation and Maths. in Electrical and Electronic Eng.*, vol. 31, no. 1, pp. 119–139, 2011.

[63] T. Gundogdu, Z. Q. Zhu, and J. C. Mipo, "Analysis of coil pitch in induction machines for electric vehicle applications," *IET Electric Power Applications*, vol. 14, no. 12, pp. 2525–2536, 2020.

[64] G. Dajaku, S. Spas, X. Dajaku, and D. Gerling, "An improved fractional slot concentrated winding for low-poles induction machines," in *2016 XXII International Conference on Electrical Machines (ICEM)*, 2016, pp. 114–119.

[65] V. M. Sundaram and H. A. Toliyat, "A fractional slot concentrated winding (fscw) configuration for outer rotor squirrel cage induction motors," in *2015 IEEE International Electric Machines Drives Conference (IEMDC)*, 2015, pp. 20–26.

[66] A. S. Abdel-Khalik and S. Ahmed, "Performance evaluation of a five-phase modular winding induction machine," *IEEE Transactions on Industrial Electronics*, vol. 59, no. 6, pp. 2654–2669, 2012.

[67] G. Rezazadeh, F. Tahami, G. A. Capolino, S. Vaschetto, Z. Nasiri-Gheidari, and H. Henao, "Improvement of concentrated winding layouts for six-phase squirrel cage induction motors," *IEEE Transactions on Energy Conversion*, vol. 35, no. 4, pp. 1727–1735, 2020.

[68] I. Boldea and S. Nasar, *The induction machine handbook. Boca Raton*. FL: CRC, 2002.

[69] J. Pyrhonen, T. Jokinen, and V. Hrabovcova, *Design of rotating electrical machines*. John Wiley & Sons, 2013.

[70] X. Liang and Y. Luy, "Harmonic analysis for induction motors," in *2006 Canadian Conference on Electrical and Computer Engineering*, 2006, pp. 172–177.

[71] X. Lu, K. L. V. Iyer, K. Mukherjee, K. Ramkumar, and N. C. Kar, "Investigation of permanent-magnet motor drives incorporating damper bars for electrified vehicles," *IEEE Transactions on Industrial Electronics*, vol. 62, no. 5, pp. 3234–3244, 2015.

Part 2

Study of Stator Winding Skin Effect Additional Losses in Synchronous Machines with Flat Turns, Open Slots and Arbitrary Rotor Geometry

2.1 Introduction

The efficiency of an electric machine is ultimately limited by the losses present in the stator windings. A proper copper loss estimation has an important role to allow a better choice of conductor size and winding layout to minimize the heating effect. Power dissipation in the stator winding of AC rotating machines is the sum of resistive DC Joule losses and additional losses caused by skin and proximity effects [1]. In low-voltage machines with semi-closed slots eddy currents accounting for additional losses are excited in stator conductors by slot leakage fluxes caused by armature currents, while rotor motion plays a minor or negligible role [2]. Conversely, large medium-voltage machines are usually equipped with form wound coils made of flat conductors embedded in open slots with rectangular cross section [3–7]. The use of flat conductors and open slots is spreading also in low-voltage machines equipped with the so-called hairpin windings [8]. In this case, flux lines can enter the slot from the air gap and sweep the conductors placed close to the slot opening so that significant eddy currents and increased additional losses arise in them, resulting in possible overheating and hot spots [4, 5]. The prediction of such kind of losses is challenging because rotor motion needs to be taken into account. This typically requires Time-Stepping Finite-Element Analysis (TSFEA) simulations where the detailed structure of each conductor needs to be considered [1], leading to significant computational burden and very complicated models. For simple rotor geometries, like that of surface permanent magnet machines, the problem can be solved analytically through the subdomain technique [9, 10] or through a set of THFEA simulations in which moving magnets are replaced by a grid of fictitious punctual conductors carrying sinusoidal currents with appropriate amplitude, frequency and phase [7]. For generic salient-pole rotor shapes, a computationally efficient alternative to TSFEA is proposed in [11] where a discrete flux density map in the slot domain is obtained through a sequence of magnetostatic finite-element analysis (MSFEA) simulations with different rotor positions and then used to compute induced eddy currents in each conductor analytically. The procedure is, however, specifically conceived for random-wound coils made of round wires and cannot directly apply to the case of form wound stators.

In this part, a very fast method to compute skin-effect additional losses in the stator winding of open-slot form-wound AC machines with arbitrary rotor geometry is proposed. The method is based on the idea of replacing the actual rotor by a static infinitely permeable ferromagnetic cylinder with a current sheet applied on its surface so as to produce the total air-gap revolving field of the real machine. Two simple MSFEA simulations, including only the detail of rotor geometry, are needed for the current sheet definition. The resulting model can be solved through a set of THFEA simulations at different frequencies to find skin-effect losses in stator conductors due to rotor motion. Finally, the solution of the whole THFEA model is shown equivalent to solving one small slice of it, if further current sheets are applied on the slice boundaries to account for the excluded parts. As a result, the application of the proposed technique to an example salient-pole synchronous generator shows that computation time can be abated from several hours (required by TSFEA) to a couple of minutes when the reduced model is adopted.

The technique being set forth in this part has some similarities with the Harmonic Balance Finite Element Method (HBFEM) [12–14], which however exhibits a significant complexity of implementation requiring dedicated numerical algorithms. The strength of the idea proposed in this part is in using the winding and permeance function theory [14] to reduce the machine model to a very simplified form which can be directly solved by commercially available software packages through conventional THFEA.

On the other side, a limit of the proposed method consists of assuming constant DC currents in rotor circuits and neglecting magnetic saturation. As to magnetic saturation, its impact on additional losses is discussed in detail through TSFEA showing that the assumption of unsaturated iron leads to conservative results, with an overestimation of the losses by around 15%, in the example machine considered as a case study. Moreover, for the sake of simplicity, this study, like [11], addresses only skin effect losses that arise in every single conductor, assuming that all strand in the coil are series-connected. The method can be however extended with relatively small effort to cover proximity losses due to circulating currents among several shunt-connected strands that may form a turn [1].

Part 2 is structured as follows: Section 2.2 addresses the description of the machine model and the study of the problem by TSFEA; Section 2.3 introduces the THFEA-based technique for the computation of additional losses in the stator strands; in Section 2.4 a reduced model aiming at speeding up the eddy current losses is presented. Sections 2.5 draws some conclusions from the previously presented investigations and results.

2.2 Description and study of the Problem by TSFEA

2.2.1 Description of the synchronous machine example

To illustrate the problem and the various possible approaches to its numerical study, the salient-pole machine shown in Figure 2.1 will be taken as an example. In addition to the dimensions shown in Fig. 1, the example machine is characterized by the data provided in Table 2.1. The machine is originally designed as a voltage-source inverter-fed motor for the oil and gas industry. The Field Oriented Control (FOC) allows for the motor to be operated at unity power factor in rating conditions. This study investigates the behavior of the machine for different possible design variants, in particular regarding the slot width. The stator slot and strand widths (w_s and w_c) are not fixed because two cases studies (corresponding to a wide-slot and a thin-slot design) as specified in Table 2.2 will be taken into account to highlight the strong impact of such parameters on skin-effect additional losses. For information, the rating data for the machine design with thin slots are provided in Table 2.3. Regarding the iron core, to investigate the effect of magnetic saturation, the two cases are addressed of a constant relative magnetic permeability equal to 10.000 and of a ferromagnetic material with the B-H curve shown in Figure 2.2.

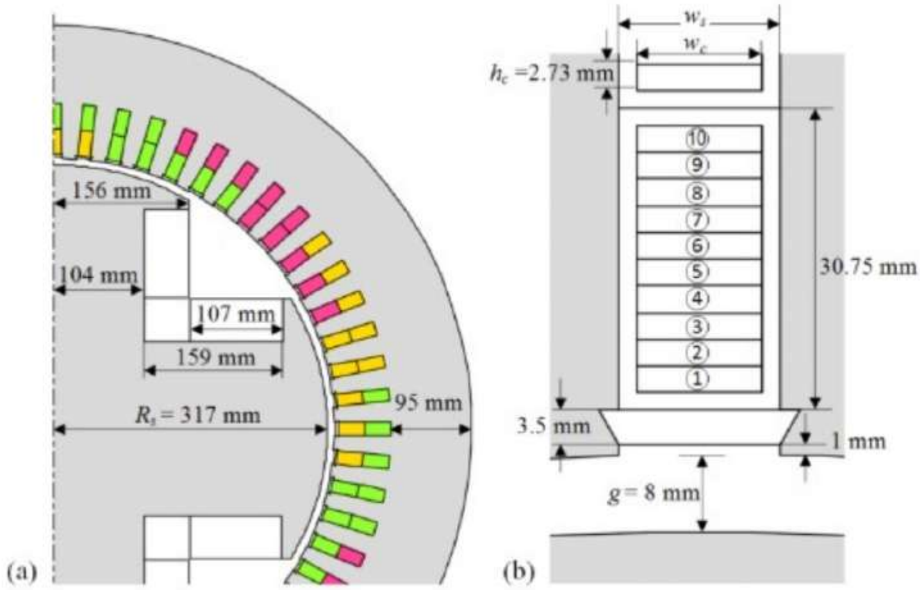

Figure 2.1: Cross-section and dimensions of **(a)** the machine under study; **(b)** the slot portion closer to the air gap.

Table 2.1: Example machine data.

Number of turns per coil	10	Number of pole, $2p$	4
Number of parallel paths per phase	2	Number of turns per phase in series	100
Number of turns per coil	10	Number of pole, $2p$	4
Number of slots	60	Core axial length	800 mm
Number of field turns per pole	100	Coil to pole pitch ratio	0.8
Number of phases	3	Phase connection	Y

Table 2.2: Investigated design variants.

	w_s	w_c
Wide slot design	16.0 mm	12.5 mm
Thin slot design	13.2 mm	8.7 mm

Table 2.3: Example machine ratings.

	Wide slot design	Thin slot design
Rated line-to-line voltage	6000 V	6000 V
Rated line current	190 A	190 A
Rated frequency	60 Hz	60 Hz
Rated power factor	1	1
Rated efficiency	97.6 %	97.7 %
No-load field current	50 A	49 A

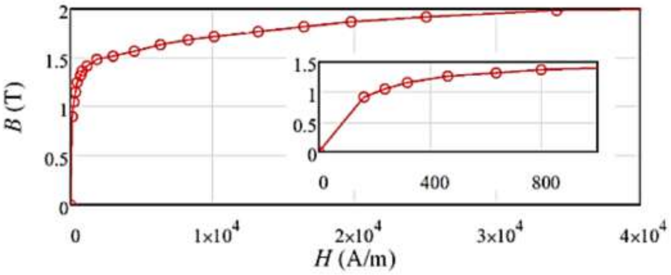

Figure 2.2: Core B-H curve considered for the ferromagnetic material of the saturated model.

2.2.2 Modeling and analysis of the machine by TSFEA

The most complete and accurate way to study and illustrate stator additional losses due to the air-gap flux lines entering the slots is TSFEA. This implies an accurate modeling of the machine geometry over time; the model needs to include both the details of the winding structure (Figure 2.1) and rotor motion [1].

For illustration purposes, the TSFEA is applied to the example machine which is supposed to operate as a generator both at no load and feeding a three-phase resistive load, in the working conditions illustrated in Figure 2.3. The phase voltage and currents E_{ph} and I_{ph} are selected so as to give the same fundamental airgap flux-density amplitude around 0.7 T in all cases and a current density around 4 A/mm^2 in stator conductors. The simulations are performed for both the wide and thin slot design (Table 2.2) as well as with linear and saturable core iron.

In the TSFEA, the fixed 1800 r/min speed is applied to the rotor and the field current is adjusted so as to obtain the indicated phase current and voltage values in all the simulated scenarios. The simulation time must be enough for the machine to reach the steady-state conditions in terms of currents, voltages and losses.

Figure 2.4 shows the flux lines and eddy-current distribution in a stator coil side placed in the slot region close to the air gap for the unsaturated machine with large-slot design. It can be seen how some flux lines from the air gap enter the slot changing their spatial distribution over time

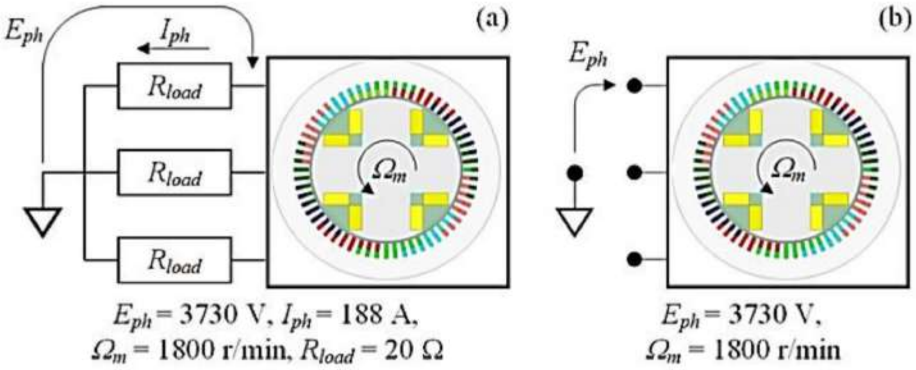

Figure 2.3: Operating conditions reproduced by TSFEA (a) on load and (b) at no load. Phase voltage and current (E_{ph} and I_{ph}) are expressed in RMS.

due to the revolving air-gap field. As an effect significant eddy currents arise especially in those conductors which are placed nearest the air-gap.

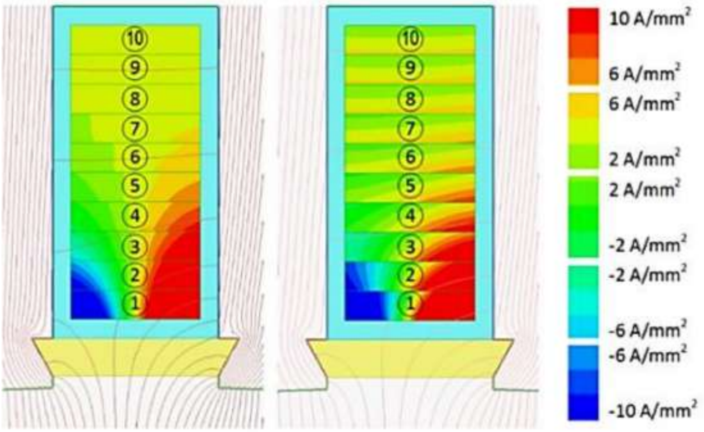

Figure 2.4: Detail of eddy current density and flux lines distribution at two different time instants for a stator coil side placed in the slot region close to the air gap. The interval between the two time instants corresponds to a rotor angular displacement of 12.8 mechanical degrees.

Figure 2.5 shows the variation of total resistive losses in each of the ten conductors in the coil as a function of time, once the machine has reached the steady state. Although the losses of all the ten conductors are plotted, only those occurring in the three strands placed closest to the air gap are visible.

Heating is due to the mean value of the losses. Therefore, in post processing TSFEA results, the average power dissipated in each conductor needs to be computed by integrating instantaneous power (Figure 2.5) over one electrical period. The mean Joule losses for the ten conductors of a coil are shown in Figure 2.6.

As expected [1, 2, 4–9], additional losses are very large in conductor #1, which is the most exposed to air-gap flux lines entering the slot (Figure 2.4), and decrease in the other conductors as their distance from the air gap grows. We can also observe that the losses at no load are much lower

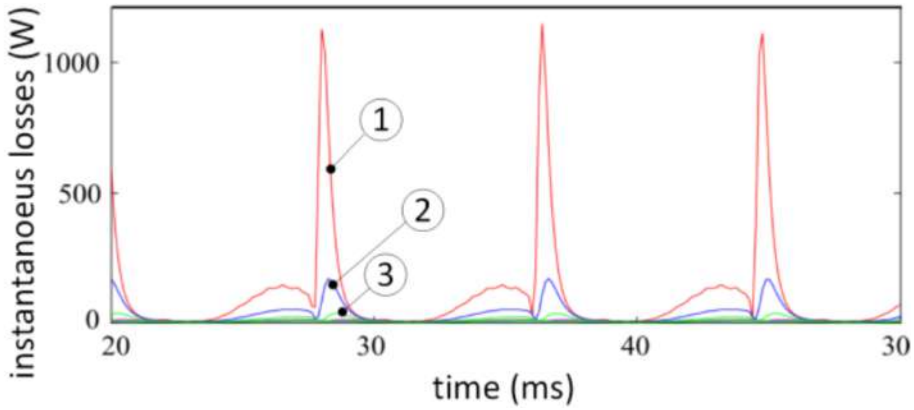

Figure 2.5: Losses versus time at steady-state for the stator of a coil side placed the closest to the air gap.

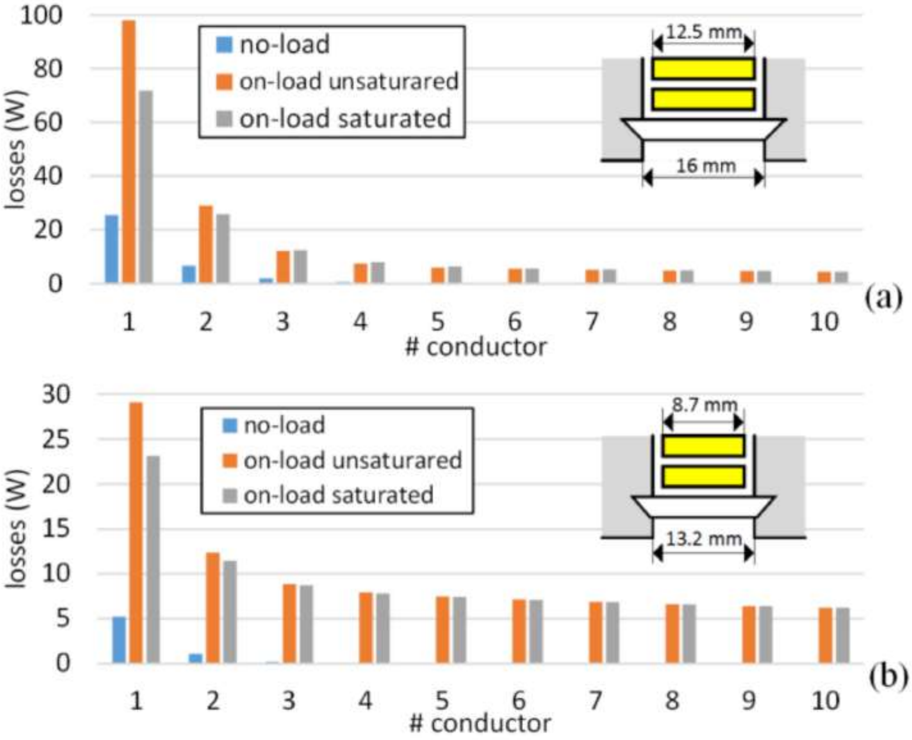

Figure 2.6: Resistive losses in the ten conductors placed nearest the air gap as obtained from TSFEA for the machine design with (a) wide slots and (b) thin slots.

than those in loaded conditions and that magnetic saturation tends to reduce them significantly, especially in conductor #1 (no-load simulation results are shown only for the linear case for the sake of brevity, since the effect of saturation is the same as on load). Finally, what evidently emerges is the strong impact of slot and conductor width: for the wide slot design the additional losses in conductor 1 are more than four times as much as in the thin-slot design.

The observations made commenting on Figure 2.6 can be in large part explained considering the air-gap flux-density waveforms in the various cases under study. These are shown in Figure 2.7 with relevant space harmonic spectra reported in Figure 2.8.

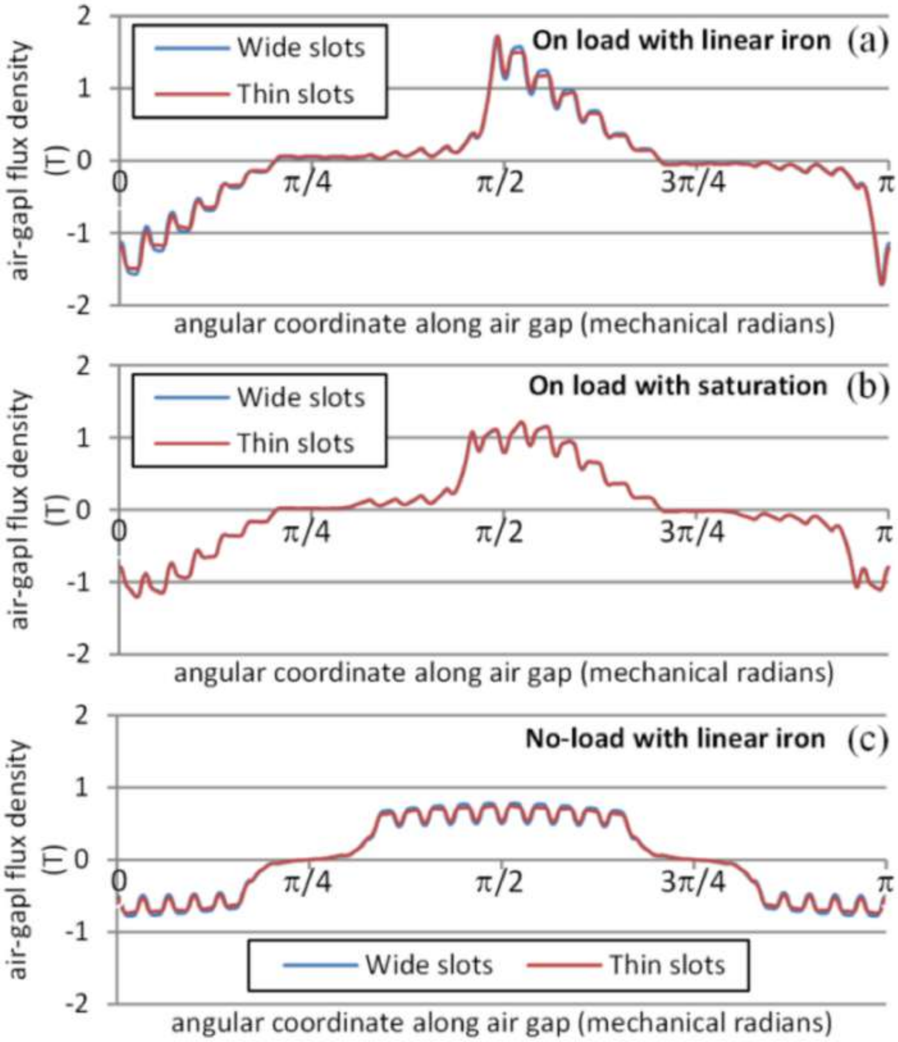

Figure 2.7: Radial component of the air-gap flux density (a) at full load with linear iron; (b) at full load with saturated iron; (c) at no load with linear iron.

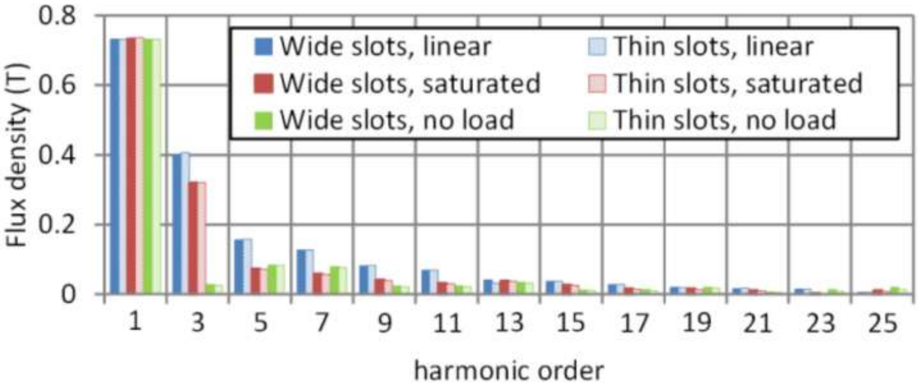

Figure 2.8: Air-gap flux-density space harmonics in various simulated scenarios.

Figure 2.8 highlights that, although the fundamental flux-density amplitudes are aligned in all cases, the content in higher-order space harmonics significantly changes from no-load to loaded operation depending on whether magnetic saturation is taken into account or not.

In particular, from Figure 2.8 it can be seen that the full-load operation with linear iron is the condition where the largest space harmonics appear while magnetic saturation produces a higher order space harmonic reduction. This can appear counter-intuitive as magnetic saturation is often thought of as a source for magnetic field distortion. Actually, the air-gap magnetic field distortion in the salient-pole machine under study is mainly produced by rotor anisotropy, which causes a steep variation in field intensity (Figure 2.7-(a)) across pole shoe ends. When magnetic saturation is taken into account, flux density peaks are obviously reduced and the overall air-gap flux-density waveforms is clearly flattened as it can be seen by comparing Figure 2.7-(a) and Figure 2.7-(b). Such "flattening effect" naturally leads the air-gap flux density waveform to better approximate an ideal sinusoidal shape and, therefore, causes a reduction in its higher-order space harmonics as visible from Figue 2.8. For the sake of clarity, it may be worth emphasizing that the presence or absence of magnetic saturation does not refer to different operating conditions, but depends on how the machine model (operated in the same working point) is modelled, i.e. either assuming a non-linear B-H characteristic for ferromagnetic cores (Figure 2.2), or assigning them a constant magnetic permeability.

Regarding the effect of load, we can observe that at no-load conditions the harmonic spectrum appears to be almost the same as in the on-load saturated case, except for the 3^{rd} harmonic which nearly reduces to zero and will be shown to have a strong impact of additional losses in what follows. Since air-gap field space harmonics are known to noticeably affect the additional losses in issue [7], it is reasonable that the largest the space harmonic content, the highest the additional losses (Figure 2.6).

On the other side, slot and conductor width effect cannot be justified looking at air-gap field waveforms (Figure 2.7), which are almost the same for both large and thin slots. An explanation can be given observing that, as clearly visible from Figure 2.4, eddy currents in the strands near the air gap concentrate on the left and right ends of conductors, with opposite direction on the two sides. This is schematically sketched in Figure 2.9-(a), where eddy currents are assumed to concentrate in points $P1$ and $P2$, and $\Phi_{gap}(t)$ denotes the average air-gap flux flowing between them. For each air-gap harmonic, $\Phi_{gap}(t)$ varies sinusoidally over time with a frequency depending on the harmonic's order and speed.

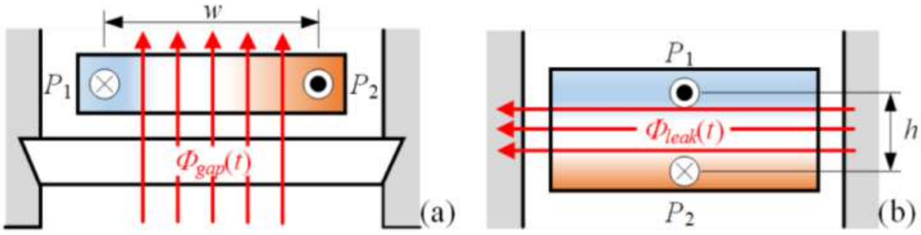

Figure 2.9: Schematic representation of a single conductor in a slot crossed by flux lines (a) from the air gap and (b) due to slot leakage flux.

Eddy currents are excited in the fictitious turn of sides $P1$ and $P2$ according to Faraday-Lentz's law by the time variation of $\Phi_{gap}(t)$. It appears that the wider the turn width w the larger the flux linkage and, hence, the electro-motive force (EMF) acting as eddy-current source. More rigorously, the phenomenon could be treated in the same way as the skin effect caused by the slot leakage flux $\Phi_{leak}(t)$ crossing conductors in the orthogonal direction (Figure 2.9-(b)). It is well-known that the height h strongly impacts on the skin effect in such case [15]. By analogy, this explains how skin-effect losses caused by air-gap lines entering the slot are found to be highly sensitive to slot and conductor width (Figure 2.6).

As could be clearly understood from this work, the assumption considering each turn composed of one single conductor is made to exclude the occurrence of proximity losses so that only extra losses due to air-gap leakage fluxes entering the slot and "sweeping" the conductors are taken into account. However, to anticipate some results which include the possibility of having multiple parallel-connectors in each turns, the winding configurations summarized in Figure 2.10 are explored through TSFEA simulations.

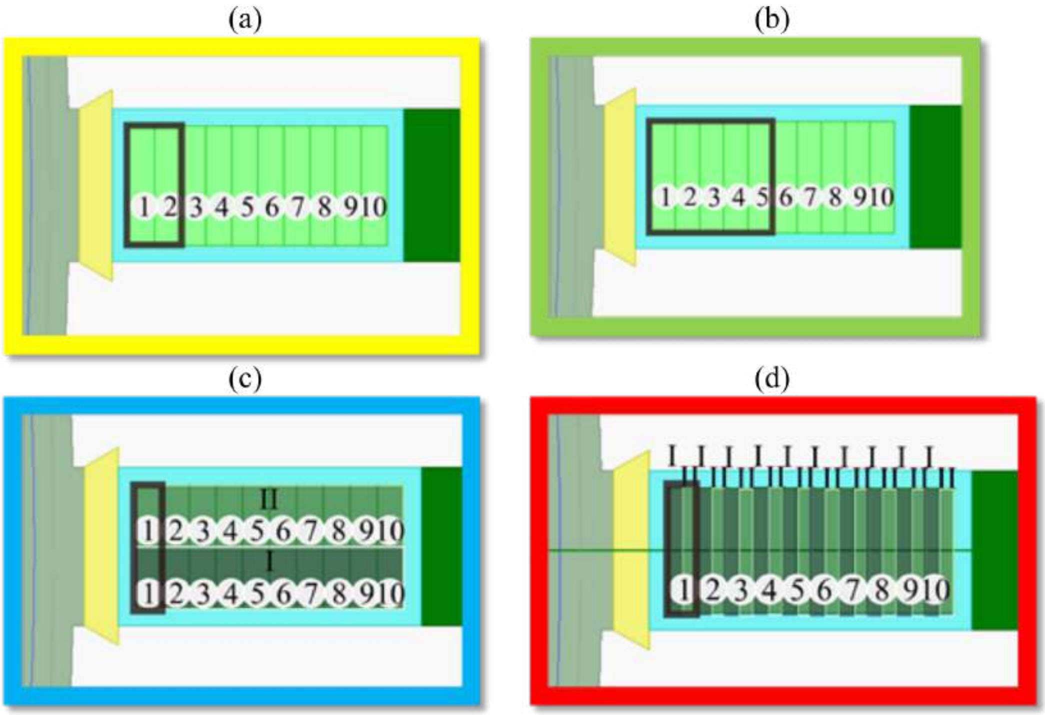

Figure 2.10: Winding configurations considered for the comparative evaluation of extra losses: (a) two strands in parallel per turn, 5 turns in series per coil; (b) five strands in parallel per turn, 2 turns in series per coil; (c) two strands in parallel per turn (one strand aside the other), 10 turns in series per coil and (d) Two strands in parallel per turn (one strand above the other), 10 turns in series per coil. The rectangle with black border embraces the strands which are connected in parallel to form a single turn.

In all the cases, the number of parallel ways per phases or the machine rated voltage and current have been adjusted to have the same current density (i.e. electrical loading). Furthermore, the size of the slot has maintained the same (corresponding to the "wide slot" design variant) as well as the armature reaction field. Simulations are all run at unity power factor, rated current and rated voltage, hence with equal flux density in the air gap and equal current density in conductors. This allows for a homogeneous comparison in terms of extra losses. The results of the total losses in the four explored situations are shown in Figure 2.11 (please note that the first white bar refers to the situation already discussed previously, where all conductors in a coil are assumed to be series connected). It is worth noticing that, for those winding configurations characterized by multiple parallel-connected strands per turn, not only skin effect is considered but also proximity losses are included.

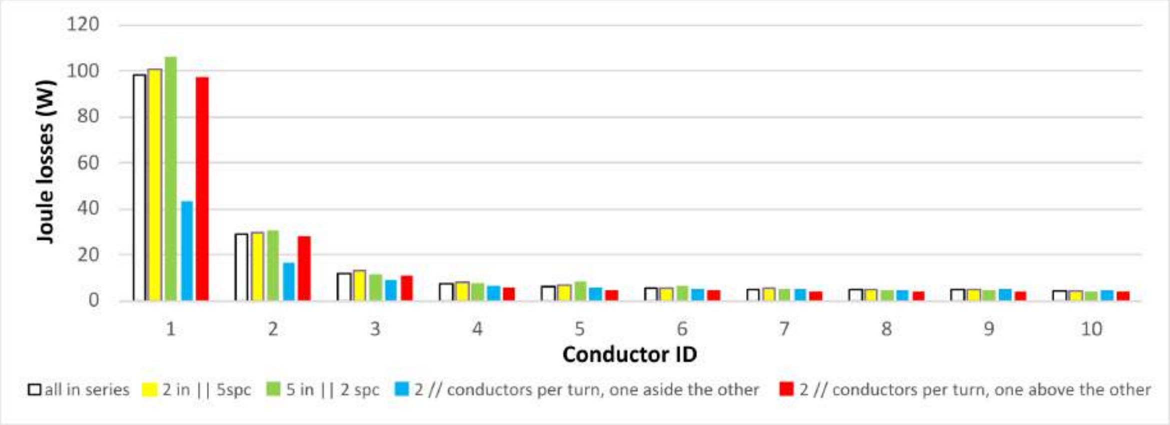

Figure 2.11: Joule losses per conductor for different winding configurations.

What clearly emerges from the comparison is that there are not significant changes in the extra losses except for the winding configuration with two parallel connected strands per turn, placed one aside the other (blue bars). This result is not surprising as it is fully consistent with the explanation given in Figure 2.9 regarding the origin of extra losses due to air-gap leakage fluxes entering the air gap: according to such explanation the larger the conductor, the larger the extra losses arising in it. Therefore, it can be expected that in the winding configuration with two parallel strands per turn placed one aside the other the extra losses are significantly reduced because the single conductor width is reduced to one half.

From the investigations conducted on different winding arrangements, it has been also noticed that proximity losses have a minor impact if compared to skin effect losses due to fluxes entering slots from the air gap. This was observed noticing that the circulating currents between parallel-connected strands per turn are very small.

The results of TSFEA simulation discussed in this Section highlight the importance of predicting skin-effect additional losses when designing form-wound machines with open slots, especially to avoid design choices (e.g. slot and conductor width) expected to cause local overheating, as will be better illustrated by the thermal analysis reported in the following Section 2.2.3.

2.2.3 Thermal analysis

Large skin-effect phenomena occurring in stator conductors placed near the air gap can be harmful not so much in terms of efficiency but as sources for overheating and hot spots. This is better illustrated in this section through a combined thermal and fluid-dynamic 3-dimensional (3D) FEA simulation of the synchronous machine example under study. The machine design with wide slots (Table 2.2), where extra losses are higher and expected to produce larger thermal issues are considered as a case study.

The type of cooling is $IC611$, which means that the totally enclosed machine is equipped with an air-to-air heat exchanger mounted on the top of the frame as illustrated in Figure 2.12. Forced circulation through shaft-mounted fans is applied to both primary cooling air (which is directly in contact with active parts) and secondary cooling air (which flows through the heat exchanger pipes). The internal cooling air flow inside the machine is sketched in Figure 2.13. The fresh cooling air (C) enters the machine frame from the heat exchanger at both ends, drawn by shaft-mounted fans (F). It then enters the air gap and returns to the heat exchanger by flowing through radial ventilation ducts. Radial ventilation ducts are obtained by subdividing the stator core into several elementary stacks (S), as shown in the example picture in Figure 2.14.

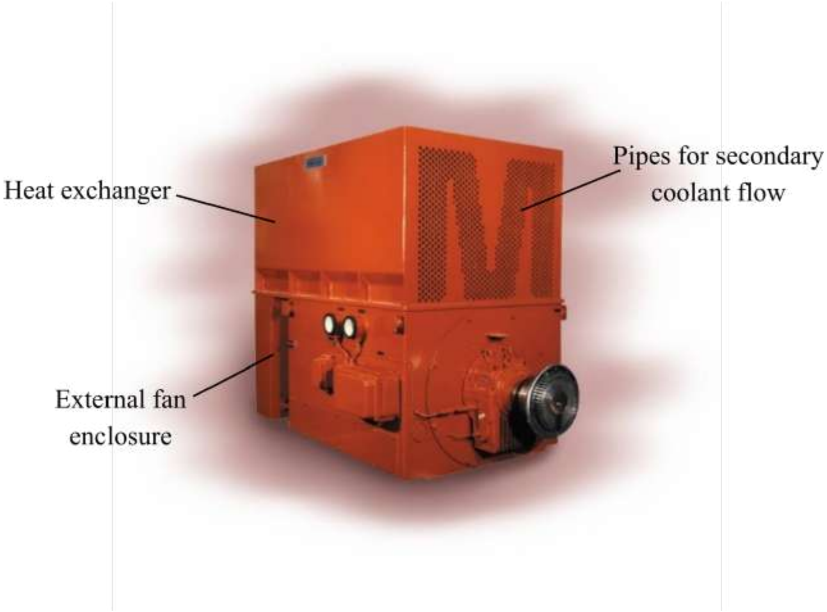

Figure 2.12: Example of a medium-voltage rotating machine with $IC611$ cooling system. The machine is totally enclosed and equipped with an air-to-air heat exchanged mounted on its top. Forced circulation through shaft mounted fans is used for both primary and secondary cooling air.

Given the cooling system depicted in Figure 2.13, it is clear that a 2D thermal simulation would not suffice because the heat flows are not only in radial and tangential direction, but also in the axial direction. In order to reduce the computational burden symmetries can be exploited and the portion of the machine shown in Figure 2.15 can be modelled.

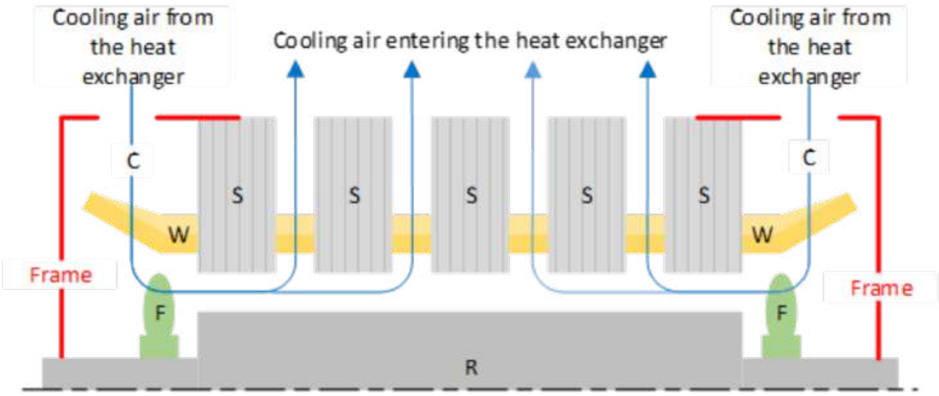

Figure 2.13: Cooling system schematic. The cooling air flow (C) enters the machine frame at both ends from the heat exchanger, drawn by shaft-mounted fans (F). It then enters the air gap radially and returns to the heat exchanger by flowing through radial ventilation ducts obtained by subdividing the stator core into elementary laminated stacks (S).

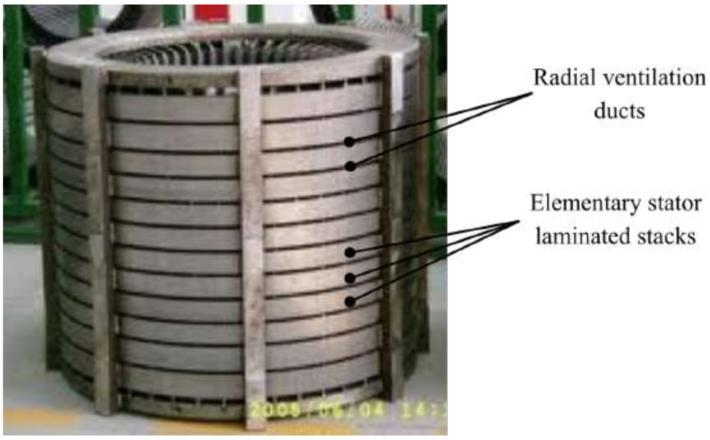

Figure 2.14: Example of a medium-voltage machine stator equipped with radial ventilation ducts.

The elementary laminated stack placed in the middle of the stator core is taken into account for the estimation to be conservative as the temperature tends to increase as we move from the ends of the core (in contact with “fresh air”) to the center. The modelled portion of the machine is delimited by cutting planes $\Pi1$, $\Pi2$, $\Pi3$ and $\Pi4$ across which no heat and no cooling air can flow due to symmetry reasons. We notice that cutting planes $\Pi1$, $\Pi2$ are displaced by a slot pitch angle apart while cutting planes $\Pi3$, $\Pi4$ are orthogonal to the machine rotational axis and placed in the middle of two successive radial cooling ducts.

The 3D model used for the simulation is shown in Figure 2.16. For its solution, the losses computed in stator conductors by TSFEA in full-load conditions are assigned as heating sources in the coils together with a specific core loss of 9.2 W/kg in the stator ferromagnetic region. The cooling air is imposed to enter the radial ventilation ducts with a typical speed of 20 m/s [16] and with a temperature of 20°C.

The thermal conductivity of materials is set using standard values in the ranges provided in [17]. The results of the combined thermal and fluid-dynamics simulations are shown in Figure 2.17

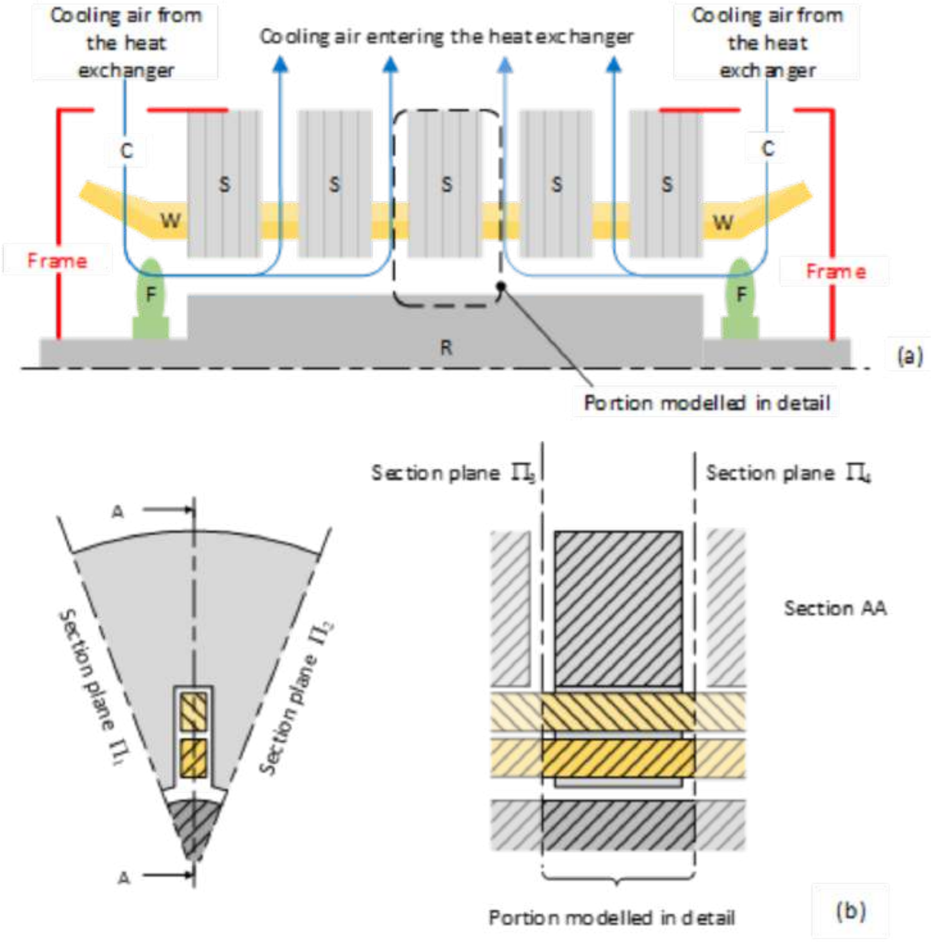

Figure 2.15: (a) Axial section schematic showing the cooling air flow: **S**-stator elementary stack between cooling ducts; **W**-stator winding coil; **R**-rotor; **F**-shaft-mounted fans; **C**-cooling air path. (b) Portion of the machine considered for the 3D thermal simulation.

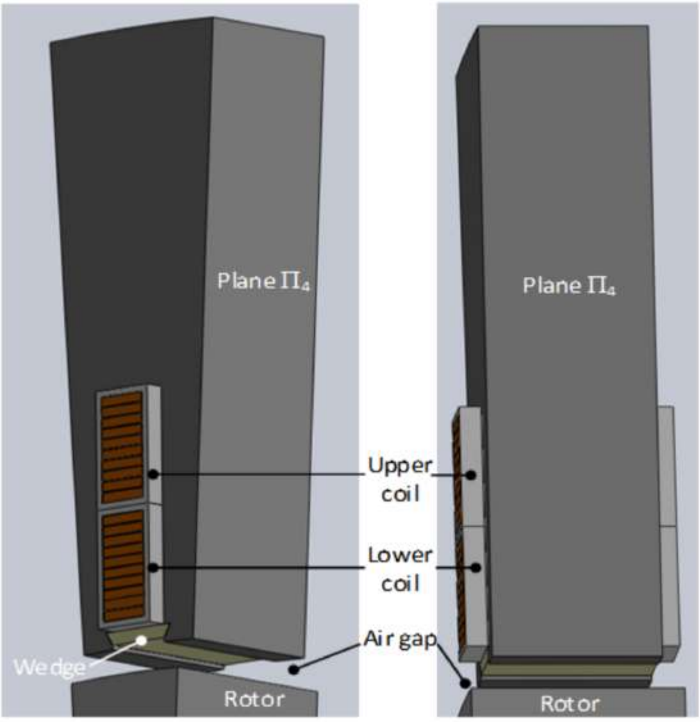

Figure 2.16: Two views of the machine model portion used for 3D thermal FEA.

in terms of velocity distribution of the air inside the radial cooling ducts.

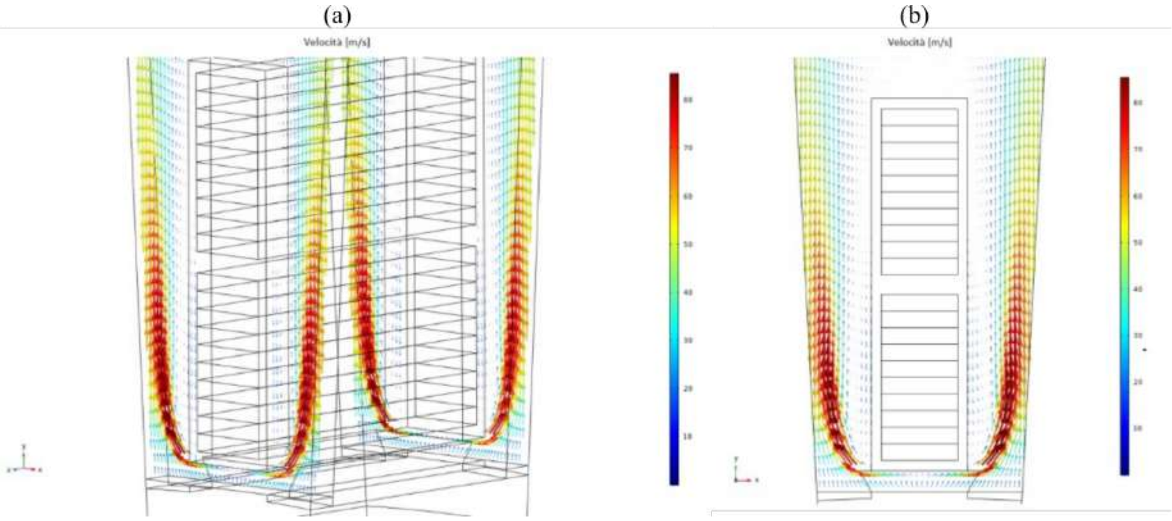

Figure 2.17: Cooling air velocity field (speed in m/s) in the radial cooling duct as resulting from 3D fluid-dynamic simulation assuming an air speed of 20 m/s on the air-gap side.

It can be seen from Figure 2.17 that - as expected - the cooling air flow is not laminar everywhere and some turbulence occurs in the cooling duct regions near the bottom and sides of the coils. This causes the air speed to locally take very high values, with beneficial effects on the heat removal.

Simulation results in terms of temperature field are shown in Figure 2.18 and 2.19. In particular Figure 2.18-(a) shows the temperature of the whole modelled system (including the cooling duct portions on both sides). It can be seen that the iron core temperature is between 30 and 40°C, while the strand copper exhibits temperatures which range from around 45°C to around 130°C. The hottest strand is – as expected – the one closest to the air gap, where the majority of Joule losses occur due to severe skin effect. As the distance from the air gap increases, the strand temperature reduces, which reflects the reduction in the extra losses caused by flux lines entering the slot from the air gap. Hot spots are very dangerous due to the damage they can cause to the insulation system.

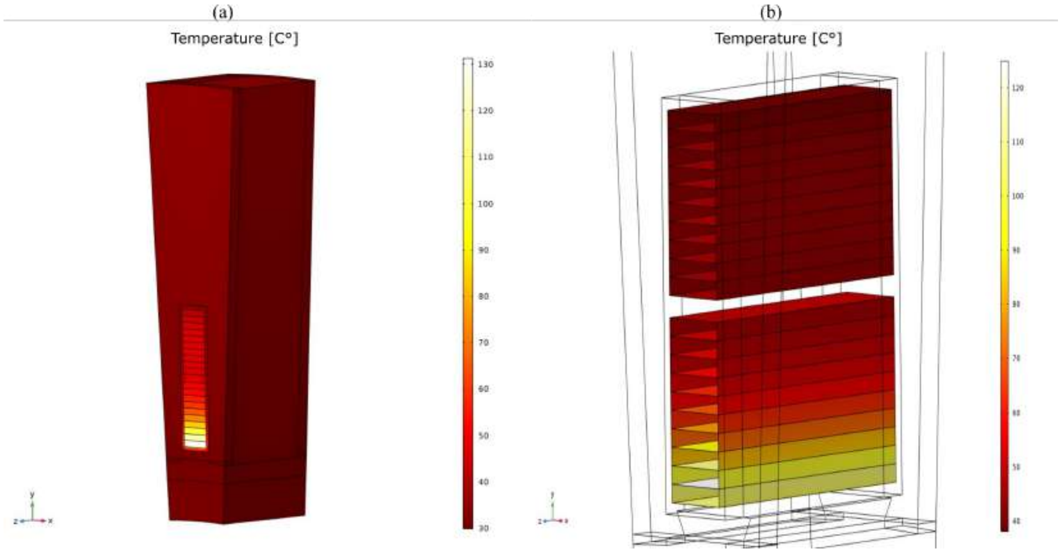

Figure 2.18: Temperature distribution in (a) the solved model and (b) the conductor insulation.

For this reason, it makes sense to investigate the temperature of the insulating varnish covering the strands, as this is the dielectric material subjected to the highest thermal stress. Such temperature distribution is shown in Figure 2.18-(b), which confirms that the temperature range is between 40 and 130 °C, with the highest temperature occurring in the insulating varnish between the first and the second strand on the air-gap side. This high thermal stress is expected to damage the insulation over time until a breakdown occurs resulting in a short circuit between the first and the second strand (turn fault). As a consequence of the fault current induced in the shorted turns the local temperature further increases normally leading to a damage and final breakdown of the ground wall insulation and a consequent phase-to-ground fault.

Finally, Figure 2.19 gives a further illustration of the temperature distribution on a radial cutting plane placed on the symmetry axis of the slot.

It is worth noticing that the temperatures resulting from the thermal and fluid-dynamic FEA are not very significant in terms of absolute values as the absolute value raises more or less proportionally to the temperature of the cooling air. What is more meaningful is the temperature difference inside the winding. From this point of view, we can observe that the difference in temperature between the strands on the two opposite ends of the slot is around 90 K, which clearly indicates the presence of "hot spots" in the conductors (and relevant insulation) placed near the air gap. Hot spots are potentially harmful because they can damage the insulation over time causing its breakdown and a consequent turn-to-turn fault.

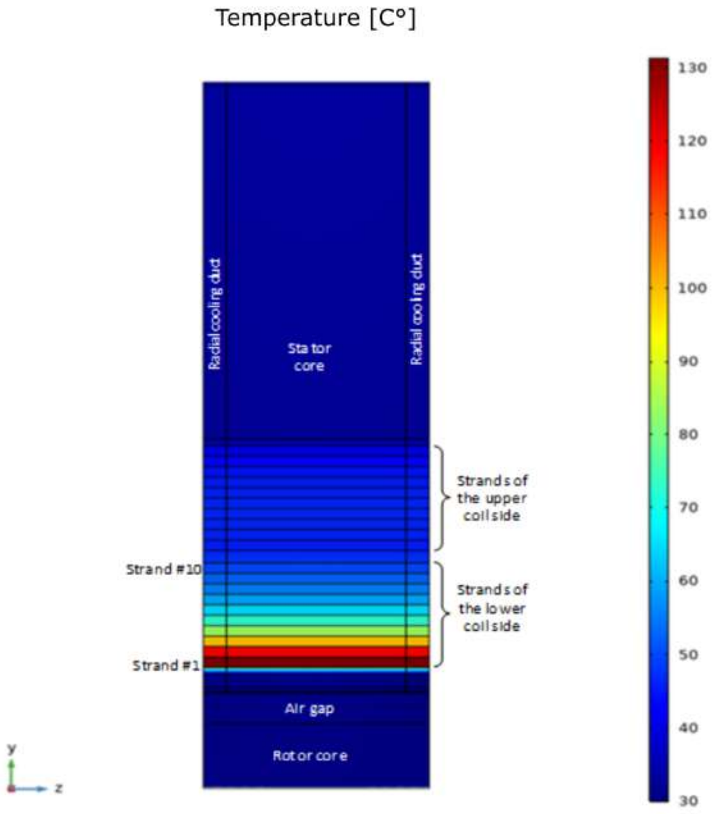

Figure 2.19: Temperature distribution in a model cross section.

2.3 Additional loss computation through THFEA

In order to overcome the shortcomings of TSFEA related to computational burden and model complexity, the following of this part will illustrate much faster simulation approaches based on MSFEA and THFEA which do not need to include rotor motion effects. As a first step in this direction, an efficient method to compute the radial airgap field space harmonic spectrum for a generic salient-pole rotor geometry is illustrated in this section. For that, the air-gap magnetic field need to be adequately determined.

2.3.1 Magnetic field space harmonic computation

The air-gap radial magnetic field can be computed through purely analytical methods for round rotor synchronous machines [9, 10]. For a generic salient-pole rotor structure, instead, a fully analytical method is not presently available from the literature and the need arises to run a minimal set of MSFEA simulations [14]. The hypotheses made in this Section to determine air-gap magnetic field harmonics for a salient-pole machine with generic rotor shape consist of neglecting magnetic saturation and stator slotting effect. The former assumption is actually a limitation of the method, while the latter is not restrictive as the slotting effect will be subsequently considered in the simplified models for THFEA.

As illustrated in Figure 2.20, we shall assume phase a-axis as a reference for a polar coordinate system (ρ, θ) and indicate θ_r the rotor d-axis position. The currents in stator phases a, b and c are assumed to have amplitude I_s and angular frequency ω:

$$\begin{aligned} i_a(t) &= I_s \cos(\omega t) \\ i_b(t) &= I_s \cos(\omega t - \frac{2\pi}{3}) \\ i_c(t) &= I_s \cos(\omega t - \frac{4\pi}{3}) \end{aligned} \tag{2.1}$$

while the field circuit is supposed to carry a constant current I_f. A mean air-gap circumference Γ is introduced having radius $R_m = R_s - g/2$ where R_s is the stator bore radius and g the minimum air-gap width.

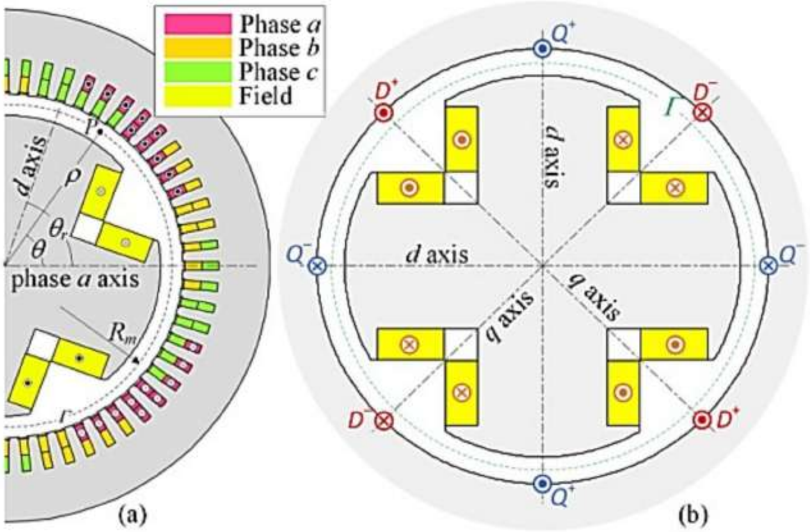

Figure 2.20: (a) Polar coordinate system and reference axes; (b) simplified slotless model for MSFEA (air-gap width is magnified for illustration purposes).

The simplified machine model shown in Figure 2.20 is reproduced for MSFEA. It includes the actual rotor geometry and a slotless stator with fictitious punctual conductors D^+, D^-, Q^+ and Q^- located where the smooth stator bore circumference intersects rotor d and q axes. If - for the time being - we neglect slotting effects, the radial magnetic field along circumference Γ at the angular position θ and time t can be expressed as [14]:

$$H_{gap}(\theta, t) = \mathcal{P}_{rot}(\theta - \theta_r)\mathcal{M}(\theta, t) + \mathcal{H}_{rot}(\theta - \theta_r)\frac{I_f}{I_{f0}} \tag{2.2}$$

where $\mathcal{P}_{rot}$ denotes the rotor permeance function, $\mathcal{M}$ the stator MMF, $\mathcal{H}_{rot}$ the radial magnetic field due to a generic rotor field current I_{f0} taken as a reference and I_f the actual field current.

The stator MMF for a symmetrical three-phase distributed winding is given by (2.3) being N_s the number of series-connected turns per phase, p the number of pole pairs and $k_{w,|6k+1|}$ the winding factor for the space harmonic of order $|6k+1|$ [18].

$$\mathcal{M}(\theta,t) = \sum_{k\in\mathbb{Z}} M_k \cos\left[p(6k+1)\theta - \omega t\right], \qquad M_k = \frac{3}{\pi} I_s \frac{N_s}{p} \frac{k_{k,|6k+1|}}{|6k+1|} \tag{2.3}$$

Regarding rotor permeance function, it can be expressed as:

$$\mathcal{P}(\theta-\theta_r) = g^{-1} p_{rot}(\theta-\theta_r) = g^{-1} \sum_{n=0,1,2,..} P_n \cos\left[2np(\theta-\theta_r)\right] \tag{2.4}$$

where p_{rot} denotes the relative permeance function (varying between 0 and 1) referred to the minimum air-gap width g and P_n are its Fourier series coefficients. For a generic salient-pole rotor geometry there is no analytical expression for p_{rot}. To identify this function according to [14], two MSFEA simulations are run on the model in Figure 2.20-(b), where conductor pairs (D^+, D^-) and (Q^+, Q^-) are respectively energized. Based on the radial component of the magnetic field computed along Γ from the two simulations, the rotor relative permeance function and relevant Fourier coefficients shown in Figure 2.21-(a) are found.

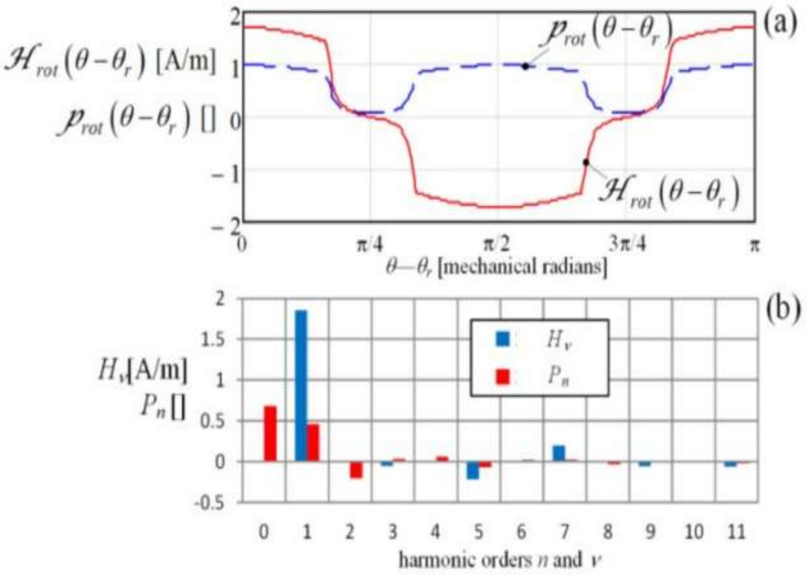

Figure 2.21: (a) Functions $\mathcal{H}_{rot}$ and p_{rot} and (b) relevant Fourier series coefficients, for a reference field current $I_{f0} = 100$ A.

Finally, the rotor air-gap field contribution $\mathcal{H}_{rot}$ for the reference field current I_{f0} is:

$$\mathcal{H}_{rot}(\theta-\theta_r) = \sum_{\nu=1,3,5..} H_\nu \cos\left[\nu p(\theta-\theta_r)\right] \tag{2.5}$$

As observed for p_{rot}, there is no general analytical expression for $\mathcal{H}_{rot}$. To identify this function, the model shown in Figure 2.20-(b) is used energizing the field circuit with the (arbitrary) current I_{f0} and extracting the magnetic field radial component along Γ. The resulting waveforms and Fourier coefficients are shown in Figure 2.21-(b) for the example case where the field current is $I_{f0} = 100$ A.

In steady-state synchronous operation, the rotor revolves at the synchronous mechanical speed ω/p and it position θ_r is given by (2.6) being θ_{r0} the d-axis position at $t = 0$.

$$\theta_r(t) = \frac{\omega}{p}t + \theta_{r0} \tag{2.6}$$

By plugging (2.3), (2.4), and (2.5) into (2.2) and taking (2.6) into account, after some algebraic manipulations, the following final expression is obtained for the radial magnetic field in steady-state synchronous operation:

$$H_{gap}(\theta, t) = \mathcal{R}e\left[\overline{H}_{gap}(\theta, t)\right] \tag{2.7}$$

$$\overline{H}_{gap}(\theta, t) = \sum_{\nu=1,2,3..}\left\{\overline{E}_\nu e^{i(\nu\omega t - \nu p\theta)}\frac{I_f}{I_{f0}} + \sum_{k\in\mathbb{Z}, q\in\{-1,1\}}\left[\overline{F}_{\nu,k,q}e^{i[\nu\omega t - (6qk+\nu)p\theta]}\right]\right\} \tag{2.8}$$

where overlined symbols indicate complex quantities and the harmonic coefficients $\overline{E}_\nu$, $\overline{F}_{\nu,k,q}$:

$$\overline{E}_\nu = H_\nu\frac{I_f}{I_{f0}}e^{i\nu p\theta_{r0}}, \quad \overline{F}_{\nu,k,q} = \frac{M_k(1+\delta_{\nu,1})P_{(\nu-q)/2}}{2g}e^{i(\nu-q)p\theta_{r0}} \tag{2.9}$$

The symbol $\delta_{\nu,1}$ in (2.9) is the Kronecker delta, which is equal to one if $\nu = 1$ and zero otherwise. For the rest of the Section, the magnetic field space harmonics will be written using the complex-valued expression (2.8) as often done in the literature, keeping in mind that the actual magnetic field corresponds to the real part of (2.8).

As an intermediate validation example, (2.7) and (2.8) are applied to compute the radial magnetic field at $t = 0$, with a peak stator current $I_s = 266$ A, a field current $I_f = 110$ A and an initial rotor position $\theta_{r0} = 69.2$ mechanical degrees for the example machine. The waveforms obtained analytically and by TSFEA are compared in Figure 2.22-(a) showing a good agreement except for slotting effects, and the relevant flux density space harmonics appearing in (2.8) are given in Figure 2.22-(b).

Equation (2.8) expresses the air-gap magnetic field as the sum of travelling waves with νp and $|6qk + \nu|p$ pole pairs, in a form that will be convenient for THFEA as explained next.

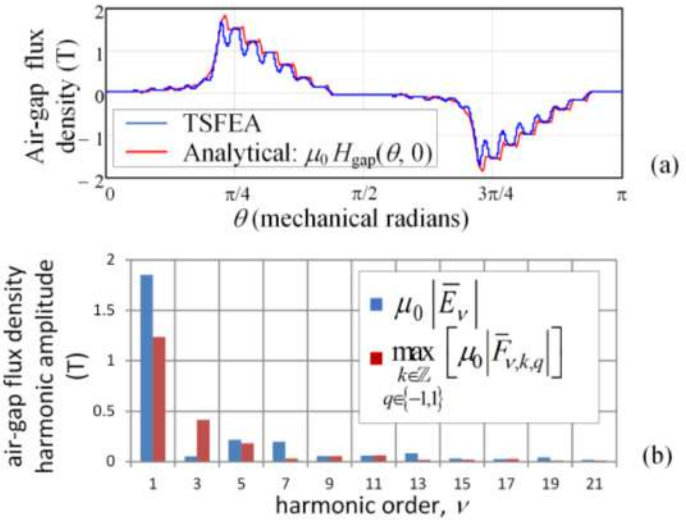

Figure 2.22: (a) Radial component of the air-gap flux density from TSFEA and from analytical calculation. (b) Analytically computed flux density harmonics.

2.3.2 Simplified machine model used for the THFEA

As a fast alternative to TSFEA, let us introduce a machine model where the real rotor is replaced by a static infinitely permeable non-conductive ferromagnetic cylinder with uniform air gap g and radius$R_r = R_s - g$, as shown in Figure 2.23. The rotor is at stand-still and all the slots of the model are empty except for one which includes the details of conductors, with no current impressed.

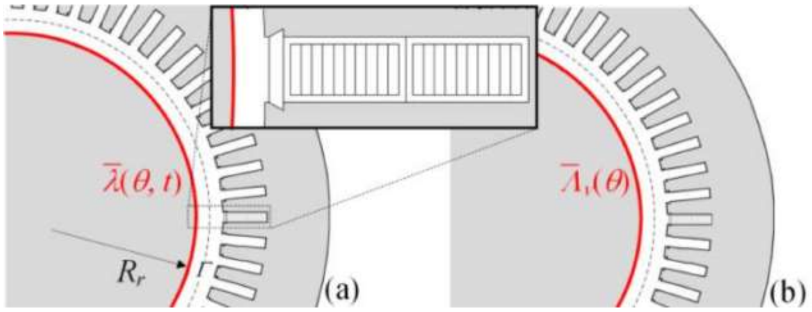

Figure 2.23: (a) Round-rotor model with fictitious linear current density spread on rotor surface; (b) THFEA model for the ν^{th} harmonic at frequency $\nu\omega$.

The air-gap magnetic field along the mean air-gap circumference Γ is imposed to be the same as that computed through (2.8) for the real machine. To this end, the following current density $\overline{\lambda}(\theta, t)$ is spread around the cylinder surface [6]:

$$\overline{\lambda}(\theta, t) = -\frac{g}{R_r}\frac{\partial \overline{H}_{gap}(\theta, t)}{\partial \theta} \tag{2.10}$$

By substitution of (2.8)-(2.9) into (2.10), the equivalent current density can be expressed as:

$$\overline{\lambda}(\theta,t)=\sum_{\nu=1,3,5}e^{i\nu\omega t}\overline{\Lambda}_{\nu}(\theta) \tag{2.11}$$

where

$$\overline{\Lambda}_{\nu}(\theta)=\overline{E'}_{\nu}e^{-i\nu p\theta}+\sum_{k\in\mathbb{Z},q\in\{-1,1\}}\overline{F'}_{\nu,k,q}e^{-i(6qk+\nu)p\theta} \tag{2.12}$$

$$\overline{E'}_{\nu}=i\frac{g\nu pH_{\nu}}{R_r}\frac{I_f}{I_{f0}}e^{i\nu p\theta_{r0}},\qquad \overline{F'}_{\nu,k,q}=i\frac{M_k p(6qk+\nu)(1+\delta_{\nu,1})P_{(\nu-q)/2}}{2R_r}e^{i(\nu-q)p\theta_{r0}} \tag{2.13}$$

Expression (2.11) is useful because it demonstrates that, thanks to the superposition principle, it is possible to approach the loss computation problem through a set of THFEA simulations, one for each harmonic order ν corresponding to an air-gap flux density wave of significant amplitude (Figure 2.22). In fact, let us consider a generic harmonic order ν. The additional losses P_{ν} associated with it can be obtained running a THFEA on the round-rotor simplified model where the complex current density $\overline{\Lambda}_{\nu}(\theta)$, given by (2.12)-(2.13), is impressed on the ferromagnetic cylinder surface at a frequency equal to $\nu\omega$ according to (2.11). Once the additional losses for all the significant harmonic orders ν are determined, they can be added to obtain the total additional losses P_{tot} caused by the whole air-gap magnetic field as:

$$P_{tot}=\sum_{\nu=1,3,5..}P_{\nu} \tag{2.14}$$

It is worth noticing that applying the superposition principle to power losses as per (2.14) is possible because for each harmonic order ν, eddy currents of different frequency ($\nu\omega$) are induced in stator conductors and, hence, losses associated with all values of ν can be summed up [19].

As an example, the machine working conditions illustrated in Figure 2.3 are reproduced through the described method in order to compare results with those obtained from TSFEA. The field current I_f and the initial rotor angle θ_{r0} appearing in (2.13) are computed for the operating point of interest as discussed in Appendix B, with no need for additional simulations. THFEA simulation results in terms of eddy-current losses produced by each conductor by different harmonics are shown in Figure 2.24 focusing on harmonic orders up to 19 and on the five conductors closest to the air gap, as in the other strands the additional losses are negligible.

Results are shown for no-load and full-load conditions, in the latter case distinguishing between wide and thin slot design. Figure 2.24 shows the impact of the various harmonics on the skin-effect additional losses caused by air-gap fluxes entering the slot. It can be noticed that, at no load, most of the losses result from the fundamental and the 5^{th} and 7^{th} harmonics, being the 3^{rd} almost absent (Figures 2.8 and 2.22). Conversely, in loaded condition the 3^{rd} harmonic is the major source for additional losses. It is also confirmed, as discussed in Section 2.2, that the thin-slot design leads to a very significant loss reduction (by nearly a factor 4).

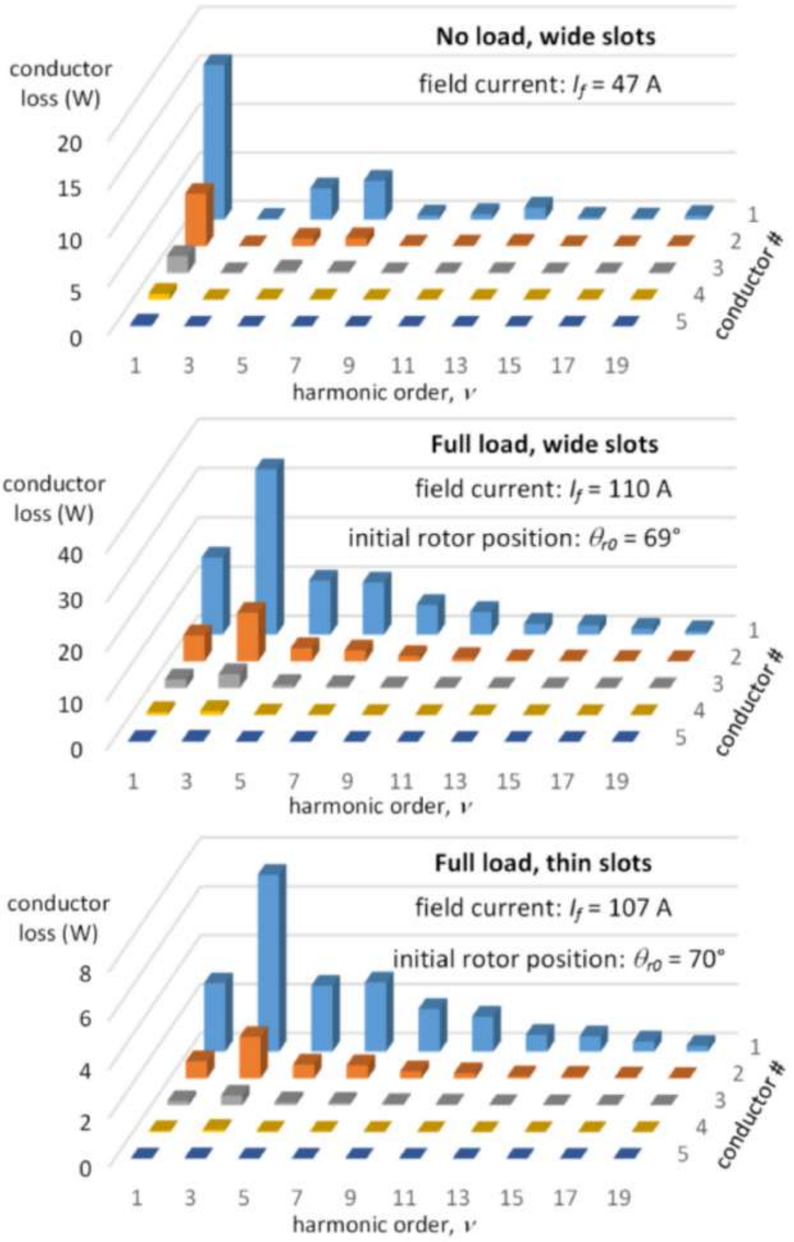

Figure 2.24: Additional losses from THFEA for harmonic orders $\nu = 1..19$ and for the first five conductors closest to the air gap.

The losses due to all individual harmonics can be summed up as per (2.14). To the resultant additional losses we then need to sum the ordinary RI^2 Joule losses, as conductors in the THFEA have no impressed current. In order to also take into account the skin effect caused by slot leakage fluxes Figure 2.9-(b), the AC resistance R of each single strand is computed as [15]:

$$R = R_{dc}k_r = \rho_{Cu}\frac{L}{h_c w_c}k_r \tag{2.15}$$

where R_{dc} is the DC resistance, ρ_{Cu} is the copper resistivity, h_c and w_c conductor cross-sectional dimension and $k_r > 1$ is the resistance correction coefficient estimated as per [15]. Computed values are given in Table 2.4.

Table 2.4: Resistance and conventional Joule losses for a single conductor.

	R_{dc}	k_r	RI^2
Wide slot design	$4.0 \times 10^{-4}\Omega$	1.24	3.6 W
Thin slot design	$5.8 \times 10^{-4}\Omega$	1.19	5.1 W

Results in terms of total losses per conductor are shown in Figure 2.25 where a comparison is made between values obtained by TSFEA (Section 2.2) and those obtained from THFEA and summing the RI^2 contribution (Table 2.4). For both no-load and on-load operation and for both thin and wide slot design, a very good agreement exists between TSFEA and THFEA results, provided that saturation is neglected in the former (similar comparisons have been repeated for the machine operating in other working conditions – e.g. at different power factors – and the same level of accordance as shown in Figure 2.25 has been obtained). As observed in Section 2.2, magnetic saturation flattens the air-gap flux density waveform and causes errors in the order of 15% in the prediction of the losses in conductor #1. However, in all the cases investigated, magnetic saturation acts in the sense of reducing losses, so that predictions through linear THFEA are conservative. In any case, the proposed method appears fully capable of identifying possible design solution (e.g. excessive slot width) for which overheating and hot spots can be expected. In fact, the very large difference from the thin and wide slot design appears to be fully captured.

In terms of computational performance for the example machine under study, TSFEA takes approximately 5 hours while THFEA, run on the same computer, takes less than 30 seconds for each harmonic order ν. For instance, the results shown in Figure 2.25 consider the contribution of the first 40 odd-order harmonics, with a total simulation time of about 10 minutes. In addition to the computation time saving, a significant advantage of the THFEA approach consists of the easier model geometry (Figure 2.23) and setup, with no need to include rotor motion and wait for simulations to reach steady-state conditions.

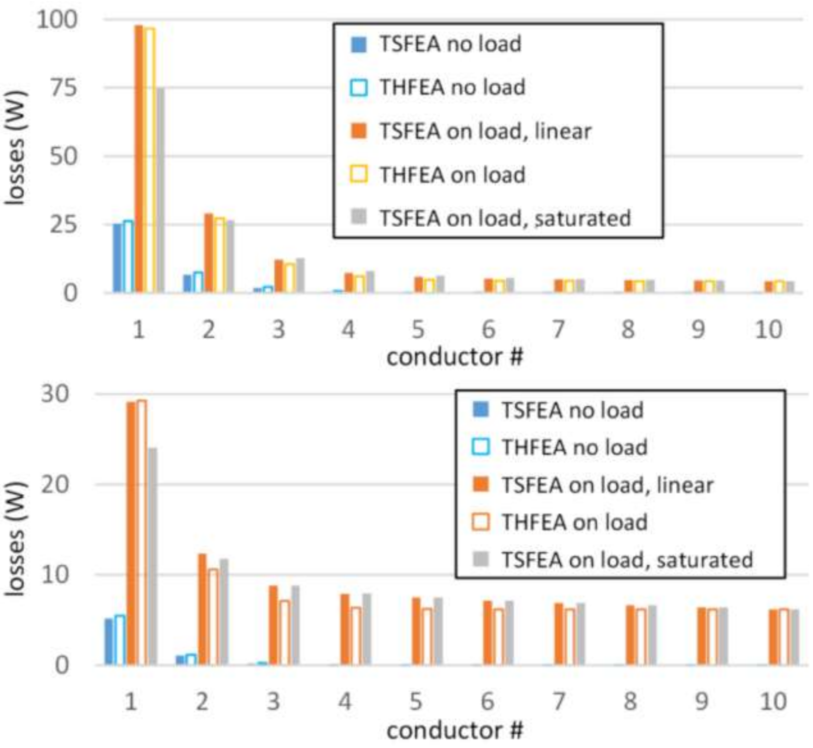

Figure 2.25: Comparison of the losses computed from TSFEA and THFEA.

2.4 Reduced model for THFEA simulations

Looking at Figure 2.23 it can be easily understood that only the region around the slot being modelled in detail, where eddy currents are inducted and losses are computed, is actually of interest. Therefore, having the whole machine cross section considered, although in a simplified way, appears redundant and the question naturally arises as to whether it is possible to limit the study to a portion of the model such as that shown in Figure 2.26, delimited by air-gap radial segments CD and EF.

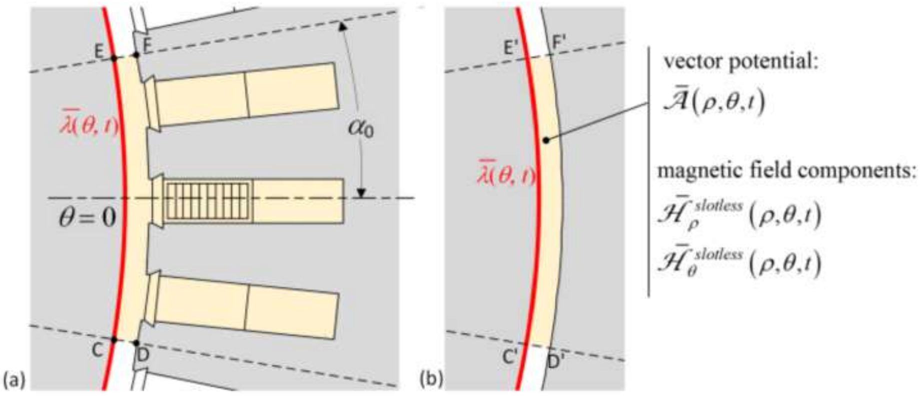

Figure 2.26: (a) Region of the model limited by air-gap radial segments CD and EF; (b) the same region but with a slotless stator geometry.

The idea proposed for limiting the study to the reduced model is to analytically compute the radial magnetic field along segments CD and EF and use this to apply Neumann boundary condition along such segments. For this purpose, the magnetic field is first determined in the hypothesis of slotless stator - i.e. referring to the slotless model version in Figure 2.26-(b) and then the complex permeance function is applied to account for the stator slotting effect [20].

The magnetic field produced in the slotless domain (Figure 2.26-(b)) by the linear current density (2.11) can be found by solving the Laplace's equation for the vector potential $\overline{\mathcal{A}}(\rho,\theta,t)$:

$$\frac{\partial^2\overline{\mathcal{A}}(\rho,\theta,t)}{\partial\rho^2}+\frac{1}{\rho}\frac{\partial\overline{\mathcal{A}}(\rho,\theta,t)}{\partial\rho}+\frac{1}{\rho^2}\frac{\partial^2\overline{\mathcal{A}}(\rho,\theta,t)}{\partial\theta^2}=0 \tag{2.16}$$

Considering the vector potential theory, the radial and tangential magnetic field components are immediately defined as [21]:

$$\overline{\mathcal{H}}_\rho^{slotless}(\rho,\theta,t)=-\frac{1}{\mu_0\rho}\frac{\partial\overline{\mathcal{A}}(\rho,\theta,t)}{\partial\theta} \tag{2.17}$$

$$\overline{\mathcal{H}}_\theta^{slotless}(\rho,\theta,t)=\frac{\partial\overline{\mathcal{A}}(\rho,\theta,t)}{\partial\rho} \tag{2.18}$$

In order to evaluate the vector potential $\overline{\mathcal{A}}(\rho,\theta,t)$, the following boundary conditions are applied:

$$\left.\frac{\partial\overline{\mathcal{A}}(\rho,\theta,t)}{\partial\rho}\right|_{\rho=R_s}=0 \tag{2.19}$$

$$\left.\frac{1}{\mu_0}\frac{\partial\overline{\mathcal{A}}(\rho,\theta,t)}{\partial\rho}\right|_{\rho=R_r}=\overline{\lambda}(\theta,t) \tag{2.20}$$

where (2.19) is due to the assumption taken into account of considering an infinitely permeable stator core while (2.20) is due to the magnetic field tangential component equalling the linear current density everywhere on the round rotor surface.

Assuming the expression:

$$\overline{\mathcal{A}}(\rho,\theta,t)=\sum_{\nu=1,3,5..}e^{i\nu\omega t}\overline{\mathcal{A}}_\nu(\rho,\theta) \tag{2.21}$$

equations (2.17) and (2.18) can be written as:

$$\overline{\mathcal{H}}_\rho^{slotless}(\rho,\theta,t)=-\frac{1}{\mu_0\rho}\sum_{\nu=1,3,5..}e^{i\nu\omega t}\frac{\partial\overline{\mathcal{A}}_\nu(\rho,\theta)}{\partial\theta} \tag{2.22}$$

$$\overline{\mathcal{H}}_\theta^{slotless}(\rho,\theta,t)=\sum_{\nu=1,3,5..}e^{i\nu\omega t}\frac{\partial\overline{\mathcal{A}}_\nu(\rho,\theta)}{\partial\rho} \tag{2.23}$$

By substituting (2.11) and (2.21) into (2.16)-(2.17)-(2.18), the time dependence disappears and (2.16)-(2.17)-(2.18) are reduced to:

$$\frac{\partial^2 \overline{\mathcal{A}}_\nu(\rho,\theta)}{\partial \rho^2} + \frac{1}{\rho}\frac{\partial \overline{\mathcal{A}}_\nu(\rho,\theta)}{\partial \rho} + \frac{1}{\rho^2}\frac{\partial^2 \overline{\mathcal{A}}_\nu(\rho,\theta)}{\partial \theta^2} = 0 \tag{2.24}$$

$$\left.\frac{\partial \overline{\mathcal{A}}_\nu(\rho,\theta)}{\partial \rho}\right|_{\rho=R_s} = 0 \tag{2.25}$$

$$\left.\frac{1}{\mu_0}\frac{\partial \overline{\mathcal{A}}_\nu(\rho,\theta)}{\partial \rho}\right|_{\rho=R_r} = \overline{\Lambda}_\nu(\theta) \tag{2.26}$$

for any harmonic order ν. Substituting (2.12) into (2.26), the system (2.24), (2.25) and (2.26) can be solved by separation of variables and the solution can be plugged into (2.22), (2.23) so that the following expressions of the radial and tangential complex magnetic field components are obtained:

$$\overline{\mathcal{H}}_\rho^{slotless}(\rho,\theta,t) = \sum_{\nu=1,3,5..} e^{i\nu\omega t}\overline{H}_{\rho\nu}(\rho,\theta) \tag{2.27}$$

$$\overline{\mathcal{H}}_\theta^{slotless}(\rho,\theta,t) = \sum_{\nu=1,3,5..} e^{i\nu\omega t}\overline{H}_{\theta\nu}(\rho,\theta) \tag{2.28}$$

where

$$\overline{H}_{\rho\nu}(\rho,\theta) = i\overline{E'}_\nu f_{-\nu p}(\rho) e^{i\nu p\theta} + \sum_{k\in\mathbb{Z},q\in\{-1,1\}} i\overline{F'}_{\nu,k,q} e^{-i(6qk+\nu)p\theta} f_{-(6qk+\nu)p}(\rho) \tag{2.29}$$

$$\overline{H}_{\theta\nu}(\rho,\theta) = \overline{E'}_\nu g_{-\nu p}(\rho) e^{i\nu p\theta} + \sum_{k\in\mathbb{Z},q\in\{-1,1\}} \overline{F'}_{\nu,k,q} e^{-i(6qk+\nu)p\theta} g_{-(6qk+\nu)p}(\rho) \tag{2.30}$$

where functions $f_n(\rho)$ and $g_n(\rho)$ are defined for any arbitrary integer n as:

$$f_n(\rho) = \frac{R_r^{n+1}(R_s^{n+1} + \rho^{2n})}{\rho^{n+1}(R_s^{2n} - R_r^{2n})} \tag{2.31}$$

$$g_n(\rho) = \frac{R_r^{n+1}(R_s^{n+1} - \rho^{2n})}{\rho^{n+1}(R_s^{2n} - R_r^{2n})} \tag{2.32}$$

To this point, once the magnetic field in the slotless domain (Figure 2.26-(b)) is defined by equations (2.27) and (2.28), the stator slotting effect needs to be included for the completeness of the analytical magnetic field evaluation. For that, the complex permeance function associated with the stator slots computed according to different methods [21, 22] is applied to (2.27) and (2.28). Thus, the radial component of the magnetic field produced by the rotor surface current in the slotted domain (Figure 2.26-(a)) can be written using the complex permeance function components p_{sa}

and p_{sb} as in [22]:

$$\begin{aligned}\overline{\mathcal{H}}_{\rho}^{slotted}(\rho,\theta,t) &= \overline{\mathcal{H}}_{\rho}^{slotless}(\rho,\theta,t)p_{sa}(\rho,\theta) + \overline{\mathcal{H}}_{\theta}^{slotless}(\rho,\theta,t)p_{sb}(\rho,\theta) \\ &= \sum_{\nu=1,3,5..} e^{i\nu\omega t}\left[\overline{H}_{\rho\nu}(\rho,\theta)p_{sa}(\rho,\theta) + \overline{H}_{\theta\nu}(\rho,\theta)p_{sb}(\rho,\theta)\right]\end{aligned} \tag{2.33}$$

The two components p_{sa} and p_{sb} of the relative complex permeance function for the machine under study are herein computed as per [22]. Their diagrams along the mean airgap circumference ($\rho = R_m$) are plotted in Figure 2.27.

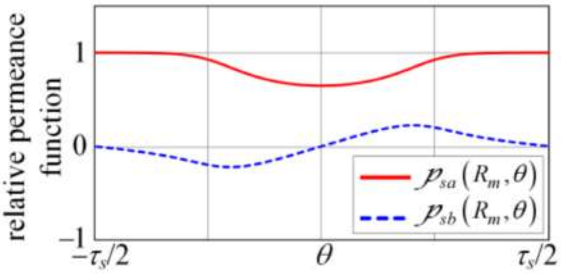

Figure 2.27: Two components of the relative permeance function associated with stator slotting plotted across a slot pitch.

In particular, along segments EF and CD the radial magnetic field will be given by (2.33) for $\theta = \pm\alpha_0$ where $2\alpha_0$ is the reduced model angular span. For the purpose of field solution in the slotted domain (Figure 2.26-(a)), imposing the radial magnetic field along segments EF and CD is equivalent to imposing an identical value of linear current density in the reduced model shown in Figure 2.26-(a), where the two segments act as boundaries between the air-gap domain and an infinitely permeable ferromagnetic region. The linear current density to be imposed on CD and EF in Figure 2.26-(a) will be:

$$\overline{\lambda}_{CD}(\rho,t) = \overline{\mathcal{H}}_{\rho}^{slotted}(\rho,-\alpha_0,t) = \sum_{\nu=1,3,5..} e^{i\nu\omega t}\overline{\Lambda}_{CD,\nu}(\rho) \tag{2.34}$$

$$\overline{\lambda}_{EF}(\rho,t) = \overline{\mathcal{H}}_{\rho}^{slotted}(\rho,\alpha_0,t) = \sum_{\nu=1,3,5..} e^{i\nu\omega t}\overline{\Lambda}_{EF,\nu}(\rho) \tag{2.35}$$

where

$$\overline{\Lambda}_{CD,\nu}(\rho) = \overline{H}_{\rho\nu}(\rho,-\alpha_0)p_{sa}(\rho,-\alpha_0) + \overline{H}_{\theta\nu}(\rho,-\alpha_0)p_{sb}(\rho,-\alpha_0) \tag{2.36}$$

$$\overline{\Lambda}_{EF,\nu}(\rho) = \overline{H}_{\rho\nu}(\rho,\alpha_0)p_{sa}(\rho,\alpha_0) + \overline{H}_{\theta\nu}(\rho,\alpha_0)p_{sb}(\rho,\alpha_0) \tag{2.37}$$

for $R_r \leq \rho \leq R_s$.

In conclusion, the losses caused by the ν^{th} order harmonic can be computed through a set of THFEA simulations at frequencies $\nu\omega$ using the extremely simplified model in Figure 2.28-(b) where: a homogeneous Neumann boundary condition is assigned to the whole outer contour; the

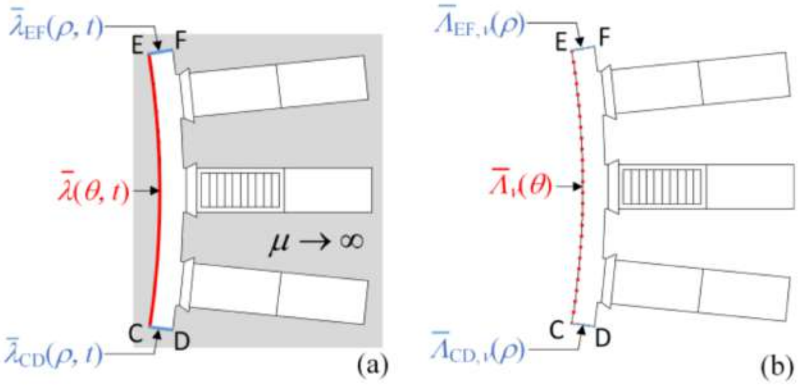

Figure 2.28: (a) Reduced model with current densities spread on arc EC and segments CD and EF; (b) THFEA model for the ν^{th} harmonic at frequency $\nu\omega$.

linear current density $\overline{\Lambda}_{\nu}(\theta)$ given by (2.12) is applied along the arc EC; the linear current densities $\overline{\Lambda}_{CD,\nu}(\rho)$ and $\overline{\Lambda}_{EF,\nu}(\rho)$ given by (2.36)-(2.37) are applied along the radial segments CD and EF, respectively. A single THFEA simulation (for a given ν) using the model in Figure 2.28-(b) takes around 4 seconds to give the power losses P_{ν} associated with the ν^{th} harmonic. As an example, supposing to run one THFEA for 15 values of $\nu = 1, 3, 5..$, the total simulation time will be about two minutes.

As a validation of the procedure, Figure 2.29 compares the solution of the whole round-rotor model (Figure 2.23) to the solution of the reduced model (Figure 2.28-(b)). The eddy-current density color map in the two cases, displayed with the same scale, suggests that the models are in full agreement. In fact, the same results shown in Figure 2.25 for the THFEA of the whole round-rotor model are obtained, with discrepancies less than 2%, from the reduced model. The latter, however, offers the advantage of an extremely fast calculation time and its extreme simplicity makes it particularly suitable for a fully automated construction, set-up and post-processing.

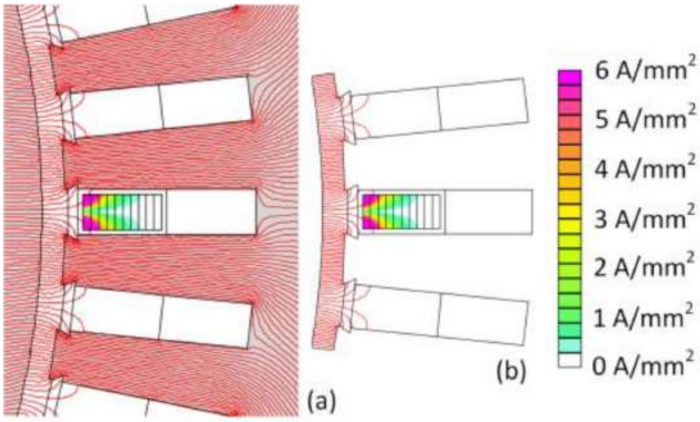

Figure 2.29: Magnetic field lines and eddy current density resulting from (a) the complete round-rotor model and (b) the reduced model.

It is worth to be noted that, considering a model angular span equal to three slot pitches gives reasonable confidence that segments EF and CD are placed sufficiently far from the conductors where eddy current arise so that it is possible to neglect the field causes by such eddy currents and thus approximate the tangential field through (2.33). In fact, the air-gap magnetic field which produced through the fictitious linear current densities applied to the radial segments EF and CD of Figure 2.28 is, actually, the field that we would have in loaded condition in the absence of eddy currents in stator conductors-i.e. equation (2.33) necessarily neglects such currents which are the output of the computation process and cannot be then known in advance. Hence, it is reasonable to consider that the magnetic field is actually equal to (2.33) at points which are sufficiently distant from the slot where eddy currents occur because, in such points, the effect of eddy currents is negligible.

2.5 Conclusion

In large medium-voltage AC electric machines with form wound coils and open slots, air-gap flux lines can enter the slot and sweep the conductors placed near the gap, causing eddy currents and additional losses that may result in local overheating and insulation failures. The phenomenon can be predicted through TSFEA including rotor motion, which however implies long simulation times, very complicated models and lengthy post-processing. This work has presented fast computation approaches to compute these additional losses through THFEA using a simplified stationary model where the moving rotor is replaced by a static ferromagnetic cylinder. The air-gap revolving field of the real machine is reproduced by spreading a suitable current sheet on the ferromagnetic cylinder surface.

To define such fictitious surface current, only three MSFEA simulations are used to capture rotor saliency effects in case of a generic salient pole geometry. It has been shown that THFEA simulations can be drastically sped up by considering one single slice of the simplified stationary model by impressing a further analytically computed current-sheet on the slice sides to account for the surrounding parts being excluded.

By applying the proposed technique on an example salient-pole generator, it has been shown that computation times can be abated from several hours required by TSFEA to few minutes, giving practically identical results in terms of additional loss prediction. A shortcoming of the method is that it assumes only impressed (not induced) currents in rotor circuits and does not account for magnetic saturation; the latter is, however, shown to reduce the losses under study, so that results obtained under linear core assumption can be regarded as conservative.

Finally, the method has been described addressing only skin effect losses arising in each single conductor. With limited extensions, the approach can be adapted to cover proximity losses due to circulating currents among multiple shunt connected strands that may be present in each turn.

Bibliography

[1] M. Popescu and D. G. Dorrell, "Proximity losses in the windings of high speed brushless permanent magnet ac motors with single tooth windings and parallel paths," *IEEE Transactions on Magnetics*, vol. 49, no. 7, pp. 3913–3916, 2013.

[2] A. S. Thomas, Z. Q. Zhu, and G. W. Jewell, "Proximity loss study in high speed flux-switching permanent magnet machine," *IEEE Transactions on Magnetics*, vol. 45, no. 10, pp. 4748–4751, 2009.

[3] R. J. Musil, S. Wenger, and K. Scherer, "Practical considerations concerning impulse voltage testing of form-wound coils for rotating machines," *IEEE Transactions on Energy Conversion*, vol. 3, no. 1, pp. 111–115, 1988.

[4] M. J. Islam, H. V. Khang, A. . Repo, and A. Arkkio, "Eddy-current loss and temperature rise in the form-wound stator winding of an inverter-fed cage induction motor," *IEEE Transactions on Magnetics*, vol. 46, no. 8, pp. 3413–3416, 2010.

[5] M. J. Islam, J. Pippuri, J. Perho, and A. Arkkio, "Time-harmonic finite-element analysis of eddy currents in the form-wound stator winding of a cage induction motor," *IET Electric Power Applications*, vol. 1, no. 5, pp. 839–846, 2007.

[6] A. Tessarolo, F. Luise, S. Pieri, A. Benedetti, M. Bortolozzi, and M. De Martin, "Design for manufacturability of an off-shore direct-drive wind generator: An insight into additional loss prediction and mitigation," *IEEE Transactions on Industry Applications*, vol. 53, no. 5, pp. 4831–4842, 2017.

[7] A. Tessarolo, F. Agnolet, F. Luise, and M. Mezzarobba, "Use of time-harmonic finite-element analysis to compute stator winding eddy-current losses due to rotor motion in surface permanent-magnet machines," *IEEE Transactions on Energy Conversion*, vol. 27, no. 3, pp. 670–679, 2012.

[8] Y. Zhao, D. Li, T. Pei, and R. Qu, "Overview of the rectangular wire windings ac electrical machine," *CES Transactions on Electrical Machines and Systems*, vol. 3, no. 2, pp. 160–169, 2019.

[9] L. J. Wu and Z. Q. Zhu, "Simplified analytical model and investigation of open-circuit ac winding loss of permanent-magnet machines," *IEEE Transactions on Industrial Electronics*, vol. 61, no. 9, pp. 4990–4999, 2014.

[10] L. J. Wu, Z. Q. Zhu, D. Staton, M. Popescu, and D. Hawkins, "Analytical model of eddy current loss in windings of permanent-magnet machines accounting for load," *IEEE Transactions on Magnetics*, vol. 48, no. 7, pp. 2138–2151, 2012.

[11] A. Fatemi, D. M. Ionel, N. A. O. Demerdash, D. A. Staton, R. Wrobel, and Y. C. Chong, "Computationally efficient strand eddy current loss calculation in electric machines," *IEEE Transactions on Industry Applications*, vol. 55, no. 4, pp. 3479–3489, 2019.

[12] S. Yamada and K. Bessho, "Harmonic field calculation by the combination of finite element analysis and harmonic balance method," *IEEE Transactions on Magnetics*, vol. 24, no. 6, pp. 2588–2590, 1988.

[13] J. Pries and H. Hofmann, "Harmonic balance fea of synchronous machines using a traveling-wave airgap model," in *2011 IEEE Vehicle Power and Propulsion Conference*, 2011, pp. 1–6.

[14] A. Tessarolo, "Accurate computation of multiphase synchronous machine inductances based on winding function theory," *IEEE Transactions on Energy Conversion*, vol. 27, no. 4, pp. 895–904, 2012.

[15] I. Boldea and S. Nasar, *The induction machine handbook*. FL: CRC, 2002.

[16] V. Ruuskanen, J. Nerg, M. Niemelä, J. Pyrhönen, and H. Polinder, "Effect of radial cooling ducts on the electromagnetic performance of the permanent magnet synchronous generators with double radial forced air cooling for direct-driven wind turbines," *IEEE Transactions on Magnetics*, vol. 49, no. 6, pp. 2974–2981, 2013.

[17] J. Pyrhonen, T. Jokinen, and V. Hrabovcova, *Design of rotating electrical machines*. John Wiley & Sons, 2013.

[18] R. F. Burbidge, "A rapid method of analysing the m.m.f. wave of a single or polyphase winding," *Proceedings of the IEE - Part C: Monographs*, vol. 105, no. 7, pp. 307–311, 1958.

[19] A. Tessarolo, M. Bortolozzi, and M. Mezzarobba, "On the validity of the harmonic superposition principle for computing rotor eddy current losses in permanent magnet machines," in *2012 XXth International Conference on Electrical Machines*, 2012, pp. 1369–1373.

[20] D. Zarko, D. Ban, and T. A. Lipo, "Analytical calculation of magnetic field distribution in the slotted air gap of a surface permanent-magnet motor using complex relative air-gap permeance," *IEEE Transactions on Magnetics*, vol. 42, no. 7, pp. 1828–1837, 2006.

[21] J. D. Jackson, "Classical electrodynamics," 1999.

[22] N. Elloumi, M. Bortolozzi, and A. Tessarolo, "On the analytical determination of the complex relative permeance function for slotted electrical machines," in *2020 International Conference on Electrical Machines (ICEM)*, vol. 1, 2020, pp. 253–258.

Appendices

Appendix A

The use of the harmonic equivalent circuit proposed in paragraph 1.5.5.4 of Section 1.5 requires the determination of the equivalent circuit components $X_{m,n}$, $R_{2,n}$ and $X_{2,n}$ as shown in Figure 30. No stator components are considered according to the simplifying assumptions that have been set consisting of neglecting the voltage drop caused by the stator side.

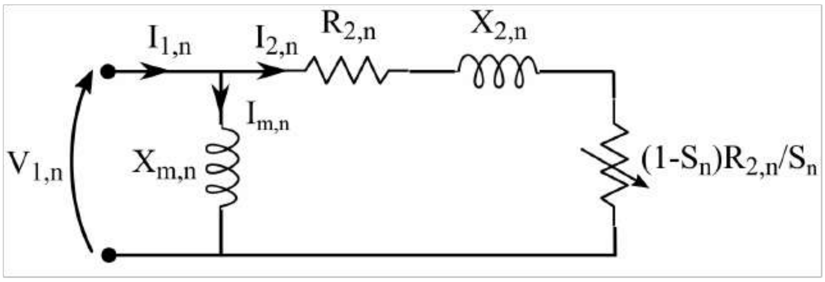

Figure 30: Simplified phase harmonic equivalent circuit.

As far as high order MMF space harmonics are concerned, the variation of the rotor bars resistance and the inductance due to skin effect need to be taken into account as they intrinsically depend on the frequency. One way to capture the effect of high frequencies on the resistance and inductance of the rotor bars can be through THFEA. For this purpose, a simplified single bar model is reproduced by THFEA under different frequency values imposing Dirichlet boundary condition along the segment AB as illustrated in Figure 31. The bar model in characterised by the same conductivity employed in the example machine understudy and fed by a RMS current I_b. The bar resistance R_b for each frequency value is determined from the Joule losses P_b generated in

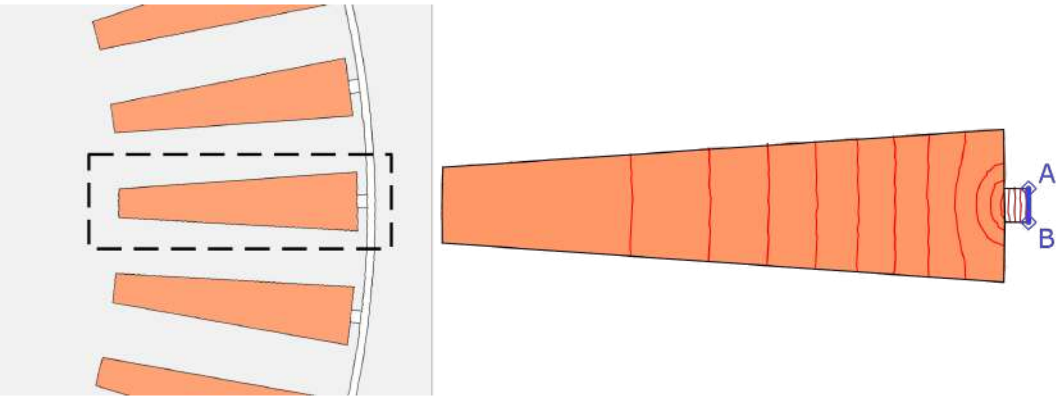

Figure 31: THFEA simplified bar model. The depth of the model and the conductivity of the bar material are imposed according to the IM characteristics stated in Table 1.13.

the bar region as:

$$R_b(f) = \frac{P_b(f)}{I_b^2} \tag{38}$$

As for the bar inductance L_b, it can be calculated from the magnetic field energy of the bar slot opening area W_b as:

$$L_b(f) = 2\frac{W_b(f)}{I_b^2} \tag{39}$$

Results of THFEA simulations in terms of bar resistance R_b and inductance L_b function of the frequency f are presented in Figure 32. At this point, in order to report the parameters of the rotor bars into the stator, a transformation ratio m_n for each harmonic of order n needs to be determined in such a way that the resistance and inductance of the rotor reported to the stator are written as:

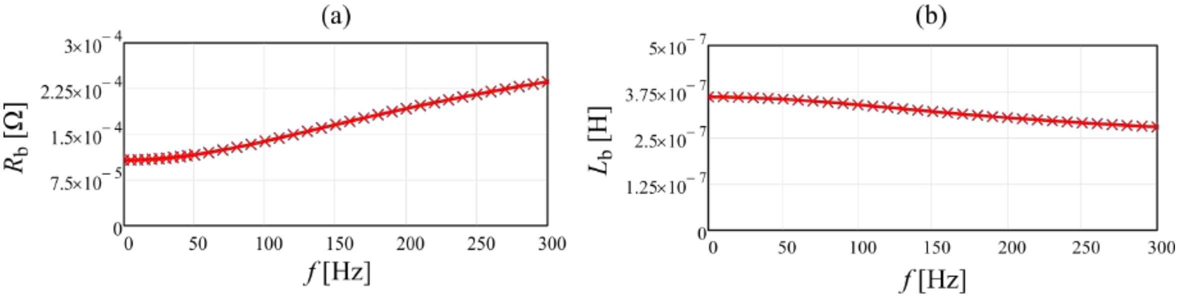

Figure 32: Variation of the bar resistance and inductance with the frequency resultant from the THFEA simulations applied to the simplified bar model of Figure 31.

$$R_{2,n} = m_n^2 R_b(f_n) \tag{40}$$

$$X_{2,n} = 2\pi f_n m_n^2 L_b(f_n) \tag{41}$$

where $f_n = S_n f$ when f is the stator frequency (the fundamental frequency). For this purpose, it is legit to consider the principle of power conservation since reporting the rotor parameters to the stator does not alter the generated power. More particularly, the total Joule losses dissipated in the rotor cage bars in presence of an RMS current I_b for the harmonic order n can be expressed as:

$$P_{loss,n} = Z_b R_b(f_n) I_b^2 \tag{42}$$

The same power losses can be formulated using the parameters of the harmonic equivalent circuit as:

$$P_{loss,n} = 3R_{2,n} I_{2,1}^2 \tag{43}$$

Equalizing the two expressions (41) and (42), and substituting $R_{2,n}$ by its expression of (40), the relation between the bar current I_b and the harmonic rotor current reported to the stator $I_{2,n}$ can be obtained as:

$$I_{2,n}^2 = \frac{Z_b}{3m_n^2} I_b^2 \tag{44}$$

To this point, a further relation need to be used to adequately determine the transformation ratio. According to the principle of MMF invariance, the air-gap MMF produced by circulating current of the rotor reported of the stator has to be equal to the one generated by the real bars current. Based on the well-known relationship $[A1]$, the n^{th} harmonic MMF amplitude produced by the n^{th} harmonic rotor current of the rotor reported to the stator can be formulated as:

$$MMF_n = \frac{3}{\pi n}(\sqrt{2}I_{2,n})N_{t_n} \tag{45}$$

where $N_{t_n}$is the harmonic equivalent number of turns per phase.

In order to determine the expression of the n^{th} harmonic MMF produced by the real current I_b circulating in the bars, the instantaneous linear current density of bars under one pole pitch τ_n when crossed by a RMS current I_b is considered. Usually, the number of bars per pole are assumed be sufficiently high, the linear current density $\lambda(\theta)$ can be approximated to have a sinusoidal waveform with a maximum value written as (Figure 33):

$$\lambda_{max} = \frac{\sqrt{2}I_b}{\tau_b} = \frac{I_b Z_b}{\sqrt{2}\pi R_r} \tag{46}$$

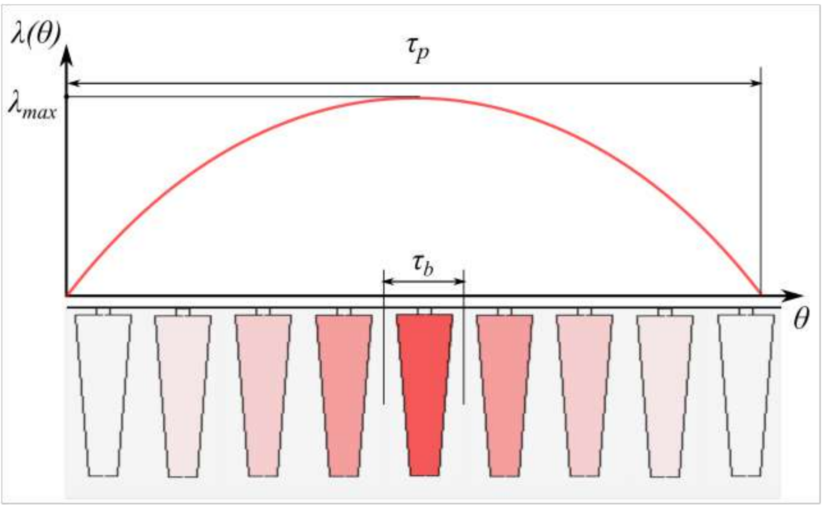

Figure 33: Schematic presentation of: the the linear current density distribution produced by the bars under one pole pitch τ_p.

Thus, the maximum magnetizing potential in the air-gap can be calculated by integrating the the linear current density of the bars over the harmonic pole pitch such that:

$$\Lambda_{max} = \int_0^{\tau_n} \lambda_{max} \sin\left(\frac{\pi}{\tau_n}\right) dx = \frac{2}{\pi}\lambda_{max}\tau_n = \frac{2}{\pi}\frac{I_b Z_b}{\sqrt{2}R_r}\frac{2\pi R_r}{2n} = \frac{\sqrt{2}I_b Z_b}{\pi n} \tag{47}$$

The MMF produced by the rotor cage when crossed by a current of RMS value I_b can be expressed as follows:

$$MMF_n = \frac{\Lambda_{max}}{2} = \frac{\sqrt{2} I_b Z_b}{2\pi n} \tag{48}$$

The equality between (45) and (48) allows to express the relation between I_b and $I_{2,n}$ like:

$$I_{2,n} = \frac{Z_b}{6N_{t_n}} I_b \tag{49}$$

Substitution (49) in (45), the harmonic transformation ratio can be finally defined as:

$$m_n = \frac{2\sqrt{3} N_{t_n}}{\sqrt{Z_b}} \tag{50}$$

To this point, the only remaining component to be determined is the magnetizing reactance of the n^{th} harmonic $X_{m,n} = 2\pi f_n L_{m,n}$ where $L_{m,n}$ is the magnetizing inductance that can be calculated as $[A2]$:

$$L_{m,n} = \frac{6}{\pi^2} \frac{\mu_0 L \tau_n}{g} \frac{N_{t_n}^2}{n} \tag{51}$$

References

$[A1]$ R. F. Burbidge, "A rapid method of analysing the m.m.f. wave of a single or polyphase winding," *Proceedings of the IEE - Part C: Monographs*, vol. 105, no. 7, pp. 307-311, March 1958.

$[A2]$ J. Pyrhonen, T. Jokinen, and V. Hrabovcova, *Design of rotating electrical machines*, JohnWiley & Sons, 2013.

Appendix B

The use of THFEA proposed in Section 2.3 requires the knowledge of the initial rotor position (at t=0) θ_{r0} and full-load field current I_f for defining the fictitious current sheet to be applied on the ferromagnetic cylinder surface (Figure 2.23) according to (2.12)-(2.13) (of course, I_f is needed only in cases of electrically excited rotor design). The parameters are to be determined so that the machine works in the desired operating conditions, e.g. with given voltage, current and power factor. For the determination of θ_{r0} and I_f, the phasor diagram of a salient-pole synchronous machine [B1] as shown in Figure 34 (generator case) can be used.

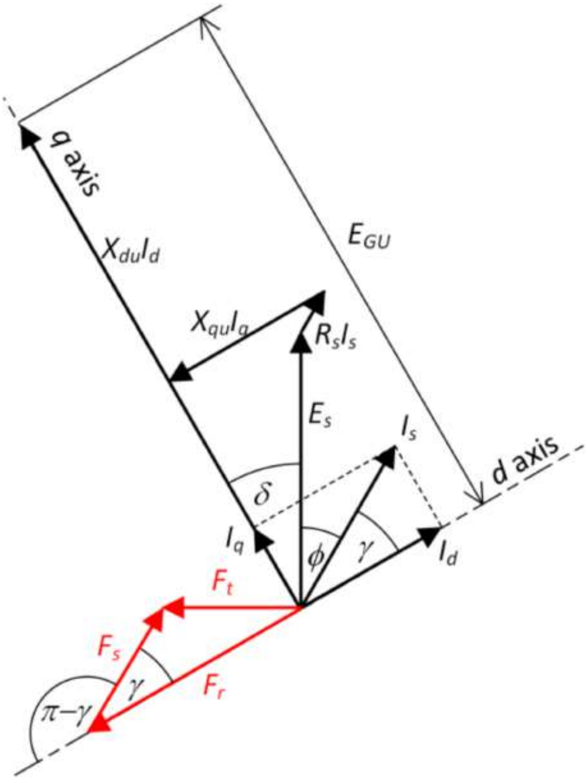

Figure 34: Phasor diagram for an electrically-excited synchronous generator.

In the figure E_s and I_s are stator phase voltage and current, R_s is stator phase resistance, X_{du} and X_{qu} are d-axis and q-axis unsaturated synchronous reactances, ϕ is the power-factor angle, γ the current angle and δ the load (or power) angle; E_{GU} is the phase electromotive-force (EMF) due to the field current; phasors F_r, F_s and F_t respectively represent the MMFs due to the field current, the armature current and their combination which sustains the total air-gap flux [$B2$]. The phase resistance can be easily computed based on winding geometry; synchronous reactances X_{du} and

X_{qu} can be determined analytically using the stator phase winding function, the rotor permeance function (2.4) and the stator slotting permeance function p_{sa} (Figure 2.27). The load angle δ can be computed as [B2]:

$$\delta = \tan^{-1} \frac{I_s(R_s \sin\phi + X_{qu} \cos\phi)}{E_s + I_s(R_s \cos\phi - X_{qu} \sin\phi)} \tag{52}$$

and the current angle γ is therefore

$$\gamma = \frac{\pi}{2} - \delta - \phi \tag{53}$$

being ϕ known from the power factor. Looking at the three MMF phasors F_r, F_s and F_t, we can note that, given the choice (2.1) for phase currents, F_s is aligned to phase a-axis while F_r is aligned to the rotor d-axis [B2]. Therefore Figure 34 shows that the initial angle θ_{r0} between phase a-axis and rotor d-axis at $t = 0$ is the mechanical angle corresponding to $\pi - \gamma$, that is:

$$\theta_{r0} = \frac{1}{p}(\pi - \gamma) = \frac{1}{p}(\frac{\pi}{2} + \delta + \phi) \tag{54}$$

Finally, the field-induced EMF E_{GU} can be found form Figure 34 $[B2]$. This is the EMF produced in a phase by the fundamental of the rotor magnetic field in (2.2):

$$\mathcal{H}_{rot}(\theta - \theta_r)\frac{I_f}{I_0} \tag{55}$$

where the function $\mathcal{H}_{rot}$ and the reference field current I_{f0} are known or fixed as discussed in Section 2.3. From this consideration, it is straightforward to determine the field current I_f in loaded operation.

References

$[B1]$ "IEEE Guide for Test Procedures for Synchronous Machines Including Acceptance and Performance Testing and Parameter Determination for Dynamic Analysis," *IEEE Std* 115-2019, 27 March 2020, p. 69.

$[B2]$ "Recommended Phasor Diagram for Synchronous Machines," *IEEE Transactions on Power Apparatus and Systems,* vol. PAS-88, no. 11, pp. 1593-1610, Nov. 1969.